eXPRESS Polymer Letters Vol.3, No.10 (2009) 605
Available online at www.expresspolymlett.com
DOI: 10.3144/expresspolymlett.2009.75

Editorial corner – a personal view
From physico- to bio-responsive polymers

*C. Werner**

Leibniz Institute of Polymer Research Dresden, Max Bergmann Center of Biomaterials & Technische Universität Dresden, Center for Regenerative Therapies Dresden, Hohe Str. 06, 01069 Dresden, Germany

Polymeric structures that undergo rapid phase transitions upon variation of environmental conditions have recently received increasing attention. Poly(N-isopropylacrylamide) and a range of related or comparable macromolecules have been successfully applied in the development of temperature-responsive systems that are used, for instance, as functional coatings of cell culture carriers to harvest cell sheets without enzymatic treatment or as valves in microfluidic circuits. Comparable effects can be achieved in polymers carrying high densities of dissociable groups, such as poly(acrylic acid), upon variation of the pH and/or ionic strength of the adjacent milieu. Polymers responding to further physical stimuli, such as magnetic or electrical fields, are also studied following the same idea.

A new class of stimuli-responsive materials goes even further: bio-responsive polymers. These macromolecules change their properties in response to recognition events with biomolecules such as growth factors, antibodies or enzymes. To make this happen, tight binding of specific molecular components to the polymeric chains is used to produce macroscopic responses such as sol-gel-transitions. Alternatively, enzymes are employed to selectively cleave susceptible segments of the macromolecules, resulting in their fragmentation. Common examples include glucose-responsive systems, enzymatically cleavable peptide-containing poly(ethylene glycols) and disulfide-based triblock copolymers responding to the gluththione levels. The responsive polymer structures are often assembled into networks or particles to maximize the macroscopic effect. Obviously, such materials can be directly used for sensoric/diagnostic applications in combination with appropriate detection principles. Beyond that, drug release systems will massively benefit from the resulting options: In a pioneering study, an antibiotic-sensing hydrogel was developed to enable the trigger inducible release of human vascular endothelial growth factor through the systemic level of an aminocoumarin antibiotic.

However, there are even more exciting options ahead. For example, using the responsiveness of macromolecules to environmental levels of biomolecular components is expected to enable feedback controlled scaffold structures for tissue engineering. We envision these materials having an in-built adaptation of physical properties, such as elasticity or permeability, to the local levels of biomolecular components, which may, in turn, control the downstream response of the biosystem brought into contact with the polymeric material. With such advances, synthetic polymeric architecture will come closer to the dynamic nature of living matter.

Prof. Dr. Carsten Werner
Member of International Advisory Board

*Corresponding author, e-mail: werner@ipfdd.de

eXPRESS Polymer Letters Vol.3, No.10 (2009) 606–614
Available online at www.expresspolymlett.com
DOI: 10.3144/expresspolymlett.2009.76

Structural features and relaxation properties of PET/PC blends containing impact strength modifier and chain extender

S. S. Pesetskii[1*], *O. V. Filimonov*[2], *V. N. Koval*[1], *V. V. Golubovich*[1]

[1]Department of Technology of Polymeric Composite Materials and Particles, V.A. Belyi Metal-Polymer Research Institute of National Academy of Sciences of Belarus, 32a, Kirov Street, 246050 Gomel, Republic of Belarus
[2]MFK 'Chemical Corporation', 29, Lazarenko St., Mogilev 212009, Republic of Belarus

Received 19 April 2009; accepted in revised form 1 July 2009

Abstract. It has been investigated how methylene diphenyl diisocyanate (MDI) influences the morphology, rheological, mechanical and relaxation properties, as well as PET crystallizability, of PET/PC/(PP/EPDM) ternary blends produced by the reactive extrusion process. It appears that irrespective of phase structure of the blends, MDI causes a rise in melt viscosity (decreased MFI-values) of the material which is the result of an increased molecular weight of the macromolecules; PET crystallization becomes retarded. MDI improves compatibility between PET and PC in PET/PC/(PP/EPDM) ternary blends. Addition of MDI leads to higher values of the dynamic shear modulus for PET high elastic state (in the temperature range between $T_{g\,\mathrm{PET}}$ and cool crystallization temperature of PET); the PET cool crystallization and melt crystallization processes become retarded; the PET and PC glass transition temperatures approach one another. MDI has been shown not to influence significantly the blend morphology or the character of interaction between the PP/EPDM disperse phase and PET/PC blend matrix.

Keywords: *polymer blends, poly(ethylene terephthalate), polycarbonate, impact modifier, chain extender*

1. Introduction

The blends of polycarbonate (PC) with poly(alkylene terephthalates), particularly poly(ethylene terephthalate) (PET), have been the subject of much attention from researchers as well as scientific schools [1–4]. This can mainly be explained by growing possibilities for developing PET/PC-based engineering materials; their properties are far more advantageous than those of the two homopolymers. Besides, when making blends, it seems possible to use – at least as one of the blend components – industrial or/and household wastes, for example, used (post-consumer) PET bottles. As a result, the commercial production of similar materials becomes quite profitable.

One of the disadvantages of PET/PC binary blends is their low impact strength measured on notched samples [2]. PET/PC blend materials show relatively high values of impact strength only at temperatures between the component glass transition temperatures ($T_{g\,\mathrm{PET}}$ and $T_{g\,\mathrm{PC}}$) [2]. For practical applications, therefore, such PET/PC blends are most suitable that contain special additives, i.e. impact strength modifiers (ISM) [5] which can increase the impact strength.

Another important problem that arises during compounding and processing of PET/PC molten blends is to prevent hydrolytic and thermal degradation of macromolecules of polyesters being blended. This problem comes, first of all, from the fact that

*Corresponding author, e-mail: otdel5mpri@tut.by

molten blends are usually processed at a temperature of 270°C or higher, because PET has a high melting temperature; the reaction rate turns out to be high and causes degradation of the macromolecular chains [6]. The reactions of macromolecular breakdown lead to reduced molecular weights, lower values of mechanical properties and lower thermal stability, which unfavorably influences the possibility of repeated processing or recycling of polyester materials [7].

Complete polycondensation initiated in the solid phase is one of the ways to prevent a negative influence of macromolecular breakdown on the properties of polycondensation thermoplastics, among them saturated polyesters such as PET and PC [8, 9]. High technological expenses required for the solid-state additional polycondensation, however, make reprocessing of polyester raw materials unprofitable.

During the last 10–15 years especially, alternative technologies have been developed for the modification of polyesters. These technologies show essential advantages compared with the solid-state polycondensation. These alternative technologies are mostly based on chemical transformations of macromolecules in molten polyesters; such chemical transformations occur with the help of additional bi- or multi-functional chemicals capable of extending the chain (so-called chain extenders) [10–15]. The chain extenders (CE) interact in melt mostly with terminal functional groups of polyester macromolecules and link them with one another; so the molecular weight does decrease, it rather increases to some extent. It was established that reactions of interaction between macromolecules and CE proceed most favourably in melt in the reactor-extruder equipped with one or two screws [16–18]. Usually, a vacuum treatment and special catalysts are used to promote these reactions [18].

This technology based on extrusion equipment becomes economically advantageous for processing polyester materials. Its abilities have been mainly investigated only for certain types of polyesters. It hasn't been understood clearly what role is played by CE in polyester blends of a more complex composition. An example of such blends is PET/PC containing ISM. The purpose of this work is to consider structural details and relaxation properties of these blends.

2. Experimental

2.1. Materials

The material was PET produced commercially by Mogilevhimvolokno Co. (Grade PET-8200 intended for making bottles and other types of packages; intrinsic viscosity, 0.882 dl/g; concentration of terminal carboxyl groups, 22.8 mmole/kg; glass transition temperature, $T_{g\,\mathrm{PET}}$ = 80°C). The second basic component for the blend was PC produced by Zarya Co, Russia (molecular weight ≈35 000; $T_{g\,\mathrm{PC}}$ = 144.5°C). The ISM was elastomer PP/EPDM based on a mixture of polypropylene and ethylene-propylene-diene rubber (melting temperature of the polypropylene component $T_{m\,\mathrm{PP}}$ = 165.5°C; crystallization temperature $T_{cr\,\mathrm{PP}}$ = 110.5°C; MFI = 2.8 g/10 min (at T = 210°C; P = 21.6 N; D_c = 2.095 mm); high flow limit of strain 10 MPa; relative elongation at rupture 595%; glass transition temperature T_g = –40°C). The PP/EPDM concentration was constant, 5 wt%, in all of the compositions tested (Table 1). The chain extender, as in work [19], was methylene diphenyl diisocyanate (MDI); its concentration was 1 wt%.

Table 1. Compositions of test materials

Composition No	Components and their concentration [wt%]
1	PET – 100 wt%
2	PC – 100 wt%
3	PET/PC – 25 wt%/(PP/EPDM) – 5 wt%
4	PET/PC – 50 wt%/(PP/EPDM) – 5 wt%
5	PET/PC – 75 wt%/(PP/EPDM) – 5 wt%
6	PET/PC – 25 wt%/(PP/EPDM) – 5 wt%/MDI – 1 wt%
7	PEt/PC – 50 wt%/(PP/EPDM) – 5 wt%/MDI – 1 wt%
8	PET/PC – 75 wt%/(PP/EPDM) – 5 wt%/MDI – 1 wt%

2.2. Preparation of blend compositions and test samples

The blend compositions have been compounded by the reactive extrusion method on extrusion-granulating line based on the twin-screw extruder TSK-35/40 (China); the screws diameters were 35 mm each; L/D = 40. The melt temperature in the extrusion zone was 265°C. MDI was introduced into the blend material as follows. First PET and PC granules were dried. Then the mixture of these granules was treated by MDI immediately before loading it into the material cylinder of the extruder.

The test samples for measuring values of the mechanical properties of the materials were injection moulded on machine EN-30 (Taiwan); screw diameter, 35 mm; shot volume, 30 cm^3. The mould temperature was set equal to 50°C.

The relaxation spectrometry was performed on plates of dimensions: 50×5×1 mm. The plates were made on laboratory-type moulding plunger machine with a shot volume of 2.5 cm^3.

Before compounding and making test samples the materials have been dried to a residual moisture content below 0.02%.

2.3. Methods of analysis

The mechanical properties of the materials in tension were determined on a universal testing machine Instron 5657 (Great Britain). The Charpy impact viscosity was determined on Charphy notched samples using the pendulum hammer PSW-1.5 (Germany). The test samples were blades with a neck measuring 50×5×3 mm and bars: 80×10×4 mm. The rheological properties were judged by MFI-values found at T = 265°C, P = 21.6 N and D_c = 2.095 mm (instrument IIRT-AM, Russia).

The analysis of temperature dependences of mechanical loss tangent (tanδ) and dynamic shear modulus (G') of the samples gave information on the dynamic-mechanical (relaxation) properties of the materials. The tests were run as in other works [2, 20], using the reverse torsion pendulum of design developed at MPRI NAS, Belarus. The test frequency was 1 Hz. The measurement accuracy was: 0.1°C for temperature; ±3% for tanδ; ±1% for G'. The test samples – plates measuring 50×5×1 mm – were injection moulded on the laboratory moulding machine of plunger type; the shot volume was 5 cm^3.

The structural morphology of the materials was studied by SEM-images taken of sections of bars (from the central portion of bars) after they had been exposed to liquid nitrogen for 30 min. The scanning electron microscope was VEGA II LSH (Czech Republic). The differential scanning analysis was performed using an instrument DSM-10M (Russia) at a heating/cooling rate of 16°C/min with weighed samples of 8 mg each. The samples were used for the analysis taken from the middle part of the specimens used for the relaxation spectrometry.

3. Results and discussion

3.1. Effect of MDI on mechanical and rheological properties of PET/PC/(PP/EPDM)

It can be seen in Table 2 that MDI – 1 wt% added to PET/PC/(PP/EPDM) blends regardless of their phase structure changes their properties. It is worth mentioning that in PET/PC blends containing PC-25% the dispersed medium was formed by PET whereas with PC-50% there were two continuous media – PET and PC. With PC-75%, the dispersed phase was PET [21]. The blends modified by MDI showed a somewhat higher level of mechanical properties such as σ_{LF}, σ_{HF}, ε_r and a (Table 2). An addition of MDI distinctly increased K_s. The MFI-values were noticed to decrease for all of the compositions. The latter fact is indicative of efficiency of MDI as a chain extender in the blends under investigation [19]. It can be understood, therefore, that PP/EPDM present in PET/PC blends is not

Table 2. Values of mechanical and rheological properties of materials

Composition No	MFI [g/10 min]	σ_{HF} [MPa]	σ_{LF} [MPa]	K_s [%]	ε_r [%]	a [kJ/m^2]
1	23.0	55	30	100	232	7.4
2	6.1	68	53	98	126	16.6
3	22.0	53	34	87	180	17.7
4	17.0	55	38	84	140	19.6
5	13.0	56	42	86	146	48.3
6	18.0	54	35	95	214	19.0
7	14.0	56	39	94	142	21.4
8	11.0	54	43	90	150	49.5

Here and henceforth, the compositions are marked as in *Table 1*. σ_{HF}, σ_{LF},ε_r are, respectively, high and low flow limits and relative elongation at rupture; K_s is strength factor for melt weld flow in injection moulding determined from the expression: $\sigma_{HF1}/\sigma_{HF2}\cdot 100\%$, where σ_{HF1} and σ_{HF2} – are, respectively, values of the upper flow limit for blade-samples moulded by melt injection in the face plane of one end and of two ends; a is Charpy impact strength measured on sharply notched samples at T = 23°C.

harmful towards MDI used as a chain extender for polyester materials. However, despite a decrease in MFI (a higher melt viscosity), the blends modified by MDI showed an increase in K_s. As this factor much depends on both the melt viscosity and on adhesion strength interaction between the phases in blends of thermodynamically incompatible or partly compatible polymers, it can be assumed that incorporated MDI causes an intensification of interphase adhesion in PET/PC blends along with an enhancement in compatibility of the components.

Table 2 shows that Charpy impact strength values determined for notched samples of compositions No.5 and No.8 are much higher than for compositions No.3–4 and 6–7. An obvious reason for this is the fact that in compositions No.3–4 and 6–7, the non-impact-resistant PET forms a continuous (disperse) medium. In compositions No.5 and No.8 the disperse medium is PC, whose impact strength much exceeds a-values for PET (Table 2, compositions No.1 and No.2). Thus the reason for a sharp rise in *a* values for compositions No.5 and No.8 is that the impact strength level for them is supported mainly by PC phase; PC is highly resistant to impact breakdown that follows chiefly the mechanism of shear flow [2]. In the blends studied, the effect of PP/EPDM is evidently reduced to increasing the degree of heterogeneity of the blend in general and of PC phase in particular. MDI acting as a chain extender encouraged an increase is shear flow resistance of the material at impact loading. That is why all of the compositions containing MDI show somewhat higher *a*-values.

3.2. Dynamic-mechanical properties of the blends

Relaxation spectrometry allows estimating variations in dynamic mechanical properties of blends within a wide temperature range and yields experimental data which can be indicative of specific interactions between phases in blends [2, 20, 21]. The temperature dependences of tanδ and G' for initial PET and PC, as well as blend compositions based on them, are shown in Figure 1. Numerical

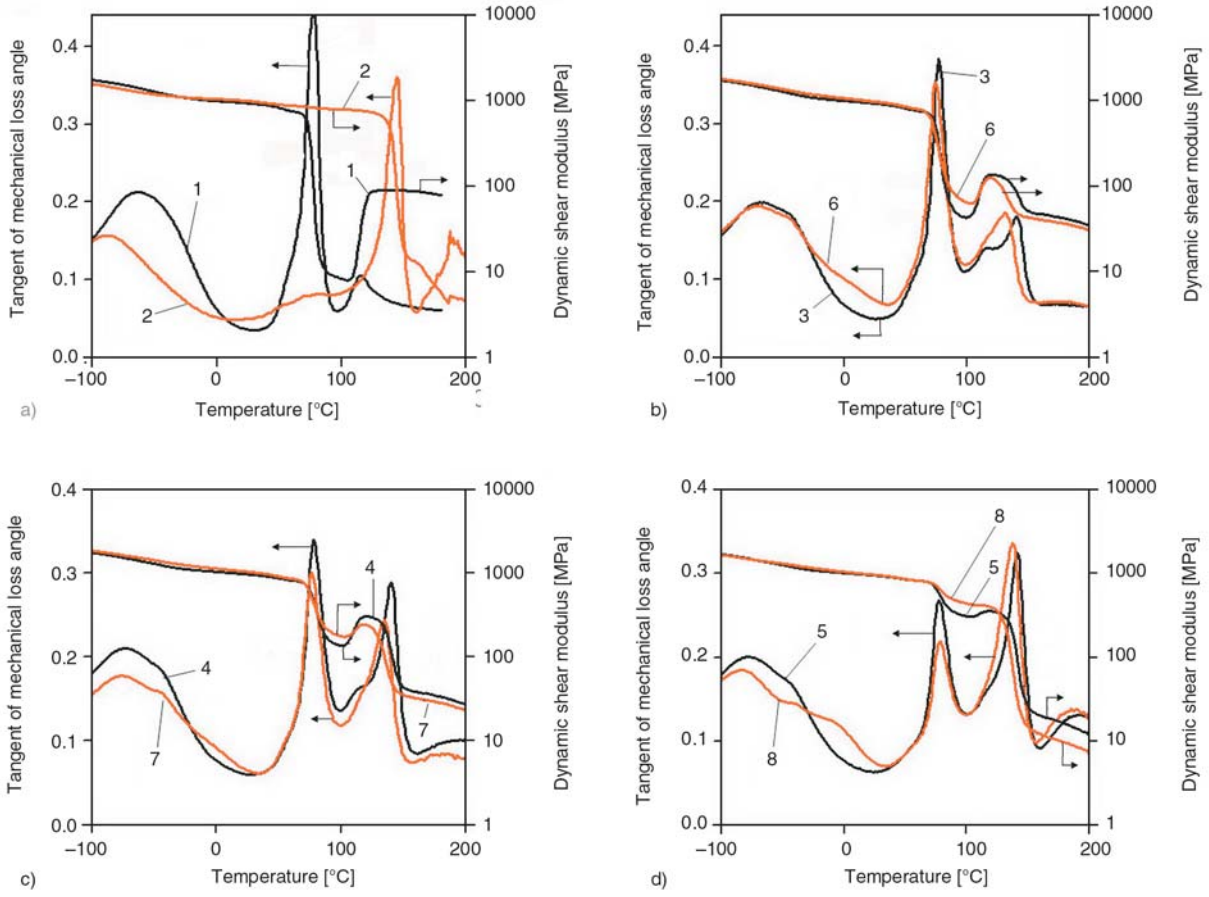

Figure 1. Mechanical loss tangent and dynamic shear modulus for polyester materials: here and henceforth the numbers of compositions are designated by digits on curves in accordance with Table 1

Table 3. Values of parameters characterizing relaxation properties of polyester materials

Composition No	$T_{g\ PET}$ [°C]	$T_{g\ PC}$ [°C]	ΔT_g [°C]	T_β [°C]	G'_{100} [MPa]	$\Delta G'_{cc}$ [MPa]
1	76.5	–	–	–61.3	8	82
2	–	144.5	–	–87.3	795	–
3	76.8	141.0	64.2	–66.8	43	93
4	78.0	141.2	63.2	–71.7	136	166
5	77.6	141.6	64.0	–76.9	308	84
6	74.3	132.0	57.7	–70.4	65	60
7	78.0	135.0	57.0	–74.2	158	59
8	78.2	138.0	59.8	–82.3	437	0

$\Delta T_g = T_{g\ PC} - T_{g\ PET}$; T_β is temperature of main maximum within the β-relaxation temperature region; G'_{100} is dynamic shear modulus at 100°C; $\Delta G'_{cc}$ is a rise in G' values with respect to G'_{100} caused by cool crystallization of PET

values of the parameters that characterize relaxation properties of the materials are listed in Table 3. An analysis of the available information led to several important conclusions about the effect of MDI on relaxation behaviour and interphase interactions in PET/PC/(PP/EPDM) ternary blends.

It can be understood from Table 3 that after MDI was added the values of T_g for PET and PC approach one another. The value of ΔT_g decreases mainly at the expense of decreased $T_{g\ PC}$, not at the expense of increased $T_{g\ PET}$. This can be explained by an improved compatibility of the components under the effect of MDI, as well as by plastification of PC by the amorphous phase of PET the T_g values of which are lower than $T_{g\ PC}$. The addition of MDI makes the values of major peak of β-relaxation shift appreciably, by 3.5–5.4°C, to the lower temperature region. The kinks present in the peak maximum of β-relaxation at $T = -41$°C are a result of simultaneous glass transition process of PP/EPDM elastomeric phase and β-relaxation process of basic components of blend (PET and PK). T_g of pure PP/EPDM is –40°C. The scanning spectroscopy data show that not only at the segmental level, but also at the level of PET and PC monomer units, effective intermolecular interactions take place; MDI plays an essential role in them.

After MDI was added, T_β values of the blends shifted (by ≈5.4°C) to the lower temperature region. The lower T_β values predetermine an opportunity of developing more frost-resistant (lower brittle temperature) materials based on MDI-modified blends.

The most important consequence of MDI added to the PET/PC/(PP/EPDM) ternary system is a considerable rise in dynamic shear modulus values within the region of high elastic state of PET (at temperatures between $T_{g\ PET}$ and cool crystallization of PET in blend, being ≈120°C as determined by the scanning spectroscopy technique). For a quantitative estimation of this effect, Table 3 gives $\Delta G'_{100}$ values which approximately correspond to G' minimum values of the materials when PET in blends undergoes devitrification.

After PET was devitrified and the blend was heated to ≈120°C, the amorphous portion of this polymer undergoes cool crystallization, and G' values of the material rise (Figure 1, Table 3). The presence of MDI in the blend material causes PET cool crystallization to proceed at a slower rate up to complete stopping in PET/PC – 75%/(PP/EPDM) – 5%/MDI – 1% blends (for these blends $\Delta G'_{cc} = 0$, Table 3). It can be seen that a rise in $\Delta G'_{100}$ has been caused by a more active interphase (segmental) interaction between the amorphous PC and amorphous phase of the devitrified PET. It is owing to stronger adhesion between the phases – and, probably, to partial mutual dissolution of the components that restricts segmental mobility – that PET cool crystallization is either retarded or suppressed in blends containing MDI. Some earlier works had described the determinative effect of segmental mobility on crystallizability of partly crystalline thermoplastics [21–23].

3.3. Results obtained by differential scanning calorimetry technique

It was established earlier that mechanical properties of PET-based blend materials much depend on the tendency of this polymer to crystallize. An increase

Table 4. DSC-results obtained for polyester materials

Composition No	Cool crystallization at heating		Melting		Crystallization at melt cooling		a[a] [%]
	$T_{c\,cr}$ [°C]	$\Delta H_{c\,cr}$ [J/g]	T_m [°C]	ΔH_m [J/g]	T_{cr} [°C]	ΔH_{cr} [J/g]	
1	130.4	28.2	253.3	44.1	194.4	27.7	11.0
3	139.5	15.5	251.0	25.2	177.8	25.9	9.5
4	143.6	13.1	252.8	18.8	182.3	25.8	8.2
5	139.0	7.4	249.5	9.2	179.9	8.6	5.5
6	145.3	12.0	244.0	21.1	165.5	29.3	8.9
7	146.6	10.8	248.9	13.4	169.0	14.5	3.9
8	148.0	4.5	252.5	5.7	160.7	8.5	3.4

[a]Crystallinity $a = (\Delta H_m - \Delta H_{c\,cr}) \cdot 100/(k \cdot \Delta H_m^*)$, where ΔH_m is latent melting heat, $\Delta H_{c\,cr}$ is latent heat of cool crystallization, $\Delta H_m^* = 144.664$ J/g is latent melting heat of PET with 100%-crystallinity [19], k is PET concentration (in wt parts) in the material

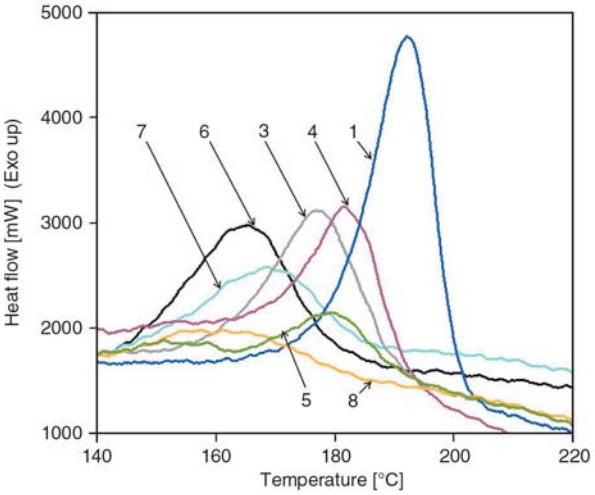

Figure 2. DSC-curves for cooling polyester blends

in the rate of crystallization and in crystallinity of the PET-component can result in a decrease in the blends plasticity and impact strength [24].

The results of analysis of PET crystallizability for tested blend materials are compared with initial polyester in Figure 2 and Table 4. The most important result of DSC-analysis is that the presence of MDI leads to rate retardation of crystallization and a lower crystallinity in a blend. The severity of MDI influence upon PET crystallizability was found to depend on the blend composition: the higher the PC concentration in the blend, the stronger the influence of MDI. This can be explained by the fact that in PET/PC/(PP/EPDM) ternary blends, PET undergoes crystallization at a slower rate, in comparison with pure polyester, because of interaction with PC-component [2].

The influence of MDI on PET crystallization in melt is especially easily visualized when analyzing DSC-curves of cooling. It can be seen in Figure 2 and Table 4 that in comparison with pure PET and a binary blend, the extent of melt overcooling reaches 20°C in order to ensure PET crystallization.

Thus in MDI – modified blends, diisocyanate acts as a chain extender and increases the PET molecular weight. It also interacts with terminal groups of PET and PC macromolecules, and obviously is helpful in forming copolymers. As a result the PET molecular mobility is restricted causing PET crystallization to proceed at a slower rate. The introduction of MDI in a PET/PC/(PP/EPDM) system may be one of the effective ways to make PET amorphous in the material.

Cuts of blends were made in liquid nitrogen and SEM-images (Figure 3) were analyzed to reveal that all of the blends morphologically look identical. Within a PET/PC quasi-homogeneous matrix, PP/EPDM forms sphere-like particles of a maximum size between some fractions of a micrometer up to 3 to 4 μm. Larger particles are relatively few. In these micrographs it is impossible to distinguish and identify phases of the composites independently of the phase structure of the materials because the interaction between PET and PC is intensive and they partly compatible in the blends investigated. No traces of a foreign phase are present on PP/EPDM particles which implies that there are no strong specific interactions between the impact strength modifier used and PET/PC blend matrix irrespective of the type and phase structure of the blends. It appears, therefore, that MDI modifies predominantly the basic components of the PET/PC blend matrix and not PP/EPDM and its interaction with the polyester matrix.

4. Conclusions

The reactive blending of PET, PC, 5 wt% of impact strength modifier – PP/EPDM – and MDI – 1wt% has been observed to cause great variations in the molecular structure and values of main properties

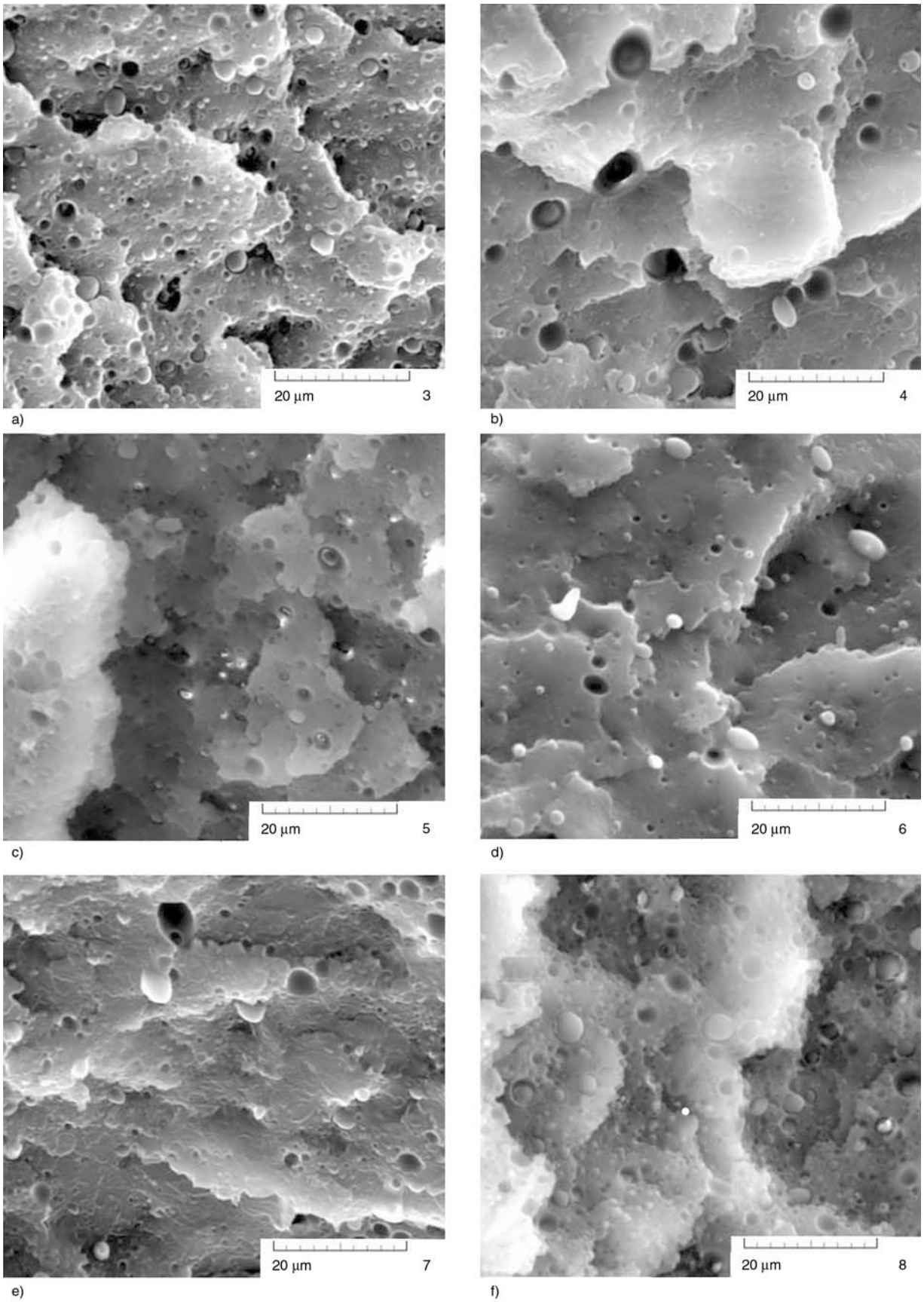

Figure 3. SEM-images (a–f) of polyester blend sections (3–8) cut under liquid nitrogen

of the materials under discussion. The addition of MDI leads to increased melt viscosity of the material (decreased MFI values) which can be explained by increased molecular weights of the components; PET crystallization proceeds at a lower rate. MDI improves compatibility of PET and PC in PET/PC/(PP/EPDM) ternary blends. This modifier causes a substantial rise in the dynamic shear modulus within the region of PET high elastic state (over the temperature range between $T_{g\,\mathrm{PET}}$ and temperature of PET cool crystallization). It also promotes approach of PET and PC glass transition temperatures; the processes of PET cool crystallization and crystallization from melt become retarded. MDI does not cause a noticeable influence on the blend morphology and on the character of interaction between the PP/EPDM disperse phase and PET/PC blend matrix.

References

[1] Samious C. K., Kalfoglou N. K.: Compatibility characterization of polycarbonate/copolyester blends. Polymer, **41**, 5759–5767 (2000). DOI: 10.1016/S0032-3861(99)00803-4

[2] Pesetskii S. S., Jurkowski B., Koval V. N.: Polycarbonate/polyalkylene terephthalate blends: Interphase interactions and impact strength. Journal of Applied Polymer Science, **84**, 1277–1285 (2002). DOI: 10.1002/app.10472

[3] Lee S-S., Jeong H. M., Jho J. Y., Ahn T. O.: Miscibility of poly(ethylene terephthalate)/poly(estercarbonate) blend. Polymer, **41**, 1773–1782 (2000). DOI: 10.1016/S0032-3861(99)00328-6

[4] Kong Y., Hay J. N.: Miscibility and crystallization behavior of poly(ethylene terephthalate)/polycarbonate blends. Polymer, **43**, 1805–1811 (2002). DOI: 10.1016/S0032-3861(01)00772-8

[5] Pesetskii S. S., Koval V. N., Starzhynsky V. E.: Method for making impact resistant composition. Russian Patent 2028335, Russia (1995).

[6] Zimmerman H., Kim N. T.: Investigation on thermal and hydrolytic degradation of poly(ethylene terephthalate). Polymer Engineering and Science, **20**, 680–683 (1980). DOI: 10.1002/pen.760201008

[7] Karger-Kocsis J.: Recycling options for post-consumer PET and PET-containing wastes by melt blending. in 'Handbook of Thermoplastic Polyesters' (ed.: Fakirov S.) Wiley-VCH, Weinheim, Vol 2, 1291–1318 (2002).

[8] Shima T., Urasaki T., Oka I.: Improved process for polycondensation of high-molecular-weigh poly(ethylene terephthalate) in the presence of acid derivatives. Advances in Chemistry, **128**, 183–207 (1973).

[9] Buxbaum L. H.: Solid-state polycondensation of poly(butylene terephthalate). Journal of Applied Polymer Science: Applied Polymer Symposium, **35**, 59–66 (1979).

[10] Inata H., Matsumura S.: Chain extenders for polyesters. I. Addition-type chain extenders reactive with carboxyl and groups of polyesters. Journal of Applied Polymer Science, **30**, 3325–3337 (1985). DOI: 10.1002/app.1985.070300815

[11] Inata H., Matsumura S.: Chain extenders for polyesters. II. Reactivities of carboxyl-addition type chain extenders: Bis cyclic-imino-ethers. Journal of Applied Polymer Science, **32**, 5193–5202 (1986). DOI: 10.1002/app.1986.070320534

[12] Inata H., Matsumura S.: Chain extenders for polyesters. III. Addition-type nitrogen-containing chain extenders reactive with hydroxyl end croups of polyesters. Journal of Applied Polymer Science, **32**, 4581–4594 (1986). DOI: 10.1002/app.1986.070320423

[13] Inata H., Matsumura S.: Chain extenders for polyesters. IV. Properties of the polyesters chain-extended by 2.2'-bis (2-oxasoline). Journal of Applied Polymer Science, **33**, 3069–3079 (1987). DOI: 10.1002/app.1987.070330838

[14] Japon S., Boogh L., Leterrier Y., Mànson J-A. E.: Reactive processing of poly(ethylene terephthalate) modified with multifunctional epoxy-based additives. Polymer, **41**, 5809–5818 (2000). DOI: 10.1016/S0032-3861(99)00768-5

[15] Villalobos M., Awojulu A., Greeley T., Turco G., Deeter G.: Oligomeric chain extenders for economic reprocessing and recycling of condensation plastics. Energy, **31**, 3227–3234 (2006). DOI: 10.1016/j.energy.2006.03.026

[16] Bikiaris D. N., Karayannidis G. P.: Thermomechanical analysis of chain extended PET and PBT. Journal of Applied Polymer Science, **60**, 55–61 (1996). DOI: 10.1002/(SICI)1097-4628(19960404)60:1<55::AID-APP7>3.0.CO;2-U

[17] Bikiaris D. N., Karayannidis G. P.: Chain extension of polyesters PET and PBT with *N*,*N*'-bis(glycidylester)pyromillitimides. I. Journal of Polymer Science Part A: Polymer Chemistry, **33**, 1705–1714 (1995). DOI: 10.1002/pola.1995.080331017

[18] Inata H., Matsumura S.: Chain extenders for polyesters. V. Reactivities of hydroxyl-addition-type chain extender 2,2'-bis(4h-3,1-benzoxazin-4-one). Journal of Applied Polymer Science, **34**, 2609–2617 (1987). DOI: 10.1002/app.1987.070340724

[19] Tang X., Guo W., Yin G., Li B., Wu C.: Reactive extrusion of recycled poly(ethylene terephthalate) with polycarbonate by addition of chain extender. Journal of Applied Polymer Science, **104**, 2602–2607 (2007).
DOI: 10.1002/app.24410

[20] Pesetskii S. S., Jurkowski B., Storozhuk I. P., Koval V. N.: Blends of polycarbonate and polysulphone-polydimethyl-siloxane block copolymers: Analysis of compatibility and impact strength. Journal of Applied Polymer Science, **73**, 1823–1834 (1999).
DOI: 10.1002/(SICI)1097-4628(19990906)73:10<1823::AID-APP1>3.0.CO;2-7

[21] Pol D., Newman S.: Polymer blends. Academic Press, New York (1978).

[22] Pesetskii S. S., Jurkowski B., Olkhov Yu. A., Bogdanovich S. P., Koval V. N.: Influence of cooling rate on structure of PA 6. European Polymer Journal, **41**, 1380–1390 (2005).
DOI: 10.1016/j.eurpolymj.2004.12.009

[23] Pesetskii S. S., Bogdanovich S. P., Koval V. N.: Structural features and stability of amorpholous phase in polyamide 6 blocks. Materials, Technologies, Instruments, **11**, 29–34 (2006).

[24] Yu Z-Z., Yang M-S., Dai S-C., Mai Y-W.: Toughening of recycled poly(ethylene terephthalate) with a maleic anhydride grafted SEBS triblock copolymer. Journal of Applied Polymer Science, **93**, 1462–1472 (2004).
DOI: 10.1002/app.20592

eXPRESS Polymer Letters Vol.3, No.10 (2009) 615–620
Available online at www.expresspolymlett.com
DOI: 10.3144/expresspolymlett.2009.77

Effects of polyester fibers and gamma irradiation on mechanical properties of polymer concrete containing $CaCO_3$ and silica sand

E. A. Bobadilla-Sánchez[1], *G. Martínez-Barrera*[1,2], *W. Brostow*[2*], *T. Datashvili*[2]

[1]Laboratorio de Investigación y Desarrollo de Materiales Avanzados (LIDMA), Facultad de Química, Universidad Autónoma del Estado de México, Km. 12 de la carretera Toluca-Atlacomulco, San Cayetano 50200, Mexico
[2]Laboratory of Advanced Polymers & Optimized Materials (LAPOM), Department of Materials Science and Engineering and Department of Physics, University of North Texas, 1150 Union Circle # 305310, Denton TX 76203-5017, USA

Received 17 March 2009; accepted in revised form 3 July 2009

Abstract. While mineral concretes belong to the oldest composites used by mankind, in an increasing number of applications their compression strength σ_c and compressive strain at yield point ε_Y are insufficient. Better results can be achieved with polymer concretes (PCs). We use a polymer concrete (PC): an unsaturated polyester resin as the matrix, $CaCO_3$ and silica sand. Moreover, we have applied two further methods to improve its mechanical properties: reinforcement with polyester fibers and gamma irradiation with a ^{60}Co source. A non-irradiated PC with 5 wt% $CaCO_3$ has σ_c = 74 MPa, an irradiated sample with optimized $CaCO_3$ contents 122 MPa. Scanning electron micrographs show that irradiation increases the interface areas between the fibers and the matrix. Improvements from 47 to 176% in ε_Y values are achieved with respect to the conventional PC without fibers, non-irradiated and containing only one mineral component.

Keywords: *mechanical properties, polymer concrete, fiber reinforcement, gamma irradiation*

1. Introduction

A large variety of concretes is based on a variety of cements [1–3]. Mineral concretes – used for a very long time – typically contain structural defects, including delaminations and voids. Polymer concretes (PCs) with a polymeric resin matrix have better mechanical properties than mineral concrete. Thus, PCs are used to make reinforced slabs, overlays for highway pavements and bridge decks, pipe coatings – as well as in repairing deteriorated mineral concretes (Portland cement concrete).

The key criteria for usability of a concrete for a specific application are compression strength σ_c and compressive strain at yield point ε_Y. While PCs have these parameters better than mineral concretes, in potential applications still better values of σ_c and ε_Y than those presently available are required. At least three options deserve consideration:

a) Use of fibers for reinforcement. There is a large variety of reinforcements for polymeric matrices [4–6]. The work of San-Jose *et al*. suggests using fibers or other objects with irregular shapes and large sizes since the adhesion between the reinforcement and the matrix depends on the physical interactions between them [7]. Similarly, elongated objects provide more improvement of mechanical properties that spherical ones [8]. This should not be surprising; Kopczynska and Ehrenstein [9] discuss how interfaces largely determine properties of multiphase materials.

b) Use of small particles as a dispersed phase. Special attention to the shape, size and number of

*Corresponding author, e-mail: wbrostow@yahoo.com

aggregates is needed because the aggregates act as stress concentration points. Some PCs contain only one aggregate, others more than one, such as a PC with quartz fine sand, quartz gravel, quartz powder and chalk [7]. Moreover, the interface surface area can be enhanced by decreasing the size of the aggregate particles (inclusive to nano-dimensions), so as to produce strong cohesion; undesirable agglomeration of the particles has to be avoided. The Zagreb group has shown that $CaCO_3$ with surface modification provides stronger bonding to polymers largely via electrostatic forces; moreover, $CaCO_3$ without pre-treatment provides stronger interfacial adhesion than after a treatment [10]. An improvement of the attraction between the polymer and the aggregates can also be achieved by adding a coupling agent such as silane to the monomer. This lowers the extent of pore formation and causes a decrement in stiffness [11]. Our main interest consists in grafting polymers onto aggregates surfaces.
c) Irradiation – by a variety of sources [12–19]. Gamma irradiation has several advantages over conventional curing processes: I) no catalyst or additives are needed to initiate the reaction; II) the initiation is homogenous throughout the system; III) it can be performed at any temperature and be interrupted at a chosen reaction time; IV) the polymer can be analyzed at selected reaction stages; and V) the temperature during reaction initialization is maintained – as contrasted with highly exothermic curing without irradiation. Moreover, the gamma irradiation applied to polymers causes three different processes: chain scission, crosslinking or grafting. Which of these processes prevails depends on the nature of irradiation, chemical nature of the polymer and the applied dose [20].
In this situation we have investigated a PC containing an unsaturated polyester resin, $CaCO_3$ and silica sand – with inclusion of polyester fibers and gamma irradiation for their further reinforcement.

2. Materials and procedures

Our PC specimens consist of natural silica, calcium carbonate (GOSA™, Atizapan, Mexico), and a commercial unsaturated pre-accelerated orthophthalic polyester resin, a viscous liquid with 30% styrene monomer (Polylite 32493-00™, Reichhold, Atlacomulco, Mexico). Methyl ethyl ketone peroxide is the initiator of free-radical polymerization (1 ml/100 g polyester). The sizes of silica sand particles were of 150, 212 and 355 μm (mesh 100, 70 and 45, respectively), and for $CaCO_3$ particles 75 μm (mesh 200). The standard mixing procedure according to the ASTM C305 was followed. It consists of two stages, mixing for 1.0 minutes at the paddle speed of 140 rpm, and followed by a total of 1.5 minutes at the speed of 285 rpm. The compositions of PCs are summarized in Table 1.
After mixing, PC cubic specimens with the side of 5.0 cm were kept at 23.0±3.0°C for 72 hours. Six different lots were elaborated (labeled I to VI) on different days, each one containing 15 samples. That is, for each type of PC (see Table 1) 15 concrete specimens were made.
For obtaining fiber-containing PCs, we have also followed the ASTM C305 mixing method, adding in the two stages the polyester fibers (Gütermann Polygal, Cuernavaca, Mexico) with diameters between 30 and 40 μm and 20 mm long. The compositions of PCs with fibers are listed in Table 2. Three different lots were elaborated (labeled VII to IX) on different days, each one contained 15 samples. That is, for each polyester-fiber content 15 concrete specimens were made.
The PC specimens were subjected to gamma irradiation using a ^{60}Co source at five different dosages: 0, 5, 10, 50 and 100 kGy at the rate of 2.48 kGy/h in air at room temperature. For comparison analysis, polyester fibers alone were irradiated under the same conditions, in packets of 50 fibers in a capillarity tube. The source was a 651 PT Gammabeam Irradiator, manufactured by Atomic Energy of Canada Ltd. (now NORDION, Chalk River,

Table 1. Compositions of the polymer concrete specimens

Specimen (type)	Polyester resin [wt%]	$CaCO_3$ [wt%]	Silica sand [wt%]
I	20	5	75
II	20	12	68
III	20	25	55
IV	20	37	43
V	20	50	30
VI	20	60	20

Table 2. Compositions of the fiber + polymer concrete specimens

Specimen	Polyester resin [wt%]	$CaCO_3$ [wt%]	Silica sand [wt%]	Polyester fiber [wt%]
VII	20.0	60.0	19.90	0.10
VIII	20.0	60.0	19.75	0.25
IX	20.0	60.0	19.60	0.40

Ontario), and located at the Institute of Nuclear Sciences of the National Autonomous University of Mexico.

Compressive strength testing was performed in an Instron Universal Testing machine Model 1125, according to the ASTM C-109M standard. The charge speed used was of 120 kg/s, holding the charge until reaching the maximum value to assure the test reliability.

3. Compression strength

In Figure 1 we show the compressive strength values σ_c for PCs without fibers. For non-irradiated PCs, σ_c values increase according to the $CaCO_3$ and silica sand concentrations; the lowest increment is seen for PC type I and the highest for PC type VI (see Table 1). That is, the compressive strength values increase when increasing $CaCO_3$ and decreasing silica sand concentration at the same time. The compressive strength values vary from 74 to 107 MPa.

Similar behavior is seen in irradiated PCs, with the values varying from 85 to 122 MPa. The highest value of 122 MPa is achieved for PC type V (50/30 $CaCO_3$/silica sand wt% ratio), irradiated at 100 kGy. This result constitutes an improvement of 64% with respect to the minimum value obtained for non-irradiated PC type I.

The next step was evaluation of effects of polyester fibers incorporation into the PC. We have chosen those PCs in which variations in the compressive strength values were minimal. Thus, PC type VI was selected (see Figure 1) since the differences did not exceed 8%.

The results for polyester-fiber PCs are shown in Figure 2. The σ_c values in non-irradiated samples are lowered by introduction of the fibers. However

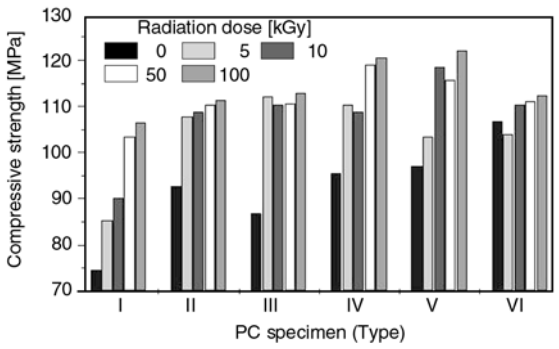

Figure 1. Compressive strength of different types of PCs

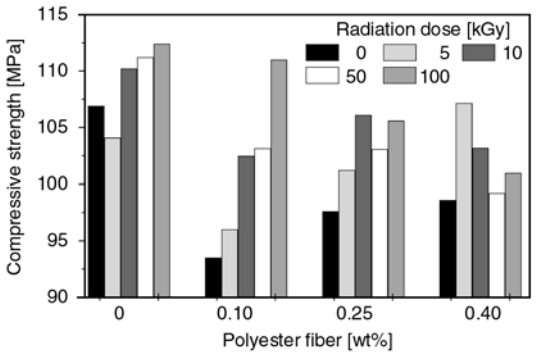

Figure 2. Compressive strength of fiber-reinforced PCs with varying polyester fiber concentrations

and as expected, σ_c values depend on a combination of the fiber concentration and the applied radiation. By following the fiber concentrations, a different behavior is seen. For PCs with 0.1 wt% of fiber, the compressive strength values increase along with increasing applied radiation dose. For 0.25 wt%, the compressive strength increases up to 10 kGy, then it decreases at 50 kGy, and finally it increases again at 100 kGy; for 0.4 wt%, the highest value is seen at 5 kGy. In this sense, we can describe this σ_c behavior as periodic. More notable is the periodicity if a fixed radiation dose is followed.

For fiber-PCs, the highest σ_c value is seen for 0.1 wt% fibers and 100 kGy of radiation dose. Recall that in Figure 1 the highest overall σ_c value is also for 100 kGy. This can be related to effects of irradiation on polyester resins reported by Jurkin and Pucić [18]. At 5 kGy the irradiated polyester resin abruptly changes from a viscous liquid into a hard thermoset solid (3-D network), reducing the polymer chains mobility [18] – what enhances σ_c. Between 5 and 50 kGy, the changes can be attributed to behavior of the fibers since the polyester resin retains its dimensional stability. For doses exceeding 50 kGy, the polyester resin begins to deteriorate [18] and lower σ_c values are seen.

As said, the σ_c values go from 74 to 107 MPa for non-irradiated PCs when varying the $CaCO_3$ and silica sand concentration; the respective range for irradiated PCs is 85–122 MPa. We recall in this context also earlier results for the same polyester resin containing whether $CaCO_3$ or silica sand. The present results are lower than those reported for PCs containing only $CaCO_3$ (from 127 to 135 MPa) [21], but higher than those obtained using silica sand only (from 62 to 68 MPa) [22]. Thus, in irradi-

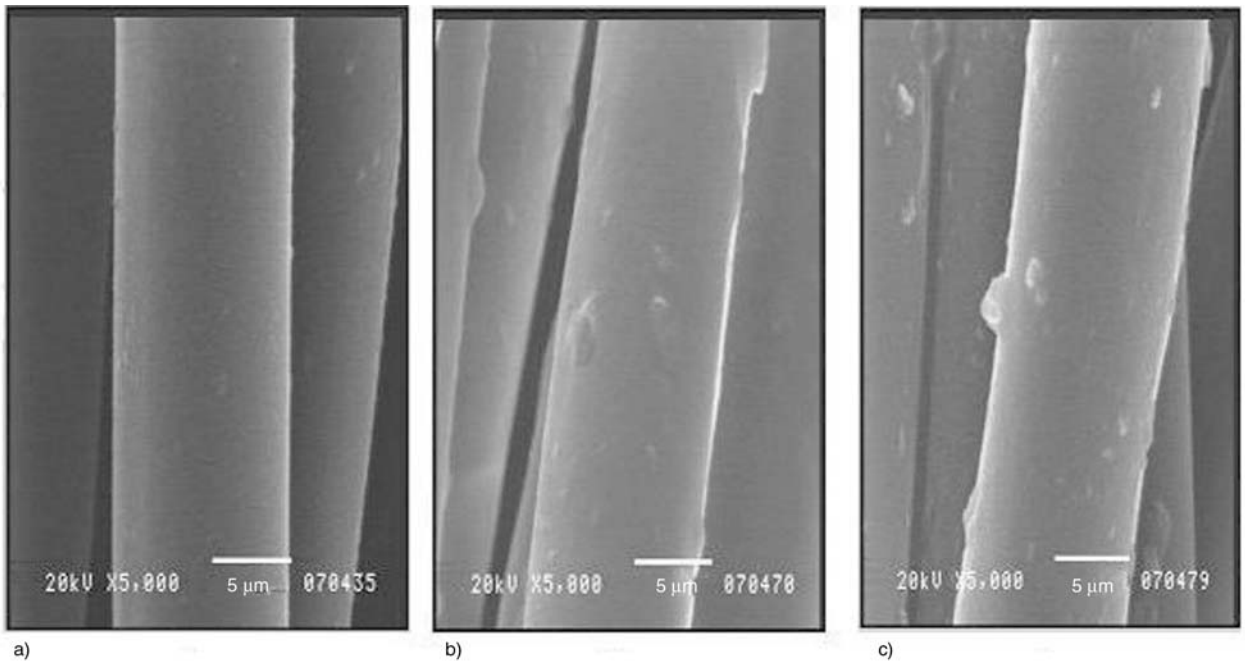

Figure 3. SEM Micrographs of polyester fibers: non-irradiated (a), irradiated at 10 kGy (b), and irradiated at 100 kGy (c)

ated materials $CaCO_3$ particles support more compression strength than the silica sand particles.

Changes on surfaces of irradiated polyester fibers were observed by scanning electron microscopy (SEM). First the fibers were vacuum-coated with carbon (3–10 nm thickness) in a vacuum pump at 50 mTorr. A JEOL model JSM-5200 was used in the secondary electron mode. For non-irradiated fibers smooth and homogeneous surfaces are seen (Figure 3a). For 10 kGy several 'particles' are observed on the fiber surface (Figure 3b). At 100 kGy, SEM reveals more such particles (Figure 3c). Apparently irradiation causes a fractional degradation of the fiber surfaces – manifested as formation of the 'particles'.

Chain scission results in formation of low molecular weight chains at higher doses, providing more contact points and thus improving physical adhesion between the fibers and the concrete. As one of the consequences, the concrete will resist larger loads by inclined forces – oriented at some angles relative to the longitudinal axes of the fibers.

4. Compressive strain at yield point

We now turn to the compressive strain at yield point ε_Y results. For non-irradiated PCs we see three well defined stages: increment-decrement-increment associated with $CaCO_3$ and silica sand concentration (Figure 4). This periodic behavior

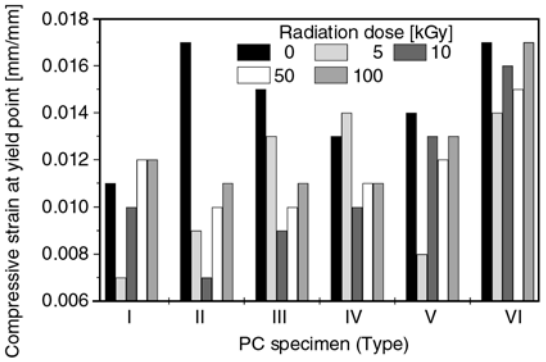

Figure 4. Compressive strain at yield point of different types of PCs

seems to be the result of a competition between two reinforcing components, $CaCO_3$ and silica sand.

For irradiated PCs two different types of behavior are seen: I) three well-defined stages, with a increment-decrement-increment sequence – observed only in PCs irradiated at 5 kGy, II) two stages, with a decrement-increment sequence, observed in PCs irradiated at 10, 50 and 100 kGy. The values for irradiated and non-irradiated PCs vary from 0.007 to 0.017 mm/mm. Apparently, the strain is supported by the polyester resin – a polymeric material - more than by mineral components $CaCO_3$ and silica sand.

The highest values for PCs without fibers are seen for PC type VI (20/60/20 resin/$CaCO_3$/silica ratio). Thus, this material was chosen as a convenient reference material for evaluation of effects of gamma

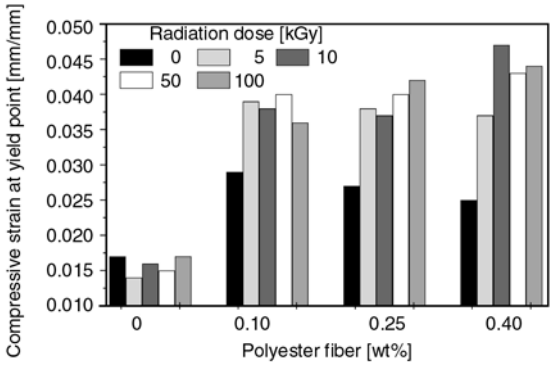

Figure 5. Compressive strain at yield point of fiber-reinforced PCs with varying polyester fiber concentrations

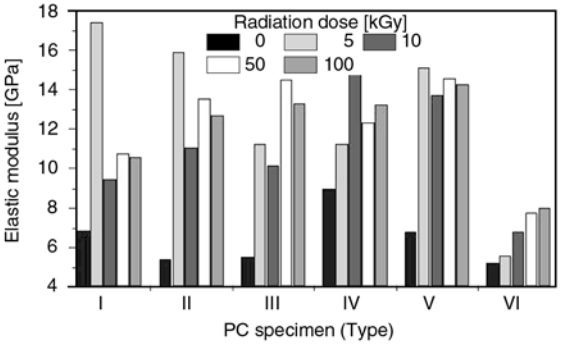

Figure 6. Compression modulus of elasticity E_c of different types of PCs

irradiation after addition of polyester fibers. The addition of the fibers, even only 0.1%, increases ε_Y tremendously, see Figure 5. The compressive strain values for fiber-PCs ranging from 0.025 to 0.047 mm/mm are higher than standard values reported in the literature for polyester-based PC (0.010 mm/mm) [20]. We note improvements from 47 to 176% with respect to conventional PCs (without fibers and non-irradiated).

We recall that the materials brittleness B is inversely proportional to ε_Y [23, 24]. If the dynamic storage modulus E' values (E' also appears in the definition of B) are comparable, our materials with higher ε_Y values are less brittle. Thus, irradiation of fibers causes material softening, and they sustain the compressive strain much more than the polyester resin.

Compare now our ε_Y range of 0.025–0.047 mm/mm with results for PCs with the same polyester resin but containing one mineral, such as PC with $CaCO_3$ (0.01–0.016 mm/mm [21]) or with silica sand (0.006–0.013 mm/mm [22]); we conclude that a combination of two different minerals and one kind of polymeric fibers result in higher compressive strain values that in PCs containing one mineral.

5. Compression modulus of elasticity

In Figure 6 we show values of the compression modulus of elasticity E_c for PCs without fibers. Also here periodic behavior is seen. For non-irradiated PCs the values range from 5.4 to 8.9 GPa, thus higher than our result for pure polyester resin, E_c = 3.9 GPa [20]; as expected, adding the minerals increases E_c.

Consider now E_c values for irradiated PCs. There is a large variety of behavior, no general pattern; the E_c ranging from 8.6 to 17.4 GPa which are higher than values reported for polyester-based PCs (6.7 GPa) [22]. The highest value is for PC with 5% of $CaCO_3$ and 75% of silica sand irradiated at 5 kGy. This means an improvement of 159% respect to standard value reported in the literature [22].

The addition of polyester fibers lowers E_c dramatically (results not included here for brevity). Both irradiated and non-irradiated PCs have results in the range from 3.1 to 3.7 GPa. Hence, the addition of the fibers increases ductility.

We have obtained notable improvements in the compressive strength and compressive strain at yield point – a consequence of contributions of irradiation, two aggregates ($CaCO_3$ and silica sand) as well as polyester fibers. Such behavior is not seen in polyester-based PCs with one aggregate.

Acknowledgements

Financial support by the National Council of Science and Technology of Mexico (CONACyT), Mexico City (Grant # 49899/2005) and by Hispanic and Global Studies Initiatives Fund of the University of North Texas, Denton, are acknowledged.

References

[1] Mindess S.: Concrete materials. Journal of Materials Education, **5**, 983–1046 (1983).

[2] Regourd M.: New progress in inorganic building materials. Journal of Materials Education, **9**, 201–228 (1987).

[3] Roy D. M., Scheetz B. E., Silsbee M. R.: Processing of optimized cements and concretes via particle packing. Journal of Materials Education, **15**, 1–16 (1993).

[4] Rabello M.: Additives for Polymers. Artliber, São Paulo (2000).
[5] Pisanova E., Zhandarov S.: Fiber-reinforced heterogeneous composites. in 'Performance of plastics' (ed.: Brostow W.), Hanser, Munich, 461–486 (2000).
[6] Bismarck A., Mohanty A. K., Aranberri-Askargorta I., Czapla S., Misra M., Hinrichsen G., Springer J.: Surface characterization of natural fibers; Surface properties and the water up-take behavior of modified sisal and coir fibers. Green Chemistry, **3**, 100–107 (2001). DOI: 10.1039/b100365h
[7] San-José J. T., Vegas I., Ferreira A.: Reinforced polymer concrete: Physical properties of the and static/dynamic bond behaviour. Cement and Concrete Composites, **27**, 934–944 (2005). DOI: 10.1016/j.cemconcomp.2005.06.004
[8] Roslaniec Z., Broza G., Schulte K.: Nanocomposites based on multiblock polyester elastomers (PEE) and carbon nanotubes (CNT). Composite Interfaces, **10**, 95–102 (2003). DOI: 10.1163/156855403763586819
[9] Kopczynska A., Ehrenstein G. W.: Polymeric surfaces and their true surface tension in solids and melts. Journal of Materials Education, **29**, 325–340 (2007).
[10] Leskovac M., Kovacevic V., Lucic Blagojevic S., Vsarljko D., Volovskek V.: Pre-treatment of $CaCO_3$ nanofiller by irradiation in the presence of vinyl monomers. e-Polymers, no. 033 (2004).
[11] Brostow W.: Performance of plastics. Hanser, Munich (2000).
[12] Brocka Z., Schmachtenberg E., Ehrenstein G. W.: Radiation crosslinking engineering thermoplastics for tribological applications. in 'Proceedings of SPEANTEC 2007, Cincinnati USA' 1690–1694 (2007).
[13] Nair P. D., Sreenivasan K., Jayabalan M.: Multiple gamma radiation sterilization of polyester fibres. Biomaterials, **9**, 335–338 (1988). DOI: 10.1016/0142-9612(88)90029-4
[14] Fink D.: Fundamentals of ion-irradiated polymers. Springer, Berlin (2004).
[15] Brostow W., Castano V. M., Horta J., Martinez-Barrera G.: Gamma irradiation effects on impact strength and thermal properties of SBR-toughened polystyrene. Polimery, **49**, 9–14 (2004).
[16] Brostow W., Castaño V. M., Martinez-Barrera G.: Gamma irradiation effect on polystyrene+SRB blends: Morphology and hardness. Polimery, **50**, 27–32 (2005).
[17] Martinez-Barrera G., Vigueras-Santiago E., Hernandez-Lopez S., Menchaca-Campos C., Brostow W.: Concrete reinforced with irradiated nylon fibers. Journal of Materials Research, **21**, 484–491 (2006). DOI: 10.1557/jmr.2006.0058
[18] Jurkin T., Pucić I.: Post-irradiation crosslinking of partially cured unsaturated polyester resin. Radiation Physics and Chemistry, **75**, 1060–1068 (2006). DOI: 10.1016/j.radphyschem.2006.04.001
[19] Menchaca-Campos C., Martínez-Barrera G., Resendiz M. C., Lara V. H., Brostow W.: Long term irradiation effects on gamma-irradiated Nylon 6, 12 fibers. Journal of Materials Research, **23**, 1276–1281 (2008). DOI: 10.1557/jmr.2008.0152
[20] Martínez-Barrera G., Brostow W.: Fiber-reinforced polymer concrete: Property improvement by gamma irradiation. in 'Gamma radiation effects on polymeric materials and its applications' (ed.: Barrera C.) Research Signpost, Kerala, 27–44 (2009).
[21] Martínez-Barrera G., Espinosa-Pesqueira M. E., Brostow W.: Concrete+polyester+$CaCO_3$: Mechanics and morphology after gamma irradiation. e- Polymers, no. 083 (2007).
[22] Martínez-Barrera G., Texcalpa-Villarruel U., Vigueras-Santiago E., Hernández-López S., Brostow W.: Compressive strength of gamma-irradiated polymer concrete. Polymer Composites, **29**, 1210–1217 (2008). DOI: 10.1002/pc.20432
[23] Brostow W., Hagg Lobland H. E., Narkis M.: Sliding wear, viscoelasticity and brittleness of polymers. Journal of Materials Research, **21**, 2422–2428 (2006). DOI: 10.1557/jmr.2006.0300
[24] Brostow W., Hagg Lobland H. E.: Predicting wear from mechanical properties of thermoplastic polymers. Polymer Engineering and Science, **48**, 1982–1985 (2008). DOI: 10.1002/pen.21045

eXPRESS Polymer Letters Vol.3, No.10 (2009) 621–629
Available online at www.expresspolymlett.com
DOI: 10.3144/expresspolymlett.2009.78

Scratch resistance of a polycarbonate + organoclay nanohybrid

A. Arribas[1], *M.-D. Bermúdez*[2], *W. Brostow*[3,*], *F. J. Carrión-Vilches*[2,3], *O. Olea-Mejía*[3,4]

[1]Centro Tecnológico del Calzado y Plástico de la Región de Murcia, Polígono Industrial Las Salinas, Avda. Europa 4-5, 30840 Alhama de Murcia, Spain
[2]Grupo de Ciencia de Materiales e Ingeniería Metalúrgica, Departamento de Ingeniería de Materiales y Fabricación, Universidad Politécnica de Cartagena, Campus de la Muralla del Mar, C/ Doctor Fleming s/n, 30202 Cartagena, Spain
[3]Laboratory of Advanced Polymers & Optimized Materials (LAPOM), Department of Materials Science & Engineering, University of North Texas, 1150 Union Circle # 305310, Denton, TX 76203-5017, USA
[4]Centro de Investigación en Química Sustentable (CIQS), Facultad de Química, Universidad Autónoma del Estado de México, Km. 12 de la carretera Toluca-Atlacomulco, San Cayetano, C.P. 50120, Mexico

Received 17 March 2009; accepted in revised form 10 July 2009

Abstract. A polycarbonate-based nanohybrid has been created containing 1 wt% of Bentone 2010, an organically modified montmorillonite. A micro-section on the nanohybrid obtained using focused ion beam (FIB) and field emission scanning electron microscopy (FESEM) was employed to observe the orientation of the nanoclay inside a polycarbonate (PC) matrix in the cross-section FIB-milled face. A micro-scratch tester was used to measure the scratch resistance in terms of residual (healing) depth R_h under progressive load and in sliding wear. Effects of the number of scratches, normal load and scratch velocity have been evaluated as a function of nanoclay orientation. In sliding wear (multiple scratching along the same groove), our nanohybrid reaches residual depth values that remain constant after a certain number of scratches, a manifestation of strain hardening. The number of scratches to induce strain hardening decreases as the normal applied load increases. SEM was used to characterize deformation and wear mechanisms that operate on contacts and the results related to the wear data.

Keywords: *nanocomposites, polycarbonate, FIB, scratch resistance, wear resistance*

1. Introduction

There exists a belief that addition of nanoparticles to polymers results in improvement of a variety of properties of the matrix polymer. This statement is not always true. Thus, for epoxy + silica nanohybrids there is an improvement of both mechanical and tribological properties [1]. By contrast, for Polyamide 6 reinforced with multiwall carbon nanotubes (MWCNTs) there is an improvement of mechanical properties; however, scratch recovery is hampered by the presence of CNTs [2] while the scratch depths can be either shallower or deeper, depending on the CNTs diameter and also on functionalization. Thus, creation of polymer-based nanohybrids seems be a two-edged sword.

Fairly large amount of work has been expended on organoclay-containing hybrids. Thus, Xu *et al.* [3] have created such hybrids on the basis of thermoplastic polyurethanes (TPUs) and investigated their tribological behavior against steel. The presence of organoclay has improved resistance to rolling wear significantly. Dynamic friction decreased for TPUs with low hardness but increased for TPUs with high hardness – hence also here we are dealing with

*Corresponding author, e-mail: wbrostow@yahoo.com

a two-edged sword. In general, tribology of polymer-based materials (PBMs) is significantly more difficult than tribology of metals although some approaches that work have been developed [4–20]. In this situation, we have decided to investigate further effects of the presence of organoclay on tribological behavior an engineering polymer. In an earlier paper [13] some of us have demonstrated using transmission electron microscopy [TEM] that there is a preferential orientation of nanoclay in the polymer matrix. Apparently the orientation appears during the injection molding process due to high shear pressure in the melt.

2. Experimental

2.1. Materials

PC and PC + 1 wt% B2010 were prepared using Lexan LS2 from General Electric Plastics and Bentone 2010 (B2010), a quaternary ammonium-modified montmorillonite that was supplied by Elementis Specialties, and used as received. After mixing in the corresponding proportion, extrusion and injection molding were carried out to obtain samples of PC and PC + 1% B2010 as previously described [13].

2.2. Thermophysical properties

Differential scanning calorimetry (DSC) was performed using a Mettler Toledo DSC 822. Samples of 9.78 mg for PC and 14.01 mg for PC + 1% B2010 were heated above the glass transition temperature T_g, then kept at 300°C for 5 minutes, cooled, and a second heating run was made between 0 and 300°C at the heating rate of 20°C/min in nitrogen atmosphere, with the flow rate of 50 ml/min. Thermogravimetric analysis (TGA) to determine degradation temperatures T_d was carried out using a Mettler Toledo TGA SDTA 851 analyzer at the heating rate of 20°C/min from 30 to 950°C in an oxygen flow of 40 ml/min.

2.3. Hardness measurement

Hardness values were determined with a TH210 Shore D hardness tester.

2.4. Focused Ion Beam (FIB) & Field Emission Scanning Electron Microscopy (FESEM)

A FEI Nova 200 Dual Beam consisting of FIB and FESEM was used to obtain cross-sections of the materials in order to evaluate the dispersion, distribution and orientation of the nanoclay in relation to the melt flow direction during the process of the injection molding. The equipment combination was the same as used in earlier work [14], the source consisted of gallium ions. We have cut with FIB precise micro-sections before FESEM. The conditions of the micro-sectioning were 17 nA probe current and 15.0 kV accelerating voltage. The micro-sections with dimensions of 6.0×5.0×5.0 μm took 20 minutes at 52° of tilt, followed by 2 cycles of cleaning for 40 s.

2.5. Scratch testing

Specimens were tested using a CSM Micro-Scratch Tester (MST) following the procedure previously described [1, 2, 6, 15–17]. Sliding wear (repetitive scratching along the same groove) tests were performed as follows: normal load 5.0, 10.0 and 15.0 N; scratch length 5.0 mm; scratch velocity 2.5, 5.0 and 15.0 mm/min at room temperature. In progressive scratch testing, progressively increasing loads from 0.03 to 30.0 N were applied at 5.0 N/min rate along 5.0 mm of length. A conical diamond indenter was used in all the tests with the diameter of 200 μm and a cone angle of 120°. The results include the penetration (instantaneous) depth R_p and the residual (healing) depth R_h. Following the scratch test and a waiting period of 2 minutes to allow for viscoelastic recovery, the indentor makes a scan along the track scratch at 0.03 N contact load to determinate the residual depth. Repeated experiments have confirmed that the shallower residual depth in our viscoelastic materials is reached inside 2 minutes. Therefore, R_h values have in each case been determined 5 minutes after recording the R_p values.

2.6. Scanning electron microscopy (SEM)

SEM images of the scratch track were obtained using a Hitachi S3500 N scanning electron microscope. The samples were sputter coated with a thin

layer of gold in order to make them conductive with the aid of a SC7640 Sputter Coater from Polaron.

3. Hardness and thermophysical properties

Table 1 shows hardness values and thermophysical properties of the materials. Hardness values are very similar for both materials. The addition of 1 wt% B2010 increases thermal stability of PC, as can be seen by the degradation temperatures. Nanoclay layers provide a barrier action against heat diffusion – what improves the thermal stability of the nanohybrid [21].

The glass transition temperature decrease shows that nanoclay acts as a plasticizer of PC. Apparently, nanoclay particles increase the mobility of PC chains. In more detail: when a sequence of chain segments 'would like' to move, the surrounding chains form a barrier to the movement because of entanglements – a fact pointed out by Treloar long ago [22]. However, if the nearest environment of that sequence consists of clay particles, those particles can move away since there are no such constraints.

Figures 1a and 1b display FESEM images of the nanohybrid where the nanoclay platelets are largely aligned parallel (*L*) to the melt flow direction [23–25]. The observed orientation could be the result of the response of the nanoclay layers to high shear forces applied during the extrusion and injection of the specimen. In the following sections, the scratching resistance of the nanohybrid will be discussed in the longitudinal (*L*) direction parallel to the melt flow and in the transverse (*T*) direction perpendicular to the melt flow (Figure 1b). An energy-dispersive X-ray spectrum (EDS) of the nanoclay (Figure 1c) confirms the presence of the filler.

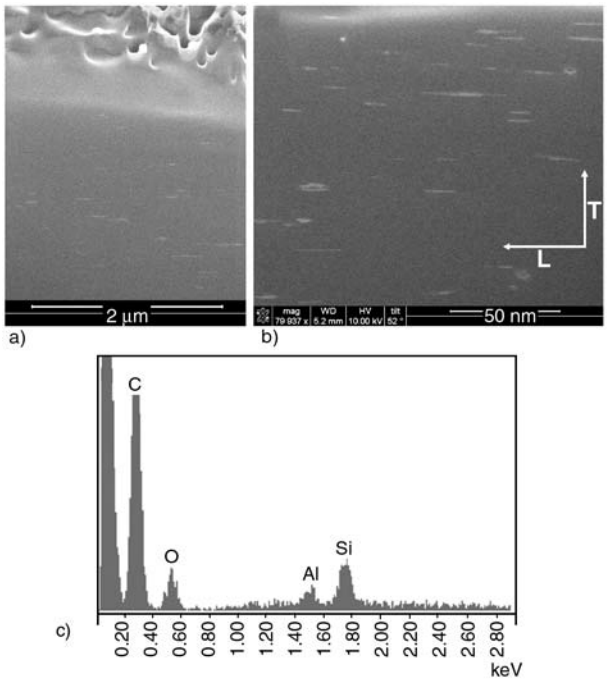

Figure 1. a) Image of Field Emission Scanning Electron Microscopy of a milled micro-section of PC + 1% B2010 using FIB technique; b) magnification of 1a showing longitudinal (*L*) and transverse (*T*) sliding directions with respect to nanoclay orientation; c) energy-dispersive X-ray spectrum (EDS) of the nanoclay

4. Scratching and sliding wear results

4.1. Progressive scratch testing

As discussed in an earlier paper [13], we have undertaken a study of the influence of nanoclay orientation when the sliding direction is either longitudinal (*L*) or transverse (*T*) to the orientation of the nanoclay (see Figure 1b). Figure 2 shows residual depth values as a function of scratch direction. A linear response to increased applied load is observed in all cases. In the longitudinal direction (Figure 2a), nanoclay reduces R_h with respect to neat PC, while R_h values are similar for both materials in the transverse direction (Figure 2b). For an explanation see the discussion of plasticizing behavior of nanoclay particles above in Section 3.

If we consider the reduction of R_h with load for the nanohybrid with respect to PC in the longitudinal direction (Figure 2c), we can fit the results to an exponential decay function (Equation (1)):

$$R_h \text{ reduction } [\%] = 10.64 + 61.10 \cdot e^{(-0.21 \cdot \text{Load})} \quad (1)$$

with good accuracy (the parameter $R = 0.983$). Thus, the presence of the nanoclay reinforcement is

Table 1. Hardness and thermal properties of the materials

Material	Hardness Shore D	T_g [°C]	T_d [°C]			
			1st step		2nd step	
			Onset	Midpoint	Onset	Midpoint
PC	81.3	145.1	475	504	552	565
PC + 1% B2010	81.8	133.6	494	510	572	608

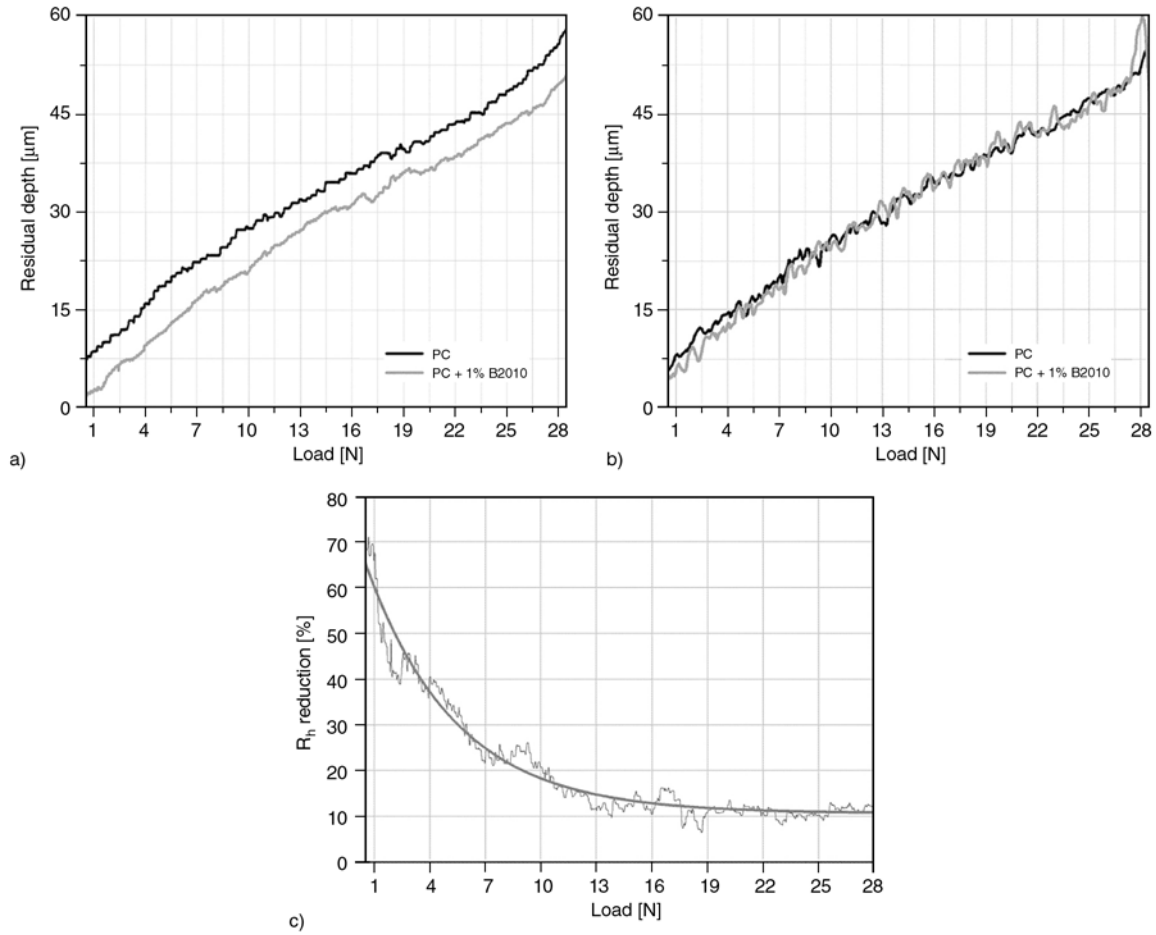

Figure 2. Residual depth under progressive load tests for PC and PC + 1% B2010 as a function of scratch direction: a) longitudinal; b) transverse; c) R_h reduction with load for the composite with respect to PC in the longitudinal direction

less effective as the applied load increases. Apparently, the first nanoclay particles put in have a larger effect on the mobility of macromolecular chains than the subsequent ones. The absence of slope changes in the R_h vs. load graphs in Figure 2a and 2b suggests that no fracture takes place during the progressive load tests.

Figure 3 shows the SEM micrographs of the tracks on neat PC (Figure 3a and 3c) and on the nanohybrid (Figure 3b and 3d), both in longitudinal and transverse directions. In the case of PC in the transverse direction (Figure 3c), we observe the presence of regular cracks inside the scratch groove. The cracks follow the original surface texture; we observe the presence of wear debris particles inside the groove in the longitudinal direction (Figures 3a and 3b). There is less damage on the surface of the composite as compared to neat PC. Apparently nanoclay helps to dissipate the stress during contact with the indenter.

Results of computer simulation of scratch testing using the molecular dynamics method [8] have been reported. However, results so far available pertain to neat polymers only.

4.2. Sliding wear

We have previously reported [17, 26] that glassy polystyrene (PS) is an exception among all polymers investigated in sliding wear mode. Namely, PS does not show a horizontal asymptote in residual depth values as a function of the number of scratches. In other words, in the case of PS, there is no strain hardening in multiple sliding along the same groove. This finding has led us to the definition of brittleness [27, 28].

However, as we have shown earlier [15], addition of 1 wt% of a liquid-crystalline additive induced the strain hardening effect in PS. This has led us to the idea to determine the sliding wear resistance of

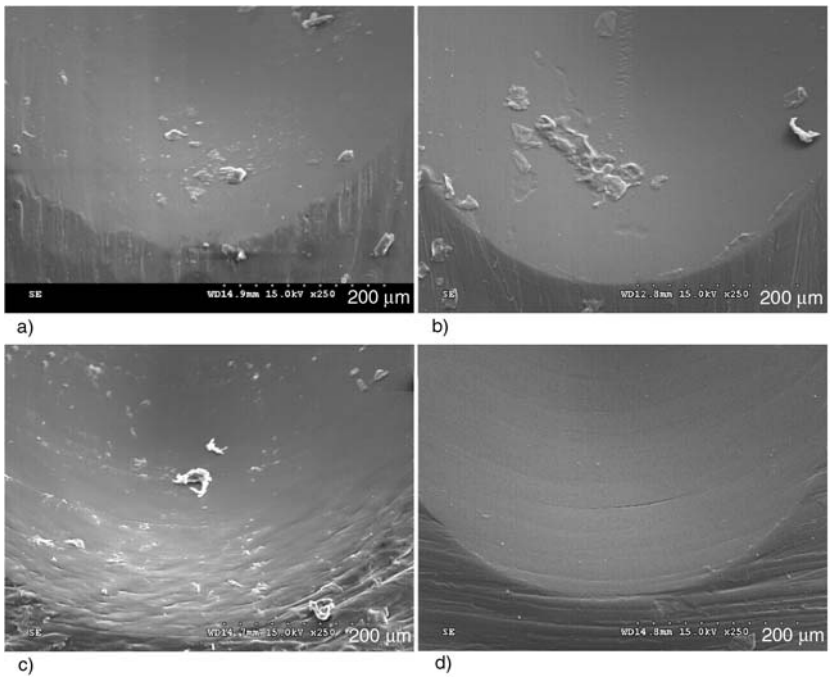

Figure 3. SEM micrographs after progressive load testing: a) PC in the longitudinal direction; b) composite in the longitudinal direction; c) PC in the transverse direction and d) composite in the transverse direction

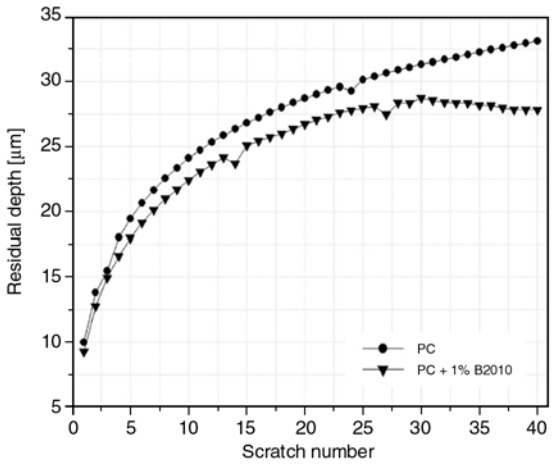

Figure 4. Residual depth under multiscratching for PC and PC + 1% B2010 in the transverse direction

PC (another glassy polymer) and effects of the nanoclay additive.

The tests were performed along the transverse direction with respect to the melt flow, perpendicular to nanoclay orientation (see again Figure 1b) that gave similar results for PC and the nanohybrid under the progressive load testing (Figure 2b).

Figure 4 shows the residual depth values for PC and the nanohybrid after 40 scratches. The higher scratch resistance of the hybrid is evident from the initial scratches and increases as the number of scratches increases. After 22 or so scratches we see a difference between PC and the nanohybrid. We see strain hardening (originally discovered in [16])

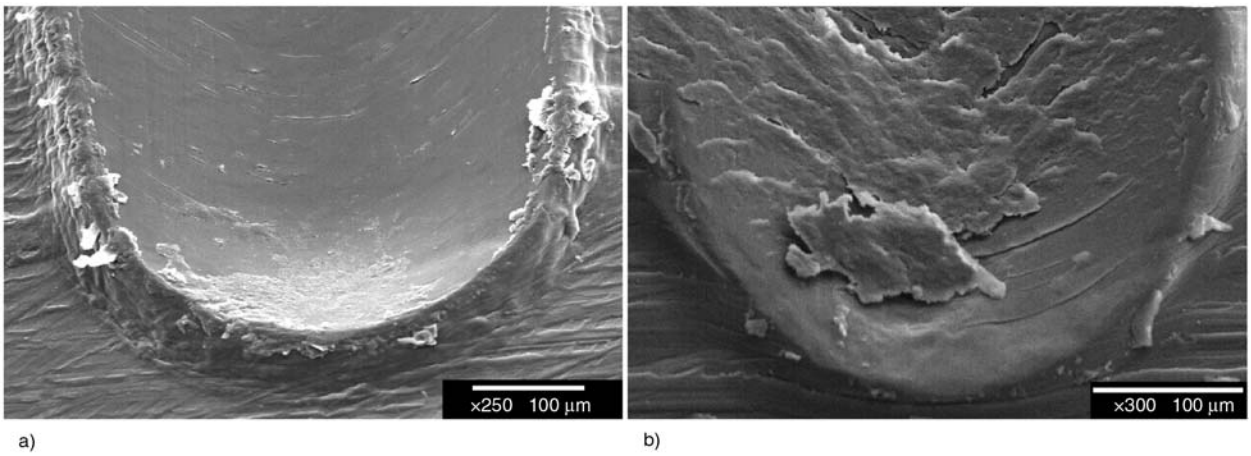

Figure 5. SEM micrographs after 40 scratches of: a) PC; b) PC + 1% B2010

in the hybrid – clearly due to the presence of nanoclay – but not in neat PC.

Scratch grooves of both materials are seen in SEM (Figure 5). PC (Figure 5a) shows a flat and smooth surface, with the presence of periodic cracks perpendicular to the sliding direction, and accumulation of plastically deformed material at the edges of the track. The nanohybrid (Figure 5b) shows a scratch groove covered by a layer of plastically deformed material. The better performance of the nanohybrid can be attributed to the stability of the plastically deformed layer.

Figure 6 displays diagrams of the residual depth R_h under variable load as a function of the scratch number and sliding direction for PC (Figure 6a) and for the nanohybrid (Figure 6b). For PC we see R_h nearly independent of the sliding direction. As anticipated by Figure 4, strain hardening is seen in the nanohybrid.

Under low load of 5.0 N, the sliding wear resistance of the nanohybrid is independent of the scratch direction. Under 10.0 N, a higher resistance in the transverse direction is observed, with a maximum R_h reduction of 26.8% for the transverse direction (T-10N; Figure 6b) with respect to the longitudinal one (L-10N; Figure 6b).

We note that the nanohybrid shows the strain hardening effect (with constant or slightly decreasing R_h values) after 12 scratches, under 15.0 N in the

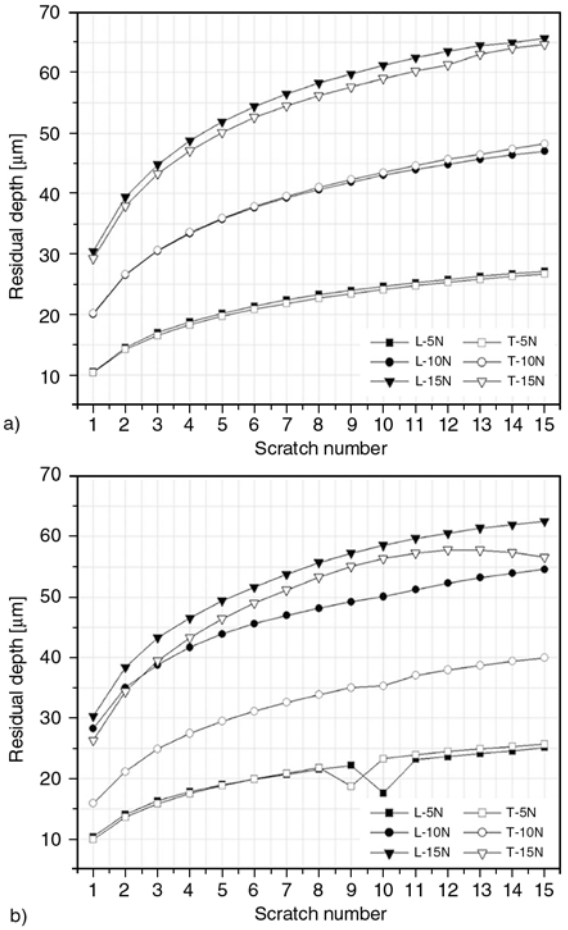

Figure 6. Residual depth under multiscratching as a function of normal load and direction: a) PC; b) nanohybrid

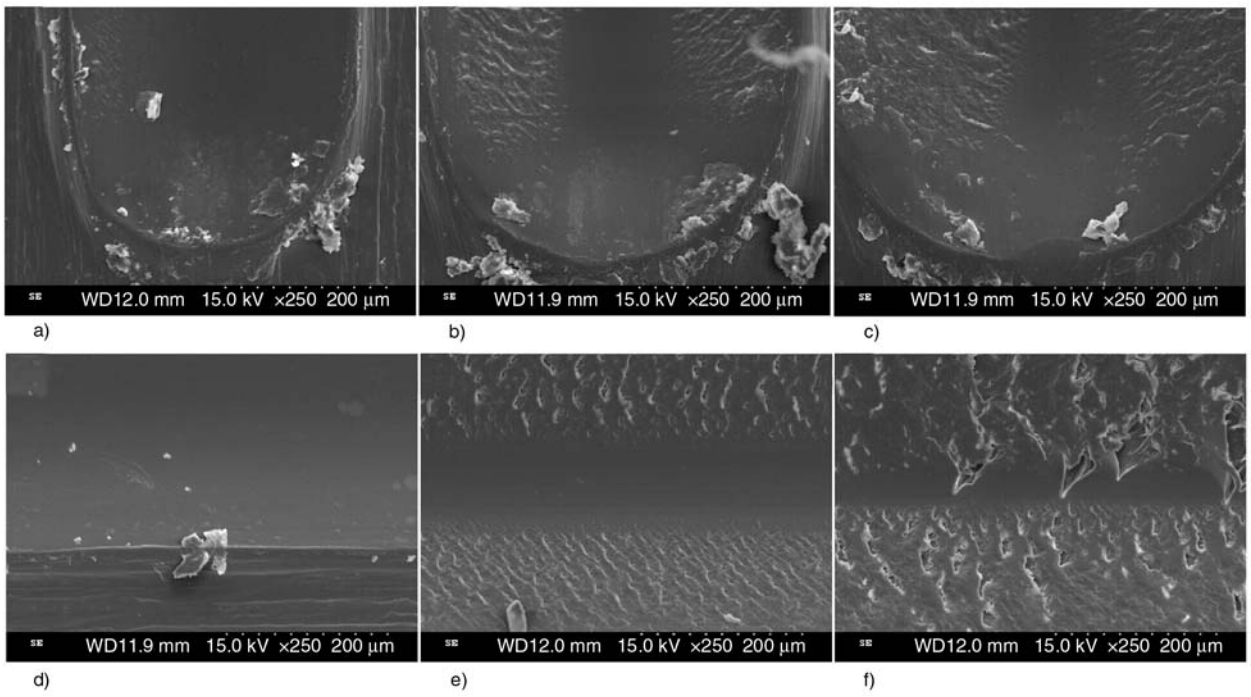

Figure 7. SEM images and magnifications of the nanohybrid scratch grooves in the longitudinal direction: a) and d) 5.0 N; b) and e) 10.0 N; c) and f) 15.0 N

transverse direction (T-15N in Figure 6b). This behavior is similar to that seen after 27 scratches under the normal load of 5.0 N in the transverse direction (Figure 4). It can be concluded that the number of scratches to induce strain hardening decreases as the applied normal load increases.

SEM images in Figure 7 show the severity of the nanohybrid surface damage as a function of the normal load after 15 scratches in the longitudinal direction. Images at the top (a–c) were taken along the scratches, images at the top (d–f) across the scratches. Under 5.0 N (Figures 7a and 7d), a mild plastic deformation and a smooth surface is observed. When the normal load applied is increased to 10.0 N (Figures 7b and 7e) a crazing mechanism with the presence of cracks at the edges of the scar and finally, under 15.0 N, severe plastic deformation and large cracks appear (Figures 7b and 7c).

4.3. Effects of scratch velocity

Variable scratching velocity tests were carried out under the normal load of 5.0 N. Figure 8 shows the change of R_h as a function of scratch number obtained for three velocities on PC (Figure 8a) and the nanohybrid (Figure 8b) in both longitudinal and transverse directions. In the case of PC (Figure 8a), R_h decreases under increasing velocity. A possible explanation is that, at higher velocity, the indenter damages a smaller number of specific locations [26]. Another explanation is that mechanical damage is the main mechanism at low velocities, an effect weakened by thermally induced deformations at high velocities [9, 10]. In this context, heat dissipation at higher velocities necessarily increases free volume v_f. In turn, higher v_f enhances the chain relaxation capability (CRC) and thus viscoelastic recovery [29–31]. Both explanations might be true simultaneously.

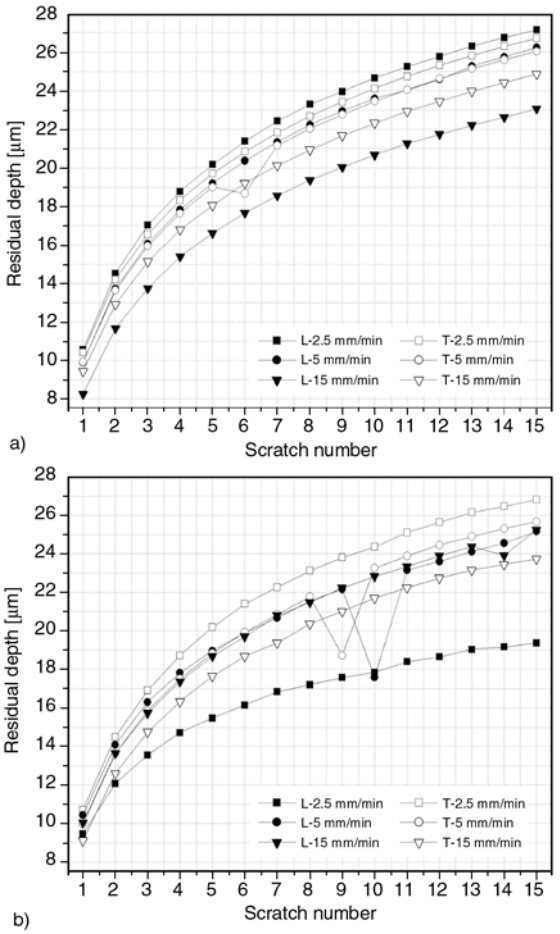

Figure 8. Residual depth in sliding wear determination as a function of scratch velocity and direction: a) PC; b) nanohybrid

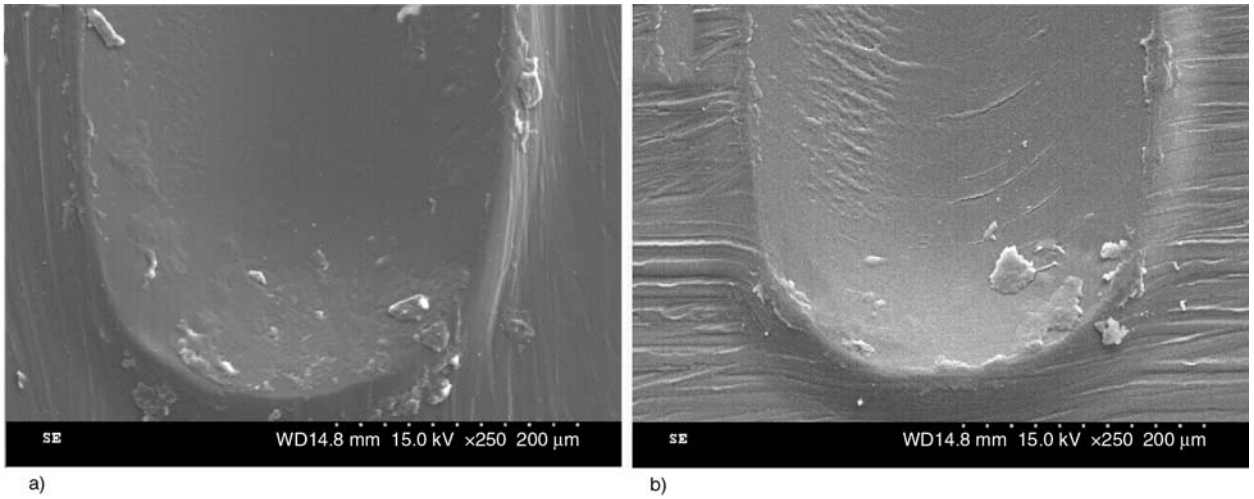

Figure 9. SEM images for the nanohybrid at 2.5 mm/min as a function of the scratch direction: a) longitudinal; b) transverse

The nanohybrid shows an R_h decrease under increasing velocity only in the transverse direction. By contrast, in the longitudinal direction the minimum R_h values are found at the lowest scratch velocity (L-2.5 mm/min; Figure 8b), that is a 27.7% reduction in R_h with respect to the transverse direction (T-2.5 mm/min; Figure 8b). We infer that in the longitudinal direction neither the mechanism of less contacts at higher velocities nor the higher heat dissipation at higher velocities are operative. The maximum R_h reduction of 28.6% is obtained for the nanohybrid with respect to PC at the lowest velocity, L-2.5 mm/minute.

Figure 9 illustrates various wear mechanisms in the nanohybrid. There is a small quantity of debris particles formed in the longitudinal direction (Figure 9a) and crack initiation in the transverse direction (Figure 9b).

A question was asked: are nanocomposites any good for anything? In [13] we have found that pin-on-disk friction of polycarbonate is lowered by addition of the nanoclay. Similar friction lowering was achieved by addition of silica nanoparticles to a commercial epoxy [1]. Carbon nanotubes lower the residual depth of Polyamide 6 in sliding wear determination [32]. Windle and his colleagues report 'a variety of effects' in poly(ether ether ketone) (PEEK) + carbon nanofibers systems, but in particular a reduction of wear rate of PEEK [33]. These results are significant since nanocomposites are mostly made to improve mechanical properties rather than tribological ones. We have already noted in the Introduction that going from a neat polymer to a nanohybrid seems a two-edged sword. Thus, nanofillers in polymers can be useful but there are not panacea.

Acknowledgements

We would like to thank the Ministerio de Ciencia e Innovación, Madrid, and Programa de Generación de Conocimiento Científico de Excelencia de la Fundación Séneca, Agencia de Ciencia y Tecnología de la Región de Murcia (Grant # II PCTRM 2007-10), for financial support of the projects MAT2008-01670/MAT and 08596/PI/08, respectively. Francisco J. Carrión-Vilches is grateful to Fundación Séneca for a grant under the program 'Estancias Externas de Investigadores de la Región de Murcia'. Financial support of this work by the Hispanic and Global Studies Initiatives Fund of the University of North Texas, Denton, and the Robert A. Welch Foundation, Houston (Grant # B-1203) are acknowledged also. Discussions with Dr. Nicholas Randall, CSM Instruments, Needham, MA, are appreciated.

References

[1] Brostow W., Chonkaew W., Datashvili T., Menard K. P.: Tribological properties of epoxy+silica hybrid materials. Journal of Nanoscience and Nanotechnology, **9**, 1916–1922 (2009). DOI: 10.1166/jnn.2009.368

[2] Giraldo L. F., Brostow W., Devaux E., López B. L., Pérez L. D., León D.: Scratch and wear resistance of Polyamide 6 reinforced with multiwall carbon nanotubes. Journal of Nanoscience and Nanotechnology, **8**, 3176–3183 (2008). DOI: 10.1166/jnn.2008.092

[3] Xu D., Karger-Kocsis J., Schlarb A. K.: Rolling friction and wear of organoclay-modified thermoplastic polyurethane rubbers against steel. Kautschuk, Gummi, Kunststoffe, **61**, 98–106 (2008).

[4] Steijn R. P.: Friction and wear in: 'Failure of plastics' (eds.: Brostow W., Corneliussen R. D.) Hanser, New York, 356–392 (1986).

[5] Rabinowicz E.: Friction and wear of materials. Wiley, New York (1995).

[6] Brostow W., Deborde J-L., Jaklewicz M., Olszynski P.: Tribology with emphasis on polymers: Friction, scratch resistance and wear. Journal of Materials Education, **24**, 119–132 (2003).

[7] Myshkin N. K., Petrokovets M. I., Kovalev A. V.: Tribology of polymers: Adhesion friction, wear and mass-transfer. Tribology International, **38**, 910–921 (2005). DOI: 10.1016/j.triboint.2005.07.016

[8] Brostow W., Hinze A. J., Simões R.: Tribological behavior of polymers simulated by molecular dynamics. Journal of Materials Research, **19**, 851–856 (2004). DOI: 10.1557/JMR.2004.0110

[9] Felhős D., Xu D., Schlarb A. K., Váradi K., Goda T.: Viscoelastic characterization of an EPDM rubber and finite element simulation of its dry rolling friction. Express Polymer Letters, **2**, 157–164 (2008). DOI: 10.3144/expresspolymlett.2008.21

[10] Karger-Kocsis J., Felhős D., Bárány T., Czigány T.: Hybrids of HNBR and in situ polymerizable cyclic butylene terephthalate (CBT) oligomers: Properties and dry sliding behaviour. Express Polymer Letters, **2**, 520–527 (2008). DOI: 10.3144/expresspolymlett.2008.62

[11] Karger-Kocsis J., Felhős D., Xu D., Schlarb A. K.: Unlubricated sliding and rolling wear of thermoplastic dynamic vulcanizates (Santoprene) against steel. Wear, **265**, 292–300 (2008). DOI: 10.1016/j.wear.2007.10.010

[12] Khan M. S., Lehmann D., Heinrich G., Gohs U., Franke R.: Structure-property effects on mechanical, friction and wear properties of electron modified PTFE filled EPDM composite. Express Polymer Letters, **3**, 39–48 (2009).
DOI: 10.3144/expresspolymlett.2009.7

[13] Carrión F. J., Arribas A., Bermúdez M-D., Guillamon A.: Physical and tribological properties of a new polycarbonate-organoclay nanocomposite. European Polymer Journal, **44**, 968–977 (2008).
DOI: 10.1016/j.eurpolymj.2008.01.038

[14] Brostow W., Gorman B. P., Olea-Mejia O.: Focused ion beam milling and scanning electron microscopy characterization of polymer+metal hybrids. Materials Letters, **61**, 1333–1336 (2007).
DOI: 10.1016/j.matlet.2006.07.026

[15] Bermúdez M. D., Brostow W., Carrión-Vilches F. J., Cervantes J. J., Pietkiewicz D.: Friction and multiple scratch behavior of polymer+monomer liquid crystals systems. Polymer, **46**, 347–462 (2005).
DOI: 10.1016/j.polymer.2004.11.003

[16] Brostow W., Darmarla G., Howe J., Pietkiewicz D.: Determination of wear of surfaces by scratch testing. e-Polymers, no. 025 (2004).

[17] Bermúdez M-D., Brostow W., Carrión-Vilches F. J., Cervantes J. J., Pietkiewicz D.: Wear of thermoplastics determined by multiple scratching. e-Polymers, no. 001 (2005).

[18] Brocka Z., Schmachtenberg E., Ehrenstein G. W.: Radiation crosslinking engineering thermoplastics for tribological applications. in 'Proceedings of Annual Technical Conference of the Society of Plastics Engineers (SPE ANTEC) Cincinnati, USA' 1690–1694 (2007).

[19] Bismarck A., Brostow W., Chiu R., Hagg Lobland H. E., Ho K. K. C.: Effects of surface plasma treatment on tribology of thermoplastic polymers. Polymer Engineering and Science, **48**, 1971–1976 (2008).
DOI: 10.1002/pen.21103

[20] Brostow W., Buchman A., Buchman E., Olea-Mejia O.: Polymer matrix+metal powder microhybrids. Polymer Engineering and Science, **48**, 1977–1981 (2008).
DOI: 10.1002/pen.21119

[21] Valera-Zaragoza M., Ramírez-Vargas E., Medellín-Rodríguez F. J., Huerta-Martínez B. M.: Thermal stability and flammability properties of heterophasic PP-EP/EVA/organoclay nanocomposites. Polymer Degradation and Stability, **91**, 1319–1325 (2006).
DOI: 10.1016/j.polymdegradstab.2005.08.011

[22] Treloar R. L. G.: The physics of rubber elasticity. Clarendon Press, Oxford (1975).

[23] Yuan M., Song Q., Turng L-S.: Spatial orientation of nanoclay and crystallite in microcellular injection molded polyamide-6 nanocomposites. Polymer Engineering and Science, **47**, 765–779 (2007).
DOI: 10.1002/pen.20752

[24] Yuan M., Turng L. S.: Microstructure and mechanical properties of microcellular injection molded polyamide-6 nanocomposites. Polymer, **47**, 7273–7292 (2005).
DOI: 10.1016/j.polymer.2005.06.054

[25] Wang K., Zhao P., Yang S., Liang S., Zhang Q., Du R., Fu Q., Yu Z., Chen E.: Unique clay orientation in the injection-molded bar of isotactic polypropylene/clay nanocomposite. Polymer, **47**, 7103–7110 (2002).
DOI: 10.1016/j.polymer.2006.08.022

[26] Bermúdez M.-D., Brostow W., Carrión-Vilches F. J., Cervantes J. J., Damarla G., Perez J. M.: Scratch velocity and wear resistance. e-Polymers, no. 003 (2005).

[27] Brostow W., Hagg Lobland H. E., Narkis M.: Sliding wear, viscoelasticity and brittleness of polymers. Journal of Materials Research, **21**, 2422–2428 (2006).
DOI: 10.1557/JMR.2006.0300

[28] Brostow W., Hagg Lobland H. E.: Predicting wear from mechanical properties of thermoplastic polymers. Polymer Engineering and Science, **48**, 1982–1985 (2008).
DOI: 10.1002/pen.21045

[29] Brostow W.: Performance of plastics. Hanser, Munich (2000).

[30] Goldman A. Y.: Viscoelasticity, creep and stress relaxation. in 'Performance of plastics' (ed.: Brostow W.) Hanser, Munich 121–146 (2000).

[31] Brostow W.: Reliability and prediction of long term performance of polymer-based materials. Pure and Applied Chemistry, **81**, 417–432 (2009).
DOI: 10.1351/PAC-CON-08-08-03

[32] Giraldo L. F., López B. L., Brostow W.: Effects of the type of carbon nanotubes on tribological properties of Polyamide 6. Polymer Engineering and Science, **49**, 896–902 (2009).
DOI: 10.1002/pen.21386

[33] Werner P., Alstädt V., Jaskulka R., Jacobs O., Sandler J. K. W., Shaffer M. S. P., Windle A. H.: Tribological behaviour of carbon-nanofibre-reinforced poly(ether ether ketone). Wear, **257**, 1006–1014 (2004).
DOI: 10.1016/j.wear.2004.07.010

eXPRESS Polymer Letters Vol.3, No.10 (2009) 630–638
Available online at www.expresspolymlett.com
DOI: 10.3144/expresspolymlett.2009.79

Taguchi analysis of shrinkage and warpage of injection-moulded polypropylene/multiwall carbon nanotubes nanocomposites

K. Prashantha[1,2,], J. Soulestin[1,2], M. F. Lacrampe[1,2], E. Lafranche[1,2], P. Krawczak[1,2], G. Dupin[3], M. Claes[3]*

[1]Université Lille Nord de France, 59000, Lille, France
[2]Ecole des Mines de Douai , Department of Polymers and Composites Technology & Mechanical Engineering, 941 Rue Charles Bourseul, BP 10838, 59508 Douai, France
[3]Nanocyl SA, Rue de l'Essor, 4, B-5060, Sambreville, Belgium

Received 25 May 2009; accepted in revised form 26 July 2009

Abstract. This paper focuses on the effect of multi-walled carbon nanotube (MWNT) addition on shrinkage and warpage properties of polypropylene (PP) injection mouldings before and after annealing. A Taguchi design of experiments has been implemented to highlight the influence and optimise processing conditions such as injection flow rate, holding pressure, back pressure and screw speed. The addition of 2 wt% of carbon nanotubes into PP significantly reduces the shrinkage and warpage of injection-moulded parts as compared to the neat PP. Skrinkage reduction up to 48% (respectively 33%) is noticed in the flow direction before (respectively after) annealing, whereas warpage reduction exceeds 55%. The sensitivity of the injection-mouldings dimensional properties to processing parameters remains roughly the same in case of neat PP and PP/MWNT nanocomposites when shrinkage is considered. It is even significantly reduced by carbon nanotubes addition when warpage is considered. Furthermore, the Taguchi method provides an efficient and effective tool to study the effects of process parameters on the warpage and shrinkage of injection moulded parts. The additive model used works well for predicting the warpage and shrinkage behaviour of PP and PP/MWNT composites.

Keywords: *nanocomposites, polypropylene, multi-walled carbon nanotubes, Taguchi analysis, shrinkage*

1. Introduction

Carbon nanotubes (CNT) are promising fillers for polymer materials due to their outstanding mechanical, electrical, and thermal properties [1–4]. These new nanocomposite materials find industrial application in the field of electrostatic dissipation [5], electromagnetic interference- shielding (associated with both commodity polymers [6] and engineering polymers [7]), and electrically conductive materials achieving at the same time enhanced stiffness, strength, impact properties, thermal stability, tribological properties, and reduced thermal expansion [8]. Further, the manufacturing of industrial parts from CNT/polymer nanocomposites requires the development of processing technologies, which are preferably compatible to already existing industrial moulding technologies. Moreover, a good knowledge of the relationship between processing conditions and properties of the nanocomposites is crucial. Most of the reported literature on nanotubes filled polymers has focussed on the quantitative [9] or qualitative [10] description of the dispersion state of nanotubes, the improvement of nanotube dispersion by polymer [11] or nanotubes

*Corresponding author, e-mail: prashantha@ensm-douai.fr

[12] modifications and/or proper selection of processing parameters (e.g. extrusion rotation speed and screw design [13], shear stress [14]), also on structure [15], viscoelastic (both in solid [16] and molten [17] state), electrical (conductivity [18], resistivity [19], percolation threshold [20]), mechanical (at room [21] and high [22] temperature) or interfacial [23] properties, as well as gas permeability and thermal stability [24] of the CNT filled polymers nanocomposites.

However, industrial parts specifications and requirements are not limited to the above mentioned usage properties. The dimensional accuracy and stability of the parts are often important quality and functional criteria (especially when parts are assembled to build more complex structures). Nevertheless, systematic investigations on the influence of nanofiller addition and of process conditions on dimensional properties of polymer nanocomposites and their variation as a function of time have not been addressed in the literature up to now. Salahuddin and Shehata [25] have studied the very particular case of polymerisation shrinkage and warpage of heat-cured dental acrylic resin. These authors have shown that addition of nanoclay reduces dimensional and shape variations, but without having investigated the effect of processing parameters modifications.

Injection moulding is one of the most important polymer processing methods for manufacturing of plastic parts. The plastic part obtained by injection moulding process is approximately the shape of the mould and may not involve further operation. The final dimensions and geometry of the moulded part is usually a primary concern in terms of manufacturing quality. Because of some physical aspect of the process, significant deviations are observed between the dimensions and shape of the cavity and those of the final parts. Those discrepancies are caused by thermal effects such as difference between the linear thermal expansion coefficients of the mould and the polymer [26], crystallization and thermal kinetics [27], flow effects inducing filler [28] and molecular orientation gradients [29, 30], as well as mould deformations [31]. Practically, the deviations from the mould geometry may be described by shrinkage and warpage, shrinkage regarding dimensional differences and warpage regarding shape differences [32]. To evaluate and improve achievable tolerances of injection moulded parts, the effects of the outlined phenomena have to be quantitatively assessed. Therefore, it is of critical importance to effectively control the factors (e.g. temperature [30], mould geometry [33], holding pressure and injection velocity [34], holding pressure and packing time [35]), which influence the moulding process from this standpoint.

Also, it is known that the annealing of thermoplastics after the manufacturing causes changes in the structure and properties of the materials. This process has been employed to improve the final properties of the polymers via healing of defects and diminishing residual stress and strain. In addition, lamellae thickening and rearrangement of the chain during heating may also occur upon annealing [36]. Therefore, it would be worth considering also the effect of annealing on the dimensional properties of the nanocomposites parts.

Since a large number of parameters influences injection-moulding processes, a full-factorial experiment is required to determine the important factors and optimal process conditions. This is both costly and time consuming. Therefore, design of experiments (DOE) is usually adopted to schedule the injection experiment [37, 38]. DOE commonly uses the method invented by Taguchi [39].

In that context, this paper proposes an expansion of our previous research on nanotube filled polypropylene nanocomposites [11, 16]. It aims at systematically investigating the effects of nanofiller addition and variation in process conditions such as holding pressure, back pressure, injection flow rate, and screw rotation speed, on the shrinkage (along- and across-the-flow directions) and warpage of injection-moulded PP/MWNT nanocomposite in U box shaped parts on the basis of a Taguchi DOE. This work therefore constitutes a first step of the future development of guidelines for plastics converters.

2. Materials and methods

2.1. Materials

Polypropylene (PP) – multi wall carbon nanotubes (MWNT) nanocomposites were produced by mixing in a co-rotating twin screw extruder (Clextral, Firminy, France) at a barrel temperature of 195–210°C and a screw speed of 50 rpm homo PP granules (Polychim polypropylene with a melt flow index of 12 g/10 min at 190°C, Polychim Industrie, Loon-Plage, France) with a commercial master-

batch containing 20 wt% of MWNT compounded by extrusion process (Plasticyl-2001 supplied by Nanocyl, Sambreville, Belgium). The specifications of MWNTs in the masterbatch are as follows: average diameter is 10 nm, average length of the nanotubes is 1.5 μm, and purity > 90%. During melt extrusion ventilation was kept on to remove trapped air in the compounds. After pelletizing, the nanocomposite granules were dried in a vacuum oven at 120°C for at least 4 h before injection-moulding. Previous studies from our laboratory indicated that incorporation of 2 wt% of MWNTs in PP gives better mechanical properties [16]. Therefore, 2 wt% of MWNTs filled PP nanocomposites have been chosen for the present study.

2.2. Injection moulding conditions

The injection moulding machine used had a clamping force of 800 kN (Krauss Maffei, Munich, Germany) and was equipped with a specially designed 'U' box type mould. The injection-moulded plastic part manufactured had a 2 mm uniform thickness and its 'U' shape roughly reproduces the geometry of many industrial parts (boxes, bumper, dash board insert, etc.). The mould cavity was fed by a sprue gate as show in Figure 1. The cavity was equipped with a melt pressure sensor that was used to control the process repeatability.

The investigations carried out mainly aimed at determining the influence of the chosen input parameters (injection moulding conditions) on the output quantities (such as shrinkage and warpage), and further using experimental techniques and statistical methods for the data analysis, to establish the relationship between them in the form of a function. Taguchi design of experiments (DOE) have been used for this purpose. The experiments consist

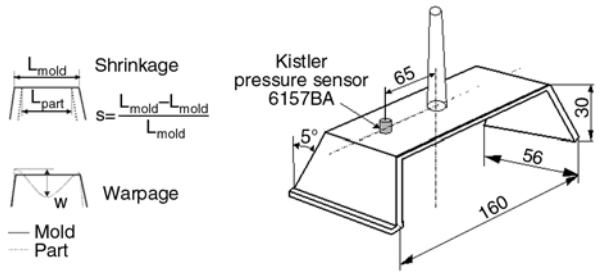

Figure 1. Typical part manufactured by injection moulding

Table 1. Factors and levels selected in the DOE

Factors	Level 1 (low)	Level 2 (high)
Injection speed [cm^3/s]: *Q*	25	50
Holding pressure [bar]: hP	250	350
Back pressure [bar]: bP	35	65
Screw rotational speed [rpm]: Ω	50	90

Table 2. L16 (24)orthogonal array used for the DOE

Trial No	Q	hP	bP	Ω
1	1	1	1	1
2	1	1	2	2
3	1	2	1	2
4	1	2	2	1
5	2	1	1	2
6	2	1	2	1
7	2	2	1	1
8	2	2	2	2
9	1	1	1	2
10	1	1	2	1
11	1	2	1	1
12	1	2	2	2
13	2	1	1	1
14	2	1	2	2
15	2	2	1	2
16	2	2	2	1

of two identical L16 orthogonal array fractional factorials designs, the first one with the neat PP and the other with the PP/MWNT nanocomposite. Four processing parameters, which were expected to be significant in their effects on the induced microstructure and the properties of the injection-moulded parts were selected as variables in these DOE: injection speed or volume flow rate (*Q*), holding pressure (hP), back pressure (bP) and screw rotational speed Because thermal parameters have a very high effect on part stability [40], taking into account melt and mould temperatures in the experimental design would not have permitted to investigate with a sufficient accuracy the influences of the four other processing parameters. Each studied parameter was set up at two levels (low and high) according to the experimental matrix shown in Table 1. The other processing parameters were kept constant: mould temperature was kept at 35°C and polymer melt temperature at 210°C; cooling time was maintained at 25 seconds, and a holding time of 35 sec was fixed. The L16 fractional orthogonal design array and the levels of set-up conditions are reported in Table 2.

2.3. Shrinkage and warpage measurements

During the injection moulding experiments, each process condition was allowed to stabilize for at least half an hour. After that, ten parts were moulded at each process condition. The sixth to tenth injection-moulded parts were further characterized. Shrinkage and warpage were measured one week after moulding and conditioning at 23°C and 50% HR so as to stabilise the material.

Annealing of the injection-moulded parts was carried out at a temperature of 120°C during 5 hours, followed by a cooling at 23°C and 50% relative humidity (henceforth this condition will be referred as annealed one) so as to allow residual stresses relaxation without inducing structural change in polypropylene [36].

The shrinkage and warpage of the injection-moulded parts are defined in Figure 1. Mould shrinkage S was measured as per the ISO-294-4 standard. S is the relative difference between the dimensions of the part and the dimensions of the mould. It is expressed as a percent change in dimension of a specimen in relation to mould dimensions. The same procedure is used for annealed samples. Generally, shrinkage of many materials differs for flow (S_F) and transverse (S_T) (or across flow) directions. Flow direction is taken as the direction the molten material is travelling when it exits the gate and enters the mould.

Mould shrinkage in the flow direction is calculated by Equation (1):

$$S_F = 100 \cdot \frac{L_M - L_P}{L_M} \tag{1}$$

where L_M is the length of the mould cavity and L_P is the corresponding length of the part after it has cooled.

Mould shrinkage in the transverse direction is calculated by Equation (2):

$$S_T = 100 \cdot \frac{W_M - W_P}{W_M} \tag{2}$$

where W_M is the width of the mould cavity and W_P is the corresponding width of the part after it has cooled.

Warpage measurements were carried out by using a Cyclone 3D measurement machine. The values of warpage are measured as the displacement difference between upper and lower points on the injection moulded part surface at ten different longitudinal lines as shown in Figure 2.

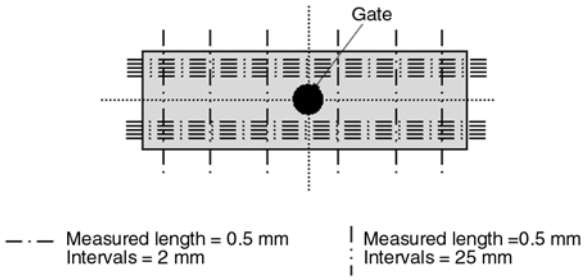

Figure 2. Warpage measurement spots of injection-moulded parts

3. Results and discussion

3.1. Shrinkage

The mean values of shrinkage in both flow and transverse directions of all samples from the 16 runs for PP and PP/MWNT nanocomposites were measured before annealing (Figures 3a and 4a) and after annealing (Figures 3b and 4b). Whatever the material may be (neat PP or PP/MWNT nanocomposite), it undergoes logically on the average between 2 and 4 times more shrinkage in transverse direction than along the flow direction. This may be explained by the combined effect of crystallization and flow-induced molecular and/or filler orientations, which is in accordance with the literature [34].

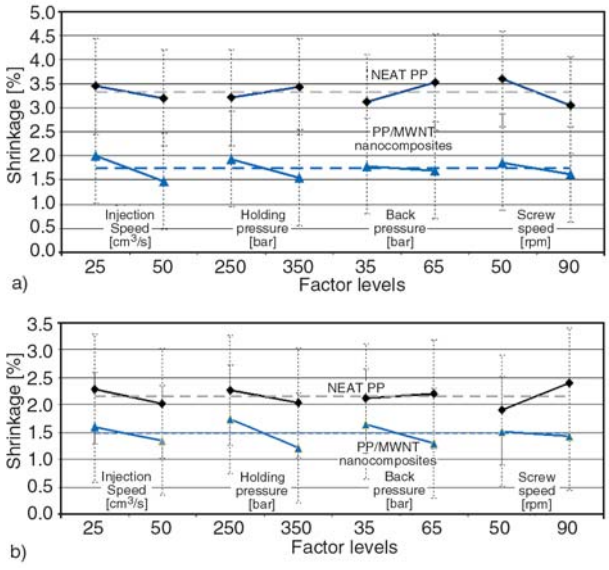

Figure 3. Shrinkage of PP and PP/MWNT nanocomposites in flow direction before annealing (a) and after annealing (b) – Standard deviations represent data scattering when the considered factor is set up to its low or high level in the Taguchi DOE

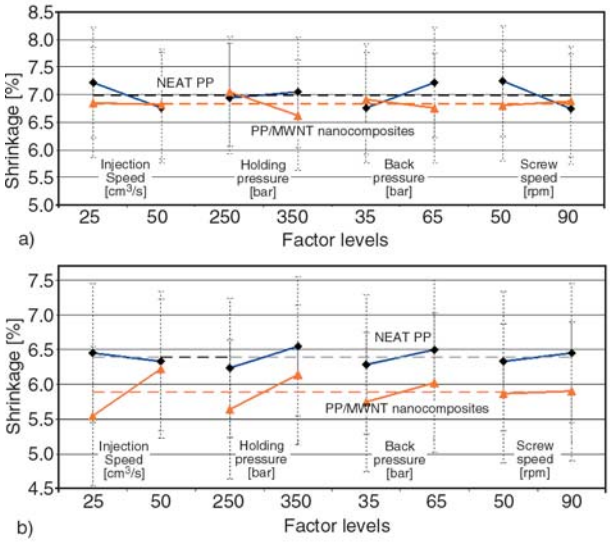

Figure 4. Shrinkage of PP and PP/MWNT nanocomposites in transverse direction before annealing (a) and after annealing (b) – Standard deviations represent data scattering when the considered factor is set up to its low or high level in the Taguchi DOE

The addition of 2 wt% of MWNTs into PP matrix allows reducing significantly the moulding shrinkage of injection moulded-parts. Compared to neat PP, this reduction reaches 48% on the average before annealing and 33% after annealing in the flow direction. The carbon nature of the nanofiller used highly limits its sensitivity to thermal expansion in the temperature range considered during injection moulding. Carbon nanotubes are not subjected to shrinkage and therefore limit the nanocomposite shrinkage accordingly. The shrinkage reduction effect induced by addition of carbon nanotubes is slightly less after annealing. This may be mainly ascribed to the completion of the relaxation mechanisms undergone by the neat PP after annealing.

The effect of 2 wt% of MWNTs addition into PP is much lower in the transverse direction even if still significant, as the shrinkage reduction is limited to about 5% before annealing and about 10% after annealing.

The influence of the processing parameters (injection speed, holding pressure, back pressure and screw rotation speed) are much more difficult to handle. Actually, the investigated processing parameters sometimes induce a quite low variation in the measured dimensional property. Therefore it makes no sense to discuss the dependence of the shrinkage on each moulding parameter in that case. It is however worth noting that the sensitivity of the injection-mouldings shrinkage to significant processing parameters globally remains roughly the same (variation of output parameters with similar orders of magnitude) for neat PP and PP/MWNT nanocomposites (except in one case, e.g. effect of injection speed on the transverse shrinkage after annealing; the reason for this exception has not been elucidated).

3.2. Warpage

Apart from shrinkage, warpage behaviour of injection-moulded parts is crucial in determining the polymer dimensional accuracy and subsequent application. Warpage behaviour of PP and PP/MWNT materials is shown in Figure 5. Nanotubes addition in PP clearly reduces average warpage by more than 55% both before and after annealing.

Warpage is known to be related to the existence of residual stresses related to heterogeneous temperature and cooling rate distributions, non-symmetric processing-induced morphology and orientation patterns through the part thickness. Under the same set of processing conditions in a Taguchi DOE, Fourdin *et al.* [41] have shown that nanofillers tend to make the injection-moulded parts morphology much more homogeneous, the nucleation being favoured instead of crystal growth during the crystallisation process. This reduced material heterogeneity then limits the local differential shrinkage

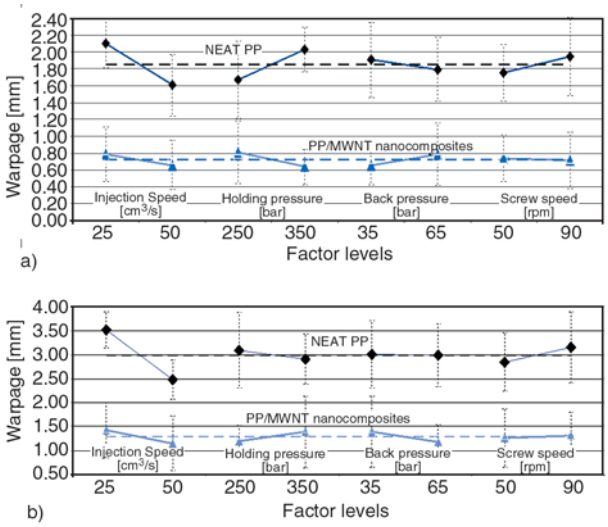

Figure 5. Warpage of PP and PP/MWNT nanocomposites before annealing (a) and after annealing (b) – Standard deviations represent data scattering when the considered factor is set up to its low or high level in the Taguchi DOE

and therefore the parts warpage. Another reason for the warpage reduction noticed upon carbon nanotubes addition may also be that the higher the rigidity of the material is, the less the part is able to deform (addition of 2 wt% of carbon nanotubes into PP increases its modulus by 35% as reported in our previous paper [16]).

Moreover, the warpage in PP/MWNT sample is less sensitive to the variation of the moulding parameters when compared to PP parts, where injection speed (primarily) and holding pressure (in a lesser extent) appear to affect significantly the part warpage. This suggest that the geometrical shape of nanocomposite injection-moulded part is less sensitive to fluctuation of processing parameters than neat PP ones. The use of nanocomposites therefore improves the robustness of the injection moulding process.

3.3. Verification tests

Additive model is being used in Taguchi method in order to predict the influence of the control factors on the response [39]. The model refers to the sum of the individual factor effects with cross-terms (interactions). One major purpose of the verification experiment is to provide evidence that shows the additive equation applies and that interactions are low. The applicability of the additive model cannot be shown simply from the factor effects plots. The general form of the predictive equation is given by Equation (3):

$$Y_{pred} = Y_{expt} + a(Q) + b(\mathrm{hP}) + c(\mathrm{bP}) + d(\Omega) + e(Q-\mathrm{hP}) + f(\mathrm{bP}-\Omega) \quad (3)$$

where Y_{pred} is the predicted value, and Y_{expt} the overall average response for the orthogonal array. Factors a, b, c and d are coefficients (low level for optimal combination or high level for minimal combination) of corresponding parameters. 'e' and 'f' are the coefficients of interaction parameters for 'Q–hP' and 'bP–Ω' respectively. All these values are obtained by analysis of variance and are tabulated in Table 3.

The factor effects corresponding to the factor levels being modelled (typically the optimum levels) are used in the predictive equation. Since the quality of warpage and shrinkage is the type of 'Smaller the Better', the optimal combination of studied factors for the smallest warpage and shrinkage can be identified from the response plots.

Table 4 summarizes the optimal factor combinations for the PP and PP/MWNT materials. The predicted optimal warpage and shrinkage (along flow and across flow direction) of each case is obtained by substituting the corresponding factors' effects shown in the response plots into the predictive equation. In practice it is very difficult to state with precision how close the experimental numbers must come to the predicted values for the agreement to be considered good. This model holds good only for this present set of parameters, but it validates the previous statistical analysis. As shown in Table 4, all the predicted values fall within the range of standard deviation of experimental means, except for the predicted value for PP/MWNT warpage before annealing.

4. Conclusions

The addition of 2 wt% of carbon nanotubes into PP significantly reduces the shrinkage and warpage of injection-moulded parts as compared to the neat PP, both before and after annealing. Skrinkage reduction up to 48% (resp. 33%) were noticed in the flow direction before (resp. after) annealing, whereas warpage reduction was found to exceed 55%. The extent of anisotropic shrinkage across-

Table 3. Model coefficient values calculated from variance analysis

Dimensional properties		Warpage				Shrinkage							
		Before annealing		After annealing		Flow direction				Transverse direction			
						Before annealing		After annealing		Before annealing		After annealing	
Material		PP	PP-MWNT	PP	PP-MWNT	PP	PP-MWNT	PP	PP-MWNT	PP	PP-MWNT	PP	PP-MWNT
Model coefficients	a	–0.2465	–0.0645	–0.5250	–0.1362	–0.1240	–0.2644	–0.2306	–0.1198	0.2307	–0.0146	–0.0609	–0.3403
	b	–0.2781	–0.0851	–0.0900	–0.0969	–0.1170	–0.1903	–0.2159	–0.2622	–0.0535	–0.2141	–0.1546	–0.2487
	c	–0.0561	–0.0635	0.0069	–0.1046	–0.2049	–0.0418	0.0413	–0.1747	–0.2269	–0.0778	–0.1103	–0.1340
	d	–0.0966	–0.0138	–0.1583	–0.0282	–0.2749	–0.1229	–0.2612	–0.0358	–0.2517	–0.0363	–0.0603	–0.0166
	e	–0.0813	–0.0022	–0.1585	–0.0783	–0.1748	0.0042	–0.1999	–0.0412	–0.1981	–0.0971	–0.1193	–0.3660
	f	–0.0074	–0.1168	–0.0411	–0.1102	–0.3068	–0.0890	–0.1233	–0.1425	–0.1891	–0.0499	–0.2448	–0.1388

Table 4. Verification conditions, predicted values and experimental values

Dimensional properties		Warpage				Shrinkage							
		Before annealing		After annealing		Flow direction				Transverse direction			
						Before annealing		After annealing		Before annealing		After annealing	
Material		PP	PP-MWNT	PP	PP-MWNT	PP	PP-MWNT	PP	PP-MWNT	PP	PP-MWNT	PP	PP-MWNT
Processing parameters (Optimal combination)	Injection speed [cm^3/s]	50	50	50	50	25	50	50	50	50	50	50	25
	Holding pressure [bar]	250	350	250	250	350	350	350	350	350	350	250	250
	Back pressure [bar]	35	35	35	65	35	35	35	65	35	35	65	65
	Screw rotational speed [rpm]	50	90	50	50	90	50	90	50	50	50	50	90
Predicted values for warpage [mm] and shrinkage [%]		1.807	0.379	2.238	0.733	2.126	1.104	1.164	0.697	6.303	6.346	5.643	4.643
Experimental values for warpage [mm] and shrinkage [%]		1.064 ±0.018	0.342 ±0.027	2.108 ±0.082	0.702 ±0.007	2.285 ±0.028	1.002 ±0.071	1.165 ±0.052	0.665 ±0.034	6.152 ±0.020	6.375 ±0.146	5.831 ±0.035	4.142 ±0.011

the-flow direction is logically more than the shrinkage along-the-flow direction. The sensitivity of the injection-mouldings dimensional properties to investigated processing parameters remains roughly the same in case of neat PP and PP/MWNT nanocomposites when shrinkage is considered. It is even significantly reduced by carbon nanotubes addition when warpage is considered.

Furthermore, the Taguchi method provides an efficient and effective tool to study the effects of process parameters on the warpage and shrinkage of injection moulded parts. The additive model works well for predicting the warpage and shrinkage behaviour of PP and PP/MWNT composites.

References

[1] Du J-H., Bai J., Cheng H-M.: The present status and key problems of carbon nanotube based polymer composites. Express Polymer Letters, **1**, 253–273 (2007). DOI: 10.3144/expresspolymlett.2007.39

[2] Coleman J. N., Khan U., Gun'ko Y. K.: Mechanical reinforcement of polymers using carbon nanotubes. Advanced Materials, **18**, 689–706 (2006). DOI: 10.1002/adma.200501851

[3] Moniruzzaman M., Winey K. I.: Polymer nanocomposites containing carbon nanotubes. Macromolecules, **39**, 5194–5205 (2006). DOI: 10.1021/ma060733p

[4] Prashantha K., Soulestin J., Lacrampe M-F., Krawczak P.: Present status and key challenges of carbon nanotubes reinforced polyolefins: A review on nanocomposites manufacturing and performance issues. Polymers and Polymer Composites, **17**, 205–245 (2009).

[5] Ferguson D. W., Bryant E. W. S., Fowler H. C.: ESD thermoplastic product offers advantages for demanding electronic applications. in 'ANTEC'98 Proceedings, Atlanta, USA' 1219–1222 (1998).

[6] Ma C-C. M., Huang Y-L., Kuan H-C., Chiu Y-S.: Preparation and electromagnetic interference shielding characteristics of novel carbon-nanotube/siloxane/poly-(urea urethane) nanocomposites. Journal of Polymer Science Part B: Polymer Physics, **43**, 345–358 (2005). DOI: 10.1002/polb.20330

[7] Yang Y. L., Gupta M. C., Dudley K. L., Lawrence R. W.: A comparative study of EMI shielding properties of carbon nanofiber and multi-walled carbon nanotube filled polymer composites. Journal of Nanoscience and Nanotechnology, **5**, 927–931 (2005). DOI: 10.1166/jnn.2005.115

[8] Breuer O., Sundararaj U.: Big returns from small fibers: A review of polymer/carbon nanotube composites. Polymer Composites, **25**, 630–645 (2004). DOI: 10.1002/pc.20058

[9] Luo Z. P., Koo J. H.: Quantitative study of the dispersion degree in carbon nanotube/polymer nanocomposites. Materials Letters, **62**, 3493–3496 (2008). DOI: 10.1016/j.matlet.2008.03.010

[10] Park S-D., Han D-H., Teng D., Kwon Y.: Rheological properties and dispersion of multi-walled carbon nanotube (MWCNT) in polystyrene matrix. Current Applied Physics, **8**, 482–485 (2008).
DOI: 10.1016/j.cap.2007.10.062

[11] Prashantha K., Soulestin J., Lacrampe M. F., Claes M., Dupin G., Krawczak P.: Multi-walled carbon nanotube filled polypropylene nanocomposites based on masterbatch route: Improvement of dispersion and mechanical properties through PP-g-MA addition. Express Polymer Letters, **2**, 735–745 (2008).
DOI: 10.3144/expresspolymlett.2008.87

[12] Jin S-H., Park Y-B., Yoon K. H.: Rheological and mechanical properties of surface modified multi-walled carbon nanotube-filled PET composite. Composites Science and Technology, **67**, 3434–3441 (2007).
DOI: 10.1016/j.compscitech.2007.03.013

[13] Villmow T., Pötschke P., Pegel S., Häussler L., Kretzschmar B.: Influence of twin-screw extrusion conditions on the dispersion of multi-walled carbon nanotubes in a poly(lactic acid) matrix. Polymer, **49**, 3500–3509 (2008).
DOI: 10.1016/j.polymer.2008.06.010

[14] Li Y., Shimizu H.: High-shear processing induced homogenous dispersion of pristine multiwalled carbon nanotubes in a thermoplastic elastomer. Polymer, **48**, 2203–2207 (2007).
DOI: 10.1016/j.polymer.2007.02.066

[15] Xu D., Wang Z.: Role of multi-wall carbon nanotube network in composites to crystallization of isotactic polypropylene matrix. Polymer, **49**, 330–338 (2008).
DOI: 10.1016/j.polymer.2007.11.041

[16] Prashantha K., Soulestin J., Lacrampe M. F., Dupin G., Krawczak P., Claes M.: Masterbatch-based multi-walled carbon nanotube filled polypropylene nanocomposites: Assessment of rheological and mechanical properties. Composites Science and Technology, **69**, 1756–1763 (2009).
DOI: 10.1016/j.compscitech.2008.10.005

[17] Wang M., Wang W., Liu T., Zhang W-D.: Melt rheological properties of nylon 6/multi-walled carbon nanotube composites. Composites Science and Technology, **68**, 2498–2502 (2008).
DOI: 10.1016/j.compscitech.2008.05.002

[18] Valentino O., Sarno M., Rainone N. G., Nobile N. R., Ciambelli P., Neitzert H. C., Simon G. P.: Influence of the polymer structure and nanotube concentration on the conductivity and rheological properties of polyethylene/CNT composites. Physica E: Low-dimensional Systems and Nanostructures, **40**, 2440–2445 (2008).
DOI: 10.1016/j.physe.2008.02.001

[19] Bao H-D., Guo Z-X., Jian Y.: Effect of electrically inert particulate filler on electrical resistivity of polymer/multi-walled carbon nanotube composites. Polymer, **49**, 3826–3831 (2008).
DOI: 10.1016/j.polymer.2008.06.024

[20] Bauhofer W., Kovács J. Z.: A review and analysis of electrical percolation in carbon nanotube polymer composites. Composites Science and Technology, **69**, 1486–1498 (2009).
DOI: 10.1016/j.compscitech.2008.06.018

[21] Yang B-X., Shi J-H., Pramoda K. P., Goh S. H.: Enhancement of the mechanical properties of polypropylene using polypropylene-grafted multiwalled carbon nanotubes. Composites Science and Technology, **68**, 2490–2497 (2008).
DOI: 10.1016/j.compscitech.2008.05.001

[22] Bao S. P., Tjong S. C.: Mechanical behaviors of polypropylene/carbon nanotube nanocomposites: The effects of loading rate and temperature. Material Science and Engineering: Part A, **485**, 508–516 (2008).
DOI: 10.1016/j.msea.2007.08.050

[23] Zhao B., Wang J., Li Z., Liu P., Chen D., Zhang Y.: Mechanical strength improvement of polypropylene threads modified by PVA/CNT composite coatings. Materials Letters, **62**, 4380–4382 (2008).
DOI: 10.1016/j.mat.let.2008.07.037

[24] Bikiaris D., Vassiliou A., Chrissafis K., Paraskevopoulos K. M., Jannakoudakis A., Docoslis A.: Effect of acid treated multi-walled carbon nanotubes on the mechanical, permeability, thermal properties and thermo-oxidative stability of isotactic polypropylene. Polymer Degradation and Stability, **93**, 952–967 (2008).
DOI: 10.1016/j.polymdegradstab.2008.01.033

[25] Salahuddin N., Shehata M.: Polymethylmethacrylate-montmorillonite composites: Preparation, characterization and properties. Polymer, **42**, 8379–8385 (2001).
DOI: 10.1016/S0032-3861(01)00253-1

[26] Jansen K. L. B., Van Dijk D. J., Husselman M. H.: Effect of processing conditions on shrinkage in injection moulding. Polymer Engineering and Science, **38**, 838–846 (1998).
DOI: 10.1002/pen.10249

[27] Regnier G., Trotignon J. P.: Local orthotropic shrinkage determination in injected moulded polymer plates. Polymer Testing, **12**, 383–392 (1993).

[28] Michil T., Seto M., Yamabe M., Kubota Y., Aoki G., Ohisuka H.: Study of warpage behavior and filler orientation during injection molding. International Polymer Processing, **23**, 419–429 (2008).
DOI: 10.3139/217.0064

[29] Schift H., David C., Gobrecht J., D'Amore A., Simoneta D., Kaiser W., Gabriel M.: Quantitative analysis of the molding of nanostructures. Journal of Vacuum Science and Technology: Part B, **18**, 3564–3568 (2000).
DOI: 10.1116/1.1324622

[30] Lafranche E., Pabiot J.: Effect of thermal dissymetries on morphology and internal stresses of injection-molded polypropylene parts: Influence on the deformation. Journal of Injection Molding Technology, **4**, 51–64 (2000).

[31] Liao S. J., Chang D. Y., Chen H. J., Tsou L. S., Ho J. R., Yau H. T., Hsieh W. H., Wang J. T., Su Y. C.: Optimal process conditions of shrinkage and warpage of thin-wall parts. Polymer Engineering and Science, **44**, 917–928 (2004).
DOI: 10.1002/pen.20083

[32] Kovács J. G., Bercsey T.: Influence of mold properties on the quality of injection molded parts. Periodica Polytechnica-Mechanical Engineering Series, **49**, 115–122 (2005).

[33] Kabanemi K. K., Vaillancourt H., Wang H., Salloum G.: Residual stresses, shrinkage, and warpage of complex injection molded products: Numerical simulation and experimental validation. Polymer Engineering and Science, **38**, 21–37 (1998).
DOI: 10.1002/pen.10162

[34] Pomerteau J., Sanschagrin B.: Injection molding shrinkage of PP: Experimental progress. Polymer Engineering and Science, **46**, 1275–1283 (2006).
DOI: 10.1002/pen.20595

[35] Otkem H., Erzurumlu T., Uzman I.: Application of Taguchi optimization technique in determining plastic injection molding process parameters for thin-shell part. Materials and Design, **28**, 1271–1278 (2007).
DOI: 10.1016/j.matdes.2005.12.013

[36] Hedesiu C., Demco D. E., Kleppinger R., Vanden Poel G., Gijsbers W., Blü1mich B., Remerie K., Litvinov V. M.: Effect of temperature and annealing on the phase composition, molecular mobility, and the thickness of domains in isotactic polypropylene studied by proton solid-state NMR, SAXS, and DSC. Macromolecules, **40**, 3977–3989 (2007).
DOI: 10.1021/ma070014q

[37] Postawa P., Koszkul J.: Change in injection moulded parts shrinkage and weight as a function of processing parameters. Journal of Materials Processing and Technology, **162–163**, 109–115 (2005).
DOI: 10.1016/j.jmatprotec.2005.02.241

[38] Kramschuster A., Cavitt R., Ermer D., Chen Z. B., Turng L-S.: Effet of processing conditions on shrinkage and warpage and morphology of injection moulded parts using microcellular injection moulding. Plastics, Rubber and Composites, **35**, 198–209 (2006).
DOI: 10.1179/174328906X128199

[39] Taguchi G., Konishi S., Wu Y.: Taguchi methods: Research and development. ASI, Dearborn (1992).

[40] Huang M-C., Tai C-C.: The effective factors in the warpage problem of an injection-molded part with thin shell feature. Journal of Materials Processing Technology, **110**, 1–9 (2001).
DOI: 10.1016/S0924-0136(00)00649-X

[41] Fourdrin S., Soulestin J., Lafranche E., Lacrampe M-F., Krawczak P.: Dimensional accuracy and stability of polypropylene-clay nanocomposites injection-mouldings. in 'PPS-23, The Polymer Processing Society 23rd Annual Meeting, Salvador, Brasil' CD-ROM P03-040 (2007).

eXPRESS Polymer Letters Vol.3, No.10 (2009) 639–649
Available online at www.expresspolymlett.com
DOI: 10.3144/expresspolymlett.2009.80

Comparison of the influence of Cu micro- and nano-particles on the thermal properties of polyethylene/Cu composites

J. A. Molefi[1], *A. S. Luyt*[1*], *I. Krupa*[2]

[1]Department of Chemistry, University of the Free State (Qwaqwa Campus), Private Bag X13, Phuthaditjhaba, 9866, South Africa
[2]Polymer Institute, Slovak Academy of Sciences, 842 36 Bratislava, Slovak Republic

Received 19 May 2009; accepted in revised form 8 August 2009

Abstract. Polyethylene (LDPE, LLDPE and HDPE) composites with different copper (micro- and nano-sized particles) contents were prepared by melt mixing and compression moulding. The melting and crystallization behaviour of the different composites was analysed using a differential scanning calorimeter (DSC), and the thermal stability in a thermogravimetric analyser (TGA). The thermal conductivities of the samples were also determined. The DSC results show that the Cu micro- and nano-particles influence the crystallization behaviour of the polyethylenes in different ways. The extent to which the copper particles influence the crystallization behaviour of the polyethylenes also depends on the respective morphologies of the different polyethylenes. The TGA results show an observable influence of both the presence of copper and the sizes of the copper particles on the thermal stabilities of the polymers. Thermal conductivities increased with increasing Cu content, but there was little difference between the thermal conductivities of the samples containing Cu micro- and nano-particles.

Keywords: *polymer composites, polyethylene/Cu, crystallization behaviour, thermal stability*

1. Introduction

This paper forms part of a comprehensive study on the use of copper micro- and nano-particles to improve thermal conductivity in phase change materials for thermal energy storage based on polyethylene/wax blends. This paper reports on the influence of Cu micro- and nano-particles on the thermal properties of polyethylene/Cu composites for three different types of polyethylene, and changes in these properties are explained in terms of morphology differences between the different polyethylenes.

The thermal properties of polyethylenes filled with copper particles were investigated by a few groups [1–3]. One study compared composites that contained respectively micro- and nano-sized particles [3]. The authors showed that incorporation of micro- or nano-sized Cu particles into LDPE reduced the melting temperature, increased the crystallization temperature, and lowered the degree of crystallinity of the matrix of the composites. Similar effects were observed for the melting peak temperatures, melting enthalpies and crystallinities of LDPE and LLDPE filled with copper particles [1]. It was found that the degree of crystallinity of the matrix of the nanocomposites was lower than that of the microcomposites [3]. In another study two different copper particle sizes (both in the

*Corresponding author, e-mail: LuytAS@qwa.ufs.ac.za

micron range) were used as fillers in a PP matrix [2]. This study showed an insignificant change in matrix crystallinity. The influence of graphite, another possible filler to improve the thermal conductivity of phase change materials, on the change in the degree of crystallinity of HDPE was studied by Krupa *et al*. [4]. A slight decrease in the melting temperature of the composites was observed, which suggested that the filler reduced the lamellar thickness of the crystallites. The same behaviour was observed in another study [5], where both HDPE and PS were filled with 60 wt% of graphite. Silver-coated polyamide (PA6) particles were also used as filler for HDPE [6]. In this case a slight decrease in the degree of crystallinity with an increase in silver-coated PA6 particle content was observed.

Generally, the literature focused on the thermal conductivities of metal containing polymers. However, a few papers are devoted to the thermal stability of polyethylene filled with metals [1, 3, 7]. When LDPE/Cu nano- and micro-composites were compared [3], the thermal decomposition temperatures of the nano-composites increased sharply at low Cu nano-particle contents, and reached an optimum value at 2 wt% Cu, after which it decreased with further increase in nano-Cu content. In the case of the LDPE/Cu micro-composites, the optimum thermal stability was reached only after addition of 6 wt% Cu, but higher Cu contents did not further reduce the thermal stability. A study by Luyt *et al*. [1] showed that the thermal stability of LDPE/Cu micro-composites increased, whereas the thermal stability of LLDPE/Cu micro-composites decreased, with increasing Cu content. Yang *et al*. [8] studied the thermal stability of aligned vapour grown carbon nano-fibre reinforced polyethylene samples drawn at different take-up speeds, and all these composites showed higher thermal stability than pure HDPE.

Polymers are materials with very low thermal conductivity values that roughly vary from 0.15 $W \cdot m^{-1} \cdot K^{-1}$ for amorphous polymers to 0.5 $W \cdot m^{-1} \cdot K^{-1}$ for highly crystalline polymers such as HDPE [9]. Several inorganic materials, graphite or metallic powders, are frequently used as thermally conductive fillers [10, 11]. Silver, copper and alumina particles are the most commonly used fillers due to their high inherent thermal conductivity [5, 10–12]. Krupa *et al*. [13] demonstrated that metal-coated particles can be effectively used to improve the thermal conductivity of, for example, HDPE. The study was based on HDPE filled with silver-coated polyamide (PA). It was found that very low silver content, if deposited on the PA particles, significantly improved the thermal conductivity of the composites. Boudenne *et al*. [2] investigated the thermal conductivity of polypropylene filled with two different sizes (23 and 230 μm) of copper particles. A non-linear increase in the thermal conductivity was observed with an increase in the volume fraction of both fillers. At a given filler concentration, a higher thermal conductivity was observed in the composite filled with the smaller Cu particles. This difference was more significant at higher filler concentrations.

2. Experimental

In this work, LDPE and LLDPE were supplied in pellet form by Sasol Polymers. LDPE has an MFI of 7.0 g/10 min (ASTM D-1238), a melting point of 106°C, a molecular weight of 96 000 $g \cdot mol^{-1}$, and a density of 0.918 $g \cdot cm^{-3}$ and LLDPE has an MFI of 1.0 g/10 min (ASTM D-1238), a molecular weight of 191 600 $g \cdot mol^{-1}$, a melting point of 124°C, and a density of 0.924 $g \cdot cm^{-3}$. HDPE was supplied in pellet form by DOW Chemicals. It has an MFI of 8 g/10 min (ASTM D-1238), a molecular weight of 168 000 $g \cdot mol^{-1}$, a melting point of 130°C, and a density of 0.954 $g \cdot cm^{-3}$. Soft paraffin wax (M3 wax) was supplied in powder form by Sasol Wax. It has an average molar mass of 440 $g \cdot mol^{-1}$ and a carbon distribution between C15 and C78. Its density is 0.90 $g \cdot cm^{-3}$ and it has a melting point range around 40–60°C. Merck Chemicals in South Africa supplied the copper powder, which was used as one of the conducting fillers. It has a melting point of 1083°C and a density of 8.96 $g \cdot cm^{-3}$, and the particles sizes were less than 38 μm determined by using a laboratory test sieve with a pore sizes of 38 μm. The copper nano-particles were supplied by Lawrence Packaging Supply Corp., Moonachie, New Jersey, USA, Lot # R402 and the particle size was 50 nm.

All the samples were prepared by mixing the components in a Brabender Plastograph 50 ml internal mixer at 160°C and a speed of 70 rpm for 15 min. After the mixing, the samples were melt pressed at 100 bar and 160°C for 15 min.

DSC analyses were done in a Perkin-Elmer Pyris-1 differential scanning calorimeter under flowing nitrogen (flow rate 20 ml·min^{-1}). The instrument was computer controlled and calculations were done using Pyris software. It was calibrated using the onset temperatures of melting of indium and zinc standards, as well as the melting enthalpy of indium. Samples (5–10 mg) were sealed in aluminium pans and heated from –40 to 160°C at a heating rate of 10°C min^{-1}, and cooled at the same rate. For the second scan, the samples were heated and cooled under the same conditions. The peak temperatures of melting and crystallization, as well as melting and crystallization enthalpies were determined from the second scan. All DSC measurements were repeated three times for each sample. The melting and crystallization temperatures, as well as enthalpies, are reported as average values with standard deviations.

TGA analysis was carried out on a Perkin-Elmer TGA7 thermogravimetric analyser. Samples ranging between 5 and 10 mg were heated from 30 to 650°C at a heating rate of 20°C·min^{-1} under flowing nitrogen (flow rate 20 ml·min^{-1}). The instrument was computer controlled and calculations were done using Pyris software.

A Shimadzu model ZU SSX-550 Superscan scanning electron microscope was used for the SEM analyses. All the samples were frozen in liquid nitrogen, then fractured by simply breaking the specimens in an appropriate size to fit in the specimen chamber, and then mounted onto the holder. The surfaces of the samples were coated with gold by an electro-deposition method to impart electrical conduction before recording the SEM micrographs. This was done to prevent the accumulation of static electric charge on the specimen during electron irradiation.

The thermal conductivity was measured using a multi-purpose apparatus ISOMET, (Applied Precision, Bratislava, Slovakia) for non-steady measurements of thermal properties. The thermal conductivity values were calculated automatically from a time dependence of the thermal flow in the material. Samples were melt-pressed into spherical (7 cm diameter) 1 mm thick sheets in a hot-melt press at 160°C for 5 min at a pressure of 100 bar. Thereafter, measurements were made at 25±2°C with a flat probe.

3. Results and discussion

The morphologies of the composites were studied by SEM analysis of the fracture surfaces of the

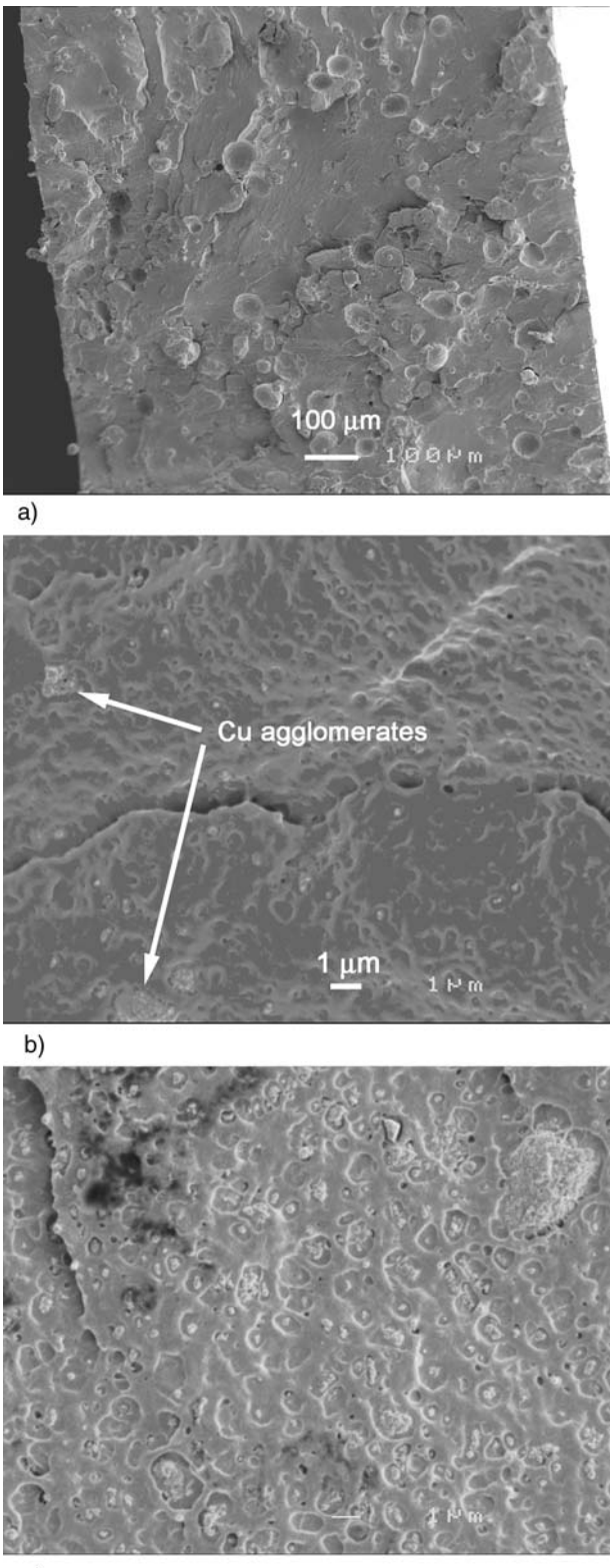

Figure 1. SEM images of (a) a 90/10 v/v LDPE/Cu micro-composite (b) a 99/1 v/v LDPE/Cu nano-composite, and (c) a 95/5 v/v LDPE/Cu nano-composite

composites. Figure 1a shows a fair dispersion of micro-particles, with no obvious agglomeration. As can be seen in Figures 1b and 1c, the Cu nano-particles are fairly well dispersed, but also form agglomerates. To optimally improve the conductivity of the composites, it is important for the particles to form a percolation network within the polymer matrices. No such network formation was observed in the SEM images of the investigated samples. In Figure 1a there seems to be voids around the Cu particles, which indicate that the interaction between the polymer and the Cu particles was weak. The lack of adhesion between the polymer and filler indicates poor interfacial interaction. As the content of Cu particles increased, the agglomeration of the particles also increased.

Figure 2 shows the DSC heating curves for pure LDPE, LLDPE, and HDPE. The curves show endotherms with melting peak temperatures at 107, 128 and 135°C for LDPE, LLDPE and HDPE. Pure HDPE has a relative high enthalpy value of 149.3 J·g^{-1}, while LLDPE and LDPE have enthalpies of 86.9 and 75.4 J·g^{-1}. These values are in line with the known crystallinities of the respective polyethylenes.

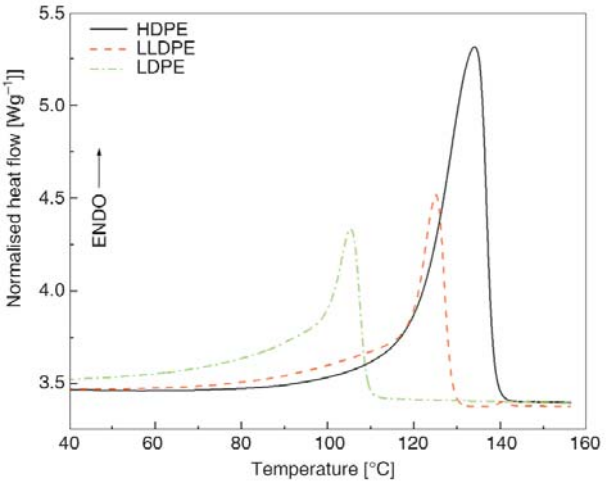

Figure 2. DSC heating curves of the pure polyethylenes

Table 1 shows the DSC results of the different polyethylenes and their Cu micro-composites. For the LDPE/Cu micro-composites the peak temperatures of melting did not significantly change and are within experimental error. From this it is clear that the presence of up to 20 vol% of Cu micro-par-

Table 1. DSC results for polyethylene/Cu micro-composites

v/v	$T_{p,m}$ [°C]	ΔH_m^{obs} [J·g^{-1}]	ΔH_m^{calc} [J·g^{-1}]	$T_{p,c}$ [°C]	ΔH_c^{obs} [J·g^{-1}]
LDPE/Cu					
100/0	106.8 ± 1.5	75.4 ± 6.2	–	91.7 ± 0.6	–63.7 ± 7.6
99/1	107.1 ± 1.4	61.5 ± 6.3	68.8 ± 5.6	91.5 ± 1.0	–57.0 ± 6.9
97/3	106.6 ± 1.7	51.3 ± 8.3	58.1 ± 4.7	91.4 ± 0.7	–41.2 ± 4.1
95/5	106.3 ± 1.2	39.9 ± 2.6	49.8 ± 4.1	91.8 ± 1.1	–43.5 ± 4.9
90/10	106.4 ± 1.1	23.4 ± 1.8	36.2 ± 6.4	91.8 ± 0.9	–27.6 ± 3.2
85/15	105.8 ± 0.8	18.6 ± 1.6	27.8 ± 4.6	92.8 ± 0.9	–21.3 ± 3.9
80/20	106.0 ± 0.9	14.4 ± 0.4	21.9 ± 3.4	92.2 ± 0.8	–16.0 ± 3.1
75/25	105.5 ± 1.2	10.4 ± 2.7	17.9 ± 1.5	92.9 ± 1.1	–12.4 ± 2.2
LLDPE/Cu					
100/0	127.7 ± 2.1	86.9 ± 1.0	–	109.6 ± 0.9	–50.1 ± 0.8
99/1	127.9 ± 1.2	69.4 ± 4.5	79.3 ± 0.9	110.2 ± 1.0	–45.2 ± 2.0
97/3	126.8 ± 1.3	58.8 ± 4.5	66.6 ± 0.8	110.0 ± 1.3	–37.7 ± 4.1
95/5	126.2 ± 0.5	45.3 ± 9.7	57.4 ± 0.6	110.3 ± 1.3	–32.7 ± 2.5
90/10	126.5 ± 1.3	30.9 ± 7.0	41.7 ± 0.5	110.9 ± 1.7	–22.2 ± 3.4
85/15	125.4 ± 1.4	19.6 ± 4.3	31.9 ± 0.4	111.6 ± 1.2	–17.1 ± 4.5
80/20	125.5 ± 1.4	15.2 ± 3.4	25.3 ± 0.3	111.0 ± 1.3	–14.3 ± 3.1
75/25	125.4 ± 1.6	10.2 ± 2.5	20.6 ± 0.3	112.5 ± 1.3	–10.4 ± 4.2
HDPE/Cu					
100/0	134.7 ± 0.5	149.3 ± 11.7	–	113.9 ± 1.1	–134.8 ± 2.6
99/1	134.1 ± 1.3	138.1 ± 3.1	136.2 ± 10.6	114.3 ± 0.1	–132.1 ± 2.1
97/3	133.6 ± 0.1	110.4 ± 7.3	115.0 ± 9.0	115.0 ± 0.9	–110.4 ± 0.4
95/5	132.6 ± 0.3	101.8 ± 0.8	98.5 ± 7.6	114.7 ± 0.6	–97.0 ± 2.3
90/10	131.6 ± 0.2	67.4 ± 6.7	71.7 ± 5.6	115.3 ± 0.3	–72.0 ± 1.6
85/15	131.4 ± 0.2	52.3 ± 8.0	54.8 ± 4.3	115.7 ± 0.2	–53.3 ± 0.3
80/20	130.8 ± 0.5	41.4 ± 1.6	43.4 ± 3.1	116.0 ± 0.4	–43.9 ± 0.3
75/25	130.2 ± 0.2	27.2 ± 9.8	35.2 ± 2.8	116.3 ± 0.6	–34.3 ± 0.4

$T_{p,m}$, ΔH_m^{obs}, ΔH_m^{calc}, $T_{p,c}$, ΔH_c^{obs} are melting peak temperature, observed melting enthalpy, calculated melting enthalpy, crystallization peak temperature, crystallization enthalpy

ticles in LDPE had little influence on the crystallite sizes. However, if the enthalpy values in Table 1 are compared, it is clear that the Cu micro-particles reduce the LDPE chain mobility which gives rise to a lower crystallinity. When the measured melting enthalpy values (ΔH_m^{obs}) are compared with the calculated values (ΔH_m^{calc}), it can be seen that the LDPE in the composites had significantly lower enthalpy (or crystallinity) values than would be expected if it was assumed that the Cu micro-particles had no influence on the LDPE crystallization behaviour. The ΔH_m^{calc} values were calculated from the melting enthalpy of pure LDPE and the weight fractions of LDPE in the respective composites.

A slight decrease in the melting temperature of LLDPE with an increase in Cu content is observed for the LLDPE/Cu micro-composites (Table 1). It seems as if the presence of Cu slightly reduces the LLDPE chain mobility which gives rise to smaller crystallites and a lower crystallinity. In the case of the HDPE/Cu micro-composites, a more observable decrease in the melting temperature of the composites with an increase in Cu content is observed. It seems as if the influence of Cu micro-particles on the crystallite size of polyethylene becomes more significant with decreasing branching and increasing crystallinity of the polymer. Another reason may be that the presence of highly thermally conductive Cu causes a faster heat distribution through the polymer, which will result in a lower melting temperature. Table 1 shows that the ΔH_m^{obs} and ΔH_m^{calc} values are almost the same for all the HDPE/Cu micro-composites, and therefore the presence and amount of Cu had very little influence on the HDPE crystallization behaviour.

The observations described in the previous paragraphs may be explained if it is accepted that the Cu particles will either reduce polymer chain mobility (giving rise to reduced crystallinity) or act as nucleation points for polymer crystallization (giving rise to increased crystallinity). It seems as if the chain structure (and the resultant degree of crystallinity) of the polymer determines which of the two effects will be dominant. Since LDPE and LLDPE are branched, and therefore have significantly lower crystallinities than HDPE, which confirms that the Cu particles are located in the amorphous regions of the polymers. Chain immobilization will then be the more dominant effect, and therefore these polymers show reduced crystallinity in the presence of Cu micro-particles. Since HDPE is much more crystalline, the amorphous regions are much smaller and it is possible that crystallization will start at the Cu surfaces and that Cu particles will act as nucleation points for HDPE crystallization. This explains the slight lowering in HDPE melting temperature (indicating the presence of smaller crystallites). This is consistent with a study done by Xia *et al*. [3]. When they added 13 wt% of Cu micro-particles into an LDPE matrix, the melting peak temperatures of pure LDPE and the LDPE/Cu micro-composites were the same within experimental error. Pure LDPE had a melting enthalpy of 88 $J \cdot g^{-1}$ which reduced to 76 $J \cdot g^{-1}$ when 13 wt% of Cu micro-particles was introduced, and the crystallization temperature increased for the same composition. The increased crystallization temperature was explained as being due to the presence of the Cu micro-particles, which acted as nucleating agents. However, the Cu particles at the same time seemed to have immobilized the LDPE chains, giving rise to reduced crystallinity, as can be seen from the smaller melting enthalpy values.

Table 2 shows the DSC results of the different polyethylenes and their Cu nano-composites. For the LDPE/Cu nano-composites the peak temperatures of melting did not significantly change and are within experimental error. From this it is clear that the presence of up to 5 vol% of Cu nano-particles in LDPE had a negligible influence on the crystallite sizes. On the other hand, if the enthalpy values in Table 2 are compared, it is clear that the presence of the Cu nano-particles restricts the LDPE chain mobility which leads to a lower crystallinity. When the observed melting enthalpy values (ΔH_m^{obs}) are compared with the calculated values (ΔH_m^{calc}), it can be seen that the LDPE in the composites had significantly lower enthalpy (or crystallinity) values than would be expected if it was assumed that the Cu nano-particles had no influence on the LDPE crystallization behaviour.

Similarly, the copper nano-particles in the LLDPE/Cu and HDPE/Cu nano-composites had no significant influence on the melting peak temperatures of the respective polyethylenes. The observed melting enthalpies of these polyethylene composites were also lower than the calculated values. However, the differences between the observed and calculated values seem to decrease with increasing crystallinity from LDPE to LLDPE to HDPE. Since

Table 2. DSC results for polyethylene/Cu nano-composites

v/v	$T_{p,m}$ [°C]	ΔH_m^{obs} [J·g^{-1}]	ΔH_m^{calc} [J·g^{-1}]	$T_{p,c}$ [°C]	ΔH_c^{obs} [J·g^{-1}]
LDPE/Cu					
100/0	106.8 ± 1.5	75.4 ± 6.2	–	91.7 ± 0.6	–63.7 ± 7.6
99/1	105.9 ± 0.3	49.4 ± 2.3	68.8 ± 5.6	90.8 ± 0.1	–54.3 ± 1.9
97/3	105.7 ± 0.1	38.8 ± 0.9	58.1 ± 4.7	91.7 ± 0.3	–48.3 ± 0.8
95/5	105.3 ± 0.1	35.5 ± 1.9	49.8 ± 4.1	91.9 ± 0.1	–41.5 ± 0.6
LLDPE/Cu					
100/0	126.7 ± 2.1	86.9 ± 1.0	–	109.6 ± 0.9	–50.1 ± 0.8
99/1	126.9 ± 0.4	62.6 ± 1.4	79.3 ± 0.9	109.3 ± 0.1	–47.0 ± 4.0
97/3	125.6 ± 0.2	56.6 ± 2.3	66.6 ± 0.8	110.7 ± 0.1	–38.3 ± 2.1
95/5	126.0 ± 0.1	43.9 ± 0.7	57.4 ± 0.6	111.7 ± 0.1	–31.0 ± 2.7
HDPE/Cu					
100/0	134.7 ± 0.5	149.3 ± 9.7	–	113.9 ± 1.1	–134.8 ± 2.6
99/1	133.2 ± 0.2	132.1 ± 2.5	136.2 ± 10.6	113.8 ± 0.2	–126.2 ± 2.2
97/3	133.1 ± 0.1	106.8 ± 1.5	115.0 ± 9.0	113.9 ± 0.3	–109.5 ± 3.2
95/5	134.4 ± 1.0	82.9 ± 0.8	98.5 ± 7.6	114.7 ± 0.3	–90.0 ± 1.6

$T_{p,m}$, ΔH_m^{obs}, ΔH_m^{calc}, ΔH_c^{obs} $T_{p,c}$, are melting peak temperature, observed melting enthalpy, calculated melting enthalpy, and crystallization peak temperature

LDPE and LLDPE are branched, and therefore have lower crystallinities than HDPE, the Cu particles are situated in the amorphous regions of these polymers. Chain immobilization will then be the more dominant effect. Since HDPE is much more crystalline, the amorphous regions are much smaller and therefore the decrease in total crystallinity is less significant.

Figure 3 shows the experimental melting enthalpies as function of Cu content for LDPE/Cu nano- and micro-composites. It can be seen that the experimental melting enthalpies of the LDPE/Cu microparticles are higher than those the of LDPE/Cu nano-composites at the same volume percentages of copper. This clearly shows that the crystallinities of the LDPE/Cu nano-composites are observably lower than those of the LDPE/Cu micro-composites, indicating that Cu nano-particles had a stronger influence on the motion and nucleation of the polymer chain segments. This behaviour indicates that the Cu nano-particles restricted the polymer chain mobility to a larger extent than the Cu micro-particles, probably because the Cu microparticles counteract this effect through their ability to act as nucleating agents that promote the crystallization process of LDPE.

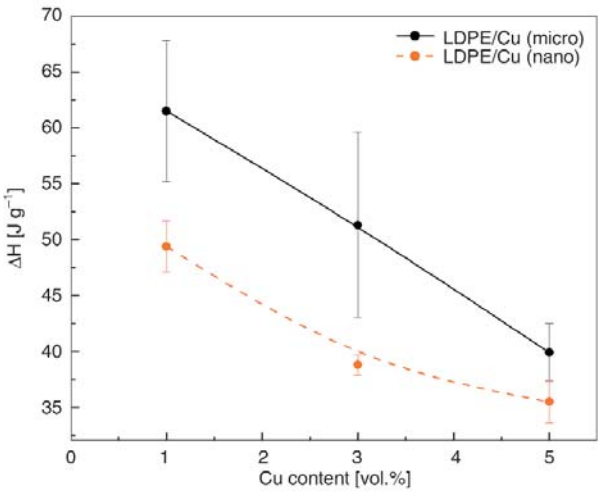

Figure 3. Comparison of ΔH^{obs} values for the melting of LDPE in LDPE/Cu micro- and nano-composites

It seems as if the influence of Cu micro-particles on the crystallite size of polyethylene becomes more significant with decreasing branching and increasing crystallinity of the polymer. Tracz *et al*. [14] found that the nucleating and ordering effects of fillers on polyethylene crystallization depend to a larger extent on the nano-structure of its surface. Nano-particles do not have any nucleating effect, but they act as obstacles for the crystallization of polyethylene. Even though some nano-particle agglomerates may nucleate PE crystallization, the overall influence of the nano-particles on the crystallization of LDPE can be considered to be a retardant effect. Therefore, the degree of crystallinity of LDPE in the nano-composites is lower than that of pure LDPE. Micro-particles can nucleate PE crystallization, because they can provide sufficiently large flat domains. However, the sizes of the microparticles are comparable to the spherulite size of LDPE, and thus the micro-particles also hinder spherulitic growth, so that the degree of crystallinity of LDPE in the presence of micro-particles is not significantly higher than that of the pure LDPE. Huang *et al*. [15] found that the addition of

2 and 4% of Al nano-particles can either facilitate or hinder the crystallization of LDPE, depending on the dispersion of the nano-particles in the polymer. The well-dispersed Al nano-particles did not have a nucleating effect and mainly acted as obstacles, but the agglomerates of Al nano-particles acted as nucleating agents and slightly improved the crystallization. The micro-particles had a nucleating effect and facilitated the crystallization process. These observations and explanations are in line with the results of our study, although in our case the presence of Cu micro-particles was found to reduce the total LDPE crystallinity, but to a smaller extent than the Cu nano-particles. In LDPE/Al micro- and nano-composites and in LDPE/TiO_2 nano-composites the melting behaviour indicated that the lamellar thickness distribution of both nano- and micro-composites did not significantly change compared to that of pure LDPE [14, 15].

The measured enthalpy values of the LLDPE/Cu and HDPE/Cu nano-composites are also lower than those of the micro-composites, but the differences are less significant (Figures 4 and 5). The reason for this is probably the higher crystallinities and lower extent of branching in these polymers, that result in a smaller influence of these particles on the polymer chain mobility. The uncertainties in the ΔH values are relatively high in the case of the microcomposites. The reason for this is probably a bigger size distribution of the micro-particles compared to the nano-particles. Unfortunately we did not statistically determine the size distribution of the micro-particles. Another interesting observation is that the difference between the ΔH values of the respective micro- and nano-composites seems to decrease with increasing filler content in the case of LDPE and LLDPE, while it seems to increase in the case of HDPE. It is difficult to give an exact explanation for this observation, because a number of factors may determine the influence of inorganic particles on the crystallization behaviour of polyethylene. Amongst these are the sizes and size distributions of the filler particles, the dispersion of the particles in the polymer matrix, the effective surface areas of the particles, the crystallinities and crystallization mechanisms of the respective polymers, and the extent of interaction between the polymer and the filler particles. Depending on these factors, the filler particles will immobilize the polymer chains (reducing crystallinity) and/or act as nucleation centres (increasing crystallinity).

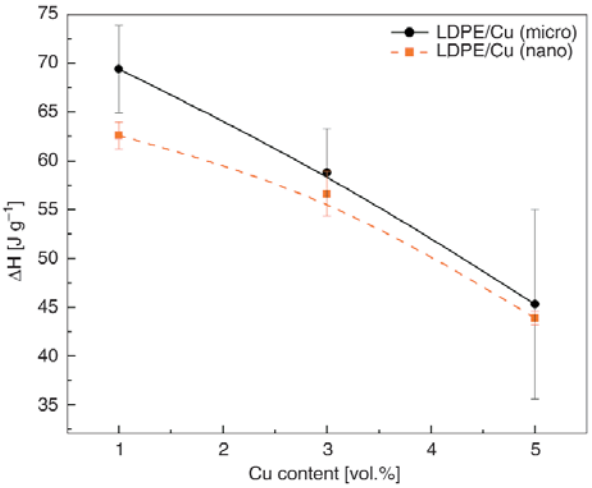

Figure 4. Comparison of ΔH^{obs} valuesfor the melting of LLDPE in LLDPE/Cu micro- and nano-composites

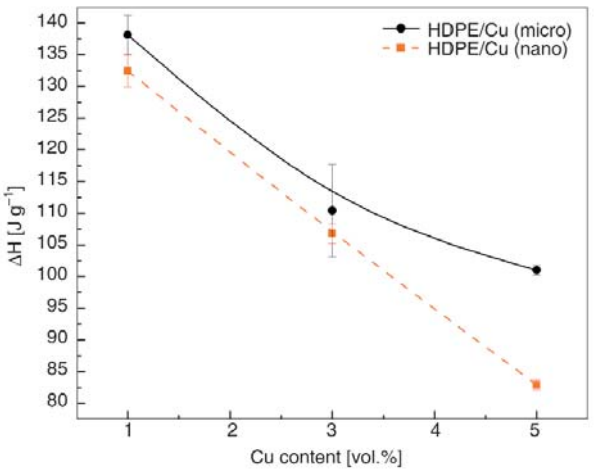

Figure 5. Comparison of ΔH^{obs} values for the melting of HDPE in HDPE/Cu micro- and nano-composites

Although high-temperature thermal stability of these composites does not directly influence their applications, it is interesting to see how the thermal stabilities of the polymers are influenced by the presence of copper filler, and whether these observations can be explained by the same morphological features used to explain the influence of copper particles on the crystallization behaviour of the PE matrices. TGA studies were also used to establish the dispersion efficiency of the copper particles in the matrix. The TGA data of the PE/Cu micro-composites are summarized in Table 3. There is a non-linear increase in thermal stability with an increase in Cu micro-particle content up to 20 vol%. This is probably due to the inability of the polymer chains to move freely because of the presence of Cu

Table 3. Temperatures of 10% degradation and DTG peak temperatures, as well as wt% of residue, of PE/Cu micro-composites

v/v	T_{10} [°C]	T_{peak} [°C]	wt% residue	wt% Cu in sample
LDPE/Cu				
100/0	443.3	485.5	–	–
99/1	449.7	487.6	7.3	8.8
95/5	454.3	489.9	32.6	33.0
90/10	459.7	485.2	51.7	52.0
80/20	461.2	480.2	69.9	69.0
LLDPE/Cu				
100/0	454.1	492.9	–	–
99/1	468.5	501.8	9.7	8.9
95/5	461.4	491.7	34.0	33.1
90/10	470.4	488.9	52.0	52.2
80/20	470.4	485.4	70.3	69.5
HDPE/Cu				
100/0	467.0	500.1	–	–
99/1	463.6	496.3	8.8	8.5
95/5	469.2	497.3	32.3	33.0
90/10	455.2	485.7	50.4	51.0
80/20	458.4	471.4	69.4	69.7

micro-particles, which will retard the movement of free radical chains and inhibit the degradation process. Another reason may be that the diffusion of the volatile degradation products may be retarded by the presence of the copper particles, which will lead to these products only coming off at higher temperatures. In other studies [3, 16] it was also found that an increase in conductive filler content enhances the thermal stability of LDPE. Krump *et al.* [16] found that the thermal stability of LDPE/Cu micro-composites increased with an increase in Cu micro-particle content. Xia *et al.* [3] showed that the optimum thermal stability was reached after addition of 6 wt% Cu, but at higher Cu contents the thermal stability remained constant. Omastová *et al.* [17] showed that carbon black (CB) and modified CB in an LDPE matrix improved the thermal stability of the filled composites, with modified CB having a more significant effect.

The thermal stability of LLDPE improves with an increase in Cu micro-particles up to 1–3 vol% Cu, and the temperature at maximum decomposition rate increases for 1 vol% Cu, after which it decreases (Table 3). This is in line with the observations by Xia *et al.* [3], but differs from the observations on the LDPE/Cu composites, probably because of the higher crystallinity of LLDPE which results in more intimate contact between the Cu and the LLDPE crystals (especially at higher Cu contents). The higher heat capacity and thermal conductivity of copper then causes more effective heat transfer to the LLDPE crystals. In the case of HDPE there is no clear trend for the influence of Cu content on its thermal stability and it seems that, within experimental error, the Cu micro-particles did not significantly influence its thermal stability. This is probably the result of a balance between thermal stability enhancement and thermal degradation initiation effects by the copper particles. The higher thermal conductivity of the metallic Cu particles may override its stiffening effect. Since HDPE is highly crystalline and inherently less thermally conductive, the transfer of heat through the entire sample is delayed. When the Cu content is above 10 vol%, there may be a strong interconnection between the Cu particles, resulting in increased thermal stability. This may also be attributed to the hindered polymer chain mobility enforced by the Cu micro-particles.

The TGA results of the PE/Cu nano-composites are summarized in Table 4. The thermal stability of LDPE and LLDPE generally increases with increasing Cu nano-particle content, but for LDPE a decrease is observed for the highest Cu content of 5 vol%. This decrease in thermal stability is probably due to the presence of Cu nano-particle agglomerates that cause an increase in energy propagation. The formation of these agglomerates was observed in the SEM results (Figure 1). The delayed thermal degradation for both LDPE/Cu and LLDPE/Cu

Table 4. Temperatures of 10% degradation and DTG peak temperatures, as well as wt% of residue, of PE/Cu nano-composites

v/v	T_{10} [°C]	T_{peak} [°C]	wt% residue	wt% Cu in sample
LDPE/Cu				
100/0	443.3	485.5	–	–
99/1	456.0	480.7	8.4	8.8
97/3	458.0	491.4	22.0	23.1
95/5	440.2	480.9	33.4	33.0
LLDPE/Cu				
100/0	454.1	492.9	–	–
99/1	441.8	491.7	10.5	8.9
97/3	464.6	495.9	22.5	23.0
95/5	468.1	495.6	33.4	33.1
HDPE/Cu				
100/0	467.0	500.1	–	–
99/1	409.7	460.0	9.7	8.9
97/3	437.3	484.1	26.3	23.0
95/5	460.9	486.3	31.2	33.0

nano-composites is due to the restricted chain and volatile degradation products mobility imposed by the Cu nano-particles. In all of these polyethylenes filled with Cu particles, the shift towards higher temperature is in the order of their polymer chain regularity. There is an increase in residue with increasing Cu content for all the investigated samples, and these values are in line with the initial wt% Cu mixed into the samples (Tables 3 and 4). This indicates that the presence of Cu particles did not cause any char formation.

The thermal conductivities of the PEs (LDPE, LLDPE and HDPE) filled with copper micro-particles are presented in Figure 6. A non-linear increase in thermal conductivities is observed with an increase in copper content. This is foreseeable, because the filler has a significantly higher thermal conductivity than the polymeric matrices. It can be seen that thermal conductivities of the HDPE/Cu micro-composites are higher than those of both the LLDPE/Cu and LDPE/Cu micro-composites. This is due to the higher degree of crystallinity of the HDPE matrix. In the case of semi-crystalline polymers, an increase in thermal conductivity with an increase in crystalline content was observed as a consequence of the better transport of heat in the crystalline phase [4]. The simple relation between thermal conductivity of semi-crystalline polymers and the weight fraction of the crystalline phase is expressed in terms of the additive rule [18], given by Equation (1):

$$\lambda_m = \lambda_c w_c + \lambda_a w_a \quad (1)$$

where λ_m, λ_c, λ_a are the thermal conductivities of the polymer and its crystalline and amorphous phases, respectively, and w_c, w_a are the weight fractions of the crystalline and amorphous phases of the polymer.

Generally, most inorganic fillers have much higher thermal conductivity than polymers, and therefore their incorporation into the polymers leads to an increase in thermal conductivity of the composites [5, 19]. Unfortunately, the prediction of thermal conductivity of filled polymers is very difficult and depends on the geometry and orientation of the filler particles in the matrix, the concentration of the filler, and the ratio between the thermal conductivity of the filler and the thermal conductivity of the matrix. Based on these factors, many different models have already been developed, but none of them has general validity, since most of the models are derived for regularly shaped particles, flakes or fibres that have a uniform size distribution. In this study, the copper particles were not regular.

The presence of copper nano-particles in the polymer matrices also increases the thermal conductivity of the nano-composites over that of the pure polymers (Figure 7). The copper nano-particles also improve the thermal conductivity of the composites. HDPE filled with nano-particles shows the highest thermal conductivity, similar to the micro-composites. The thermal conductivities of the nano-composites were in the same as those of the micro-composites, for the same volume fractions of copper filler.

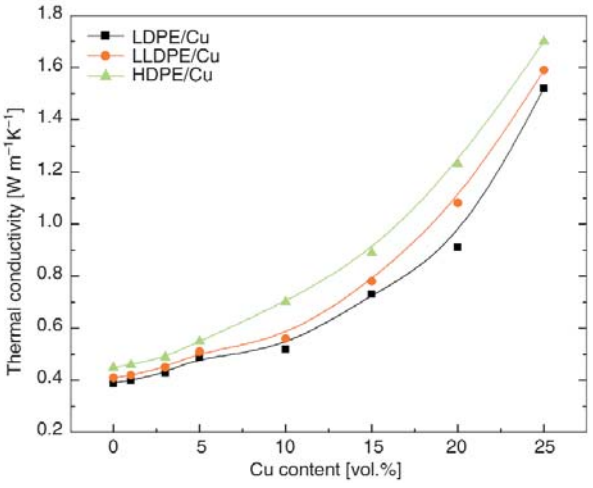

Figure 6. Thermal conductivity of the polyethylene composites as function of Cu micro-particle content

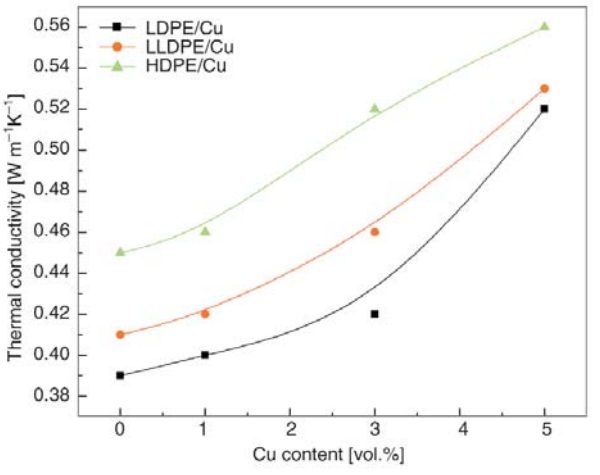

Figure 7. Thermal conductivity of the polyethylene composites as function of Cu nano-particle content

4. Conclusions

This paper discussed the morphology and thermal properties of the composites of three different polyethylenes (LDPE, LLDPE and HDPE) with Cu micro- and nano-particles. No previous paper reports such a comparative investigation. The Cu particles in the PE/Cu micro-composites were fairly well dispersed in the polymer matrix, but as the filler content increased, voids around the Cu particles were observed indicating poor interaction between the polymer and the Cu micro-particles. The lack of adhesion between the polymer and filler indicates poor interfacial interaction. The Cu nano-particles were well dispersed in the polymer matrix, except that they tended to form agglomerates. Incorporation of both Cu micro- and nano-particles into the different polyethylenes reduced the crystallinities of the different polyethylenes. Generally the nano-composites had a more significant influence because of the larger total surface area of these particles. Even though the nano-particles tended to form agglomerates, their influence was still more significant than that of the micro-particles. The micro-particles generally had a nucleating effect and facilitated the crystallization process, while the well dispersed nano-particles hindered the crystallization of polyethylene. Since linear chain polyethylenes are more difficult to decompose than the branched ones, the pure LDPE degraded at much lower temperatures compared to LLDPE and HDPE. Generally the presence of Cu particles in the polyethylenes showed an increase in thermal stability with increasing Cu content, indicating that the Cu particles either immobilized the free radical chains or inhibited the diffusion of the volatile degradation products. The Cu nano-particles had a more significant influence than the micro-particles, and the influence of both types of particles became less significant with increasing polymer crystallinity. Thermal conductivities increased with increasing Cu content, but there was little difference between the thermal conductivities of the samples containing Cu micro- and nano-particles.

Acknowledgements

The National Research Foundation of South Africa (GUN 62693) and the University of the Free State are acknowledged for financial support of this research.

References

[1] Luyt A. S., Molefi J. A., Krump H.: Thermal, mechanical and electrical properties of copper powder filled low-density and linear low-density polyethylene composites. Polymer Degradation and Stability, **91**, 1629–1636 (2006).
DOI: 10.1016/j.polymdegradstab.2005.09.014

[2] Boudenne A., Ibos I., Fois M., Majestè J. C., Gehn E.: Electrical and thermal behaviour of polypropylene filled with copper particles. Composites Part A: Applied Science and Manufacturing, **36**, 1545–1554 (2005).
DOI: 10.1016/j.compositesa.2005.02.005

[3] Xia X., Cai S., Xie C.: Preparation, structure and thermal stability of Cu/LDPE nanocomposites. Materials Chemistry and Physics, **95**, 122–129 (2006).
DOI: 10.1016/j.matchemphys.2005.05.010

[4] Krupa I., Novák I., Chodák I.: Electrically and thermally conductive polyethylene/graphite composites and their mechanical properties. Synthetic Metals, **145**, 245–252 (2004).
DOI: 10.1016/j.synthmet.2004.05.007

[5] Krupa I., Chodák I.: Physical properties of thermoplastic/graphite composites. European Polymer Journal, **37**, 2159–2168 (2001).
DOI: 10.1016/S0014-3057(01)00115-X

[6] Krupa I., Miková G., Novák I., Janigová I., Nógellová Z., Lednický F., Prokeš J.: Electrically conductive composites of polyethylene filled with polyamide particles coated with silver. European Polymer Journal, **43**, 2401–2413 (2007).
DOI: 10.1016/j.eurpolymj.2007.03.033

[7] Murty M. V. S., Grulke E. A., Bhattacharyya D.: Influence of the metallic on thermal degradation and liquefaction of high density polyethylene (HDPE). Polymer Degradation and Stability, **61**, 421–430 (1998).
DOI: 10.1016/S0141-3910(97)00228-0

[8] Yang S., Taha-Tijerina J., Serrato-Diaz V., Hernandez K., Lozano K.: Dynamic mechanical and thermal analysis of aligned vapor grown carbon nanofiber reinforced polyethylene. Composites Part B: Engineering, **38**, 228–235 (2007).
DOI: 10.1016/j.compositesb.2006.04.003

[9] Bandrup J., Immergut E., Grulke E.: Polymer handbook. Wiley, New York (1999).

[10] Sundstrom D. W., Lee Y-D.: Thermal conductivity of polymers filled with particulate solids. Journal of Applied Polymer Science, **16**, 3159–3167 (1972).
DOI: 10.1002/app.1972.070161210

[11] Bujard P., Munk K., Kuehnlein G.: Thermal conductivity. Technomic Publishing, Lancaster, (1994).

[12] Boudenne A., Ibos L., Géhin E., Fois M., Majesté J. C.: Anomalous behavior of thermal conductivity and diffusivity in polymeric materials filled with metallic particles. Journal of Materials Science, **16**, 4163–4164 (2005).
DOI: 10.1007/s10853-005-3818-2

[13] Krupa I., Boudenne A., Ibos L.: Thermophysical properties of polyethylene filled with metal coated polyamide particles. European Polymer Journal, **43**, 2443–2452 (2007).
DOI: 10.1016/j.eurpolymj.2007.03.032

[14] Tracz A., Kucinska I., Wostek-Wojciechowska D., Jeszka J. K.: The influence of micro- and nano-particles on model atomically flat surfaces on crystallization of polyethylene. European Polymer Journal, **41**, 501–509 (2005).
DOI: 10.1016/j.eurpolymj.2004.09.019

[15] Huang X., Ke Q., Kim C., Zhong H., Wei P., Wang G., Liu F., Jiang P.: Nonisothermal crystallization behaviour and nucleating of LDPE/Al nano- and micro-composites. Polymer Engineering and Science, **47**, 1052–1061 (2007).
DOI: 10.1002/pen.20784

[16] Krump I., Luyt A. S., Molefi J. A.: Changes in free surface energy as an indicator of polymer blend miscibility. Materials Letters, **59**, 517–519 (2005).
DOI:10.1016/j.matlet.2004.10.039

[17] Omastová M., Podhradská S., Prokeš J., Janigová I., Stejskal J.: Thermal ageing of conducting polymeric composites. Polymer Degradation and Stability, **82**, 251–256 (2003).
DOI: 10.1016/S0141-3910(03)00218-0

[18] Park J. W., Oh S. C., Lee H. P., Kim T., Yoo K. O.: A kinetic analysis of thermal degradation of polymers using a dynamic method. Polymer Degradation and Stability, **67**, 535–540 (2000).
DOI: 10.1016/S0141-3910(99)00155-X

[19] Rusu M., Sofian N., Rusu D.: Mechanical and thermal properties of zinc powder filled high density polyethylene composites. Polymer Testing, **20**, 409–417 (2001).

eXPRESS Polymer Letters Vol.3, No.10 (2009) 650–656
Available online at www.expresspolymlett.com
DOI: 10.3144/expresspolymlett.2009.81

Mechanical and falling weight impact properties of unidirectional phormium fibre/epoxy laminates

C. Santulli[1*], *G. Jeronimidis*[2], *I. M. De Rosa*[3], *F. Sarasini*[3]

[1]Electrical Engineering Department, Università di Roma – La Sapienza, Via Eudossiana 18 00184 Roma, Italy
[2]Centre for Biomimetics, School of Construction Management and Engineering University of Reading, Whiteknights, RG6 6AY, United Kingdom
[3]Research Center for Nanotechnologies applied to Engineering (CNIS) Università di Roma – La Sapienza, Via Eudossiana 18, 00184 Roma, Italy

Received 25 June 2009; accepted in revised form 10 August 2009

Abstract. The falling weight impact properties of composites obtained by introducing 16 wt% of *phormium tenax* fibres extracted with two different methods i.e., either manually or by paddocking and scutching and in both cases chemically treated with a 1% solution of sodium hydroxide, have been investigated. The effect of the two extraction methods on fibre characteristics is compared by the tensile properties of the fibres and the flexural properties, fracture modes and hysteresis cycles parameters (impact energy partition, linear stiffness and normalised penetration energy) of final laminates.
Laminates obtained using paddocked and scutched fibres are clearly superior to those manufactured using the manually extracted fibres: this is due to the more effective fibre impregnation in the former case than in the latter, which results in an improved dissipation of energy during the damping phase of the impact event. It is noteworthy, however, that the low volume of fibres introduced in the laminate with the manufacturing method adopted does not allow obtaining properties comparable with other semi-structural plant fibre composites, such as e.g., hemp fibre reinforced laminates.

Keywords: *polymer composites, fibre extraction, phormium, falling weight impact testing, hysteresis curves*

1. Introduction

Natural fibre composites represent a possible route for obtaining more carbon-dioxide neutral materials [1]. The fibres most frequently used in composites aimed at semi-structural applications are mainly bast extracted ones, such as jute, flax and hemp, and a few extracted from other parts of the plant, such as from the fruit skin e.g., coir, or from the leaf e.g., sisal, abaca or pineapple, although studies on a much larger number of natural fibres in composites are present in literature [2]. Concentrating on the leaf fibres, while on one side these appear to be promising for obtaining long stretches of aligned fibres, on the other side they are formed by bundles of many fibre cells, only a small portion of which contribute effectively to fibre-matrix adhesion [3].
In recent years, a renewed interest has been shown for the fibres extracted from the leaves of the phormium tenax, also known as New Zealand flax, which have a traditional use by the Maori people as fibre for weaving mats and ropes [4]. Phormium leaves grow grouped in fans with the youngest leaf in the centre of the fan and older leaves on the outside: the latter reach considerable length, of up to 3 meters, and average width in the order of 100–150 mm [5]. Extracted fibres contain around 45% cellulose, 30% hemicellulose, 10% lignin, 10%

*Corresponding author, e-mail: carlo.santulli@uniroma1.it

moisture, and little pectin and wax, although their composition is quite variable depending on the cultivar [6].

Some recent work on the application of alkali-treated phormium fibres arranged in mats used as a reinforcement for epoxy composites showed some promising results, as far as flexural properties are concerned. Electron microscopy highlighted the infrequent presence of kink bands in the individual fibre cells and suggested that wrinkled cell-wall surfaces were able to improve the adhesion at fibre-matrix interface [5]. This outcome would in principle suggest a possible use of phormium fibres as a reinforcement for composites. However, a number of issues are still to be addressed: in particular, their impact damage resistance needs to be measured.

In recent years, falling weight impact tests have been performed also on plant fibre composites: a recent study provided some data in this respect [7]. For example, average impact penetration energy of jute (30 vol%)/polyester and of sisal (30 vol%)/polyester composites is equal to 10.6 kJ/m^2 and 12.2 kJ/m^2 respectively: this is obviously very far from what obtained with fibreglass, where for a similar volume of oriented reinforcement, impact penetration energy usually approaches 100 kJ/m^2 [7].

In addition, some other studies on plant fibre composites highlighted the relation between hysteresis cycles and the mode of failure of these materials under impact loading. This has been obtained by measuring a number of variables from the hysteresis cycle, such as linear stiffness, peak load, extent of first load drop, and partition of impact energy in three terms, namely elastic energy, plastic energy and damping (or rebound) energy [8–10].

In this work, the analysis of hysteresis cycles is applied to the comparison of impact properties of unidirectional phormium fibre/epoxy composites obtained with fibres either extracted manually from the leaves, or retted (i.e., paddocked and scutched). The idea is measuring the effect of the process of retting with respect to manual extraction of fibres, in particular considering that the former is more time consuming and possibly more expensive than the latter. The composite has been laminated in different thickness, keeping constant the volume of reinforcement introduced, at 16±1 wt% throughout.

2. Materials and methods

2.1. Fibres extraction

Phormium leaves show an obvious and quite precise alignment of technical fibres, kept together by a limited amount of resin and non fibrous matter, as from Figure 1.

The fibres were extracted with two different methods:

– In the first case (manual extraction), the leaves were cut to a length of 350 mm and left to open up to partly separate hemicellulose and non structural matter and separate the aligned bundles of fibres, in a solution of 1% sodium hydroxide in water. After 24 hours, the fibres are dried from the water in excess, then combed away and separated, so to obtain the technical fibres ready for being impregnated with the polymer resin.

– In the second case (paddocking and scutching), the leaves, as obtained from the plant, hence with length of 2–2.5 m, after removing the curled tips, are washed and fibres are scraped away, trying to preserve straight sections as long as possible. The fibres are then paddocked and scutched. Paddocking involved exposure of the fibres to sun and rain over a few weeks, which again allows separating any non-fibrous matter, which was then removed by scutching. After drying, the fibres were cut at a length of 350 mm to be treated in a solution of 1% sodium hydroxide in water for 24 hours, then dried to be inserted in the mould.

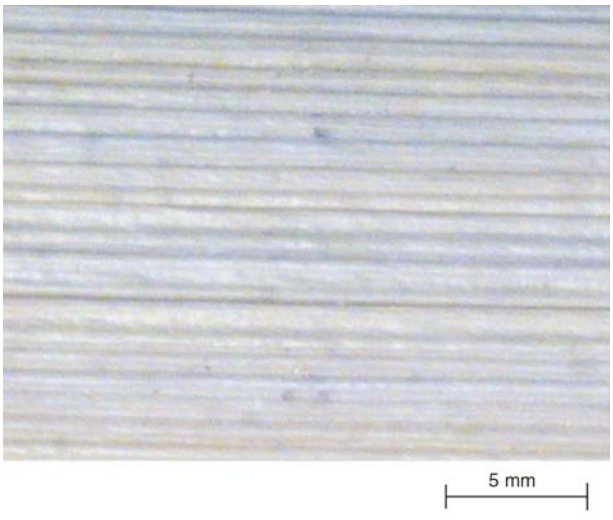

Figure 1. Optical micrograph of a portion of phormium leaf showing aligned fibres

Table 1. Series of samples tested (IFW = Impact by falling weight)

Series	Fibre extracted	Type of test	Thickness [mm]
1	Manually	Flexural and impact (IFW)	3.5
2	Manually	Impact (IFW)	7.0
3	Paddocked and scutched	Flexural	3.5
4	Paddocked and scutched	Impact (IFW)	7.0
5	Paddocked and scutched	Impact (IFW)	10.0

In general, the difference between the two methods is that in the first case, manual extraction may be less damaging for the fibres, also because the exposure to the environment is limited, although it may yield technical fibres of variable diameter. In contrast, in the second case paddocking and scutching is a more severe treatment, which involves fibre separation from the leaves before those which on the other side allow the fibres to be 'cleaner' from non-fibrous matter, and hence possibly the values of fibre diameters would be less scattered.

2.2. Composites manufacturing

The resin used for composites manufacturing was an Ampreg26 epoxy (by SP systems Plc, Isle of Wight, UK), with Ampreg 26 Slow hardener. Lamination was carried out at 20–22°C with 12 hours pressure application and 48 hours post-curing.
Phormium fibre-epoxy laminates were obtained by hand lay-up in a closed matching mould, with planar dimensions 300×150 mm, which allows obtaining a laminate thickness variable from 2 to 10 mm. After cutting, five samples with planar dimensions 250×25 mm were obtained, with different thickness according to the category of samples. All the categories of samples tested are listed in Table 1.

2.3. Fibres tensile testing

The fibres were tested in a universal testing machine model H5KS by Hounsfield Test Equipment Ltd. (Salfords, Redhill, Surrey, UK) equipped with a 1000 N load cell. The fibres were cut to a gauge length of 80 mm, in a way to avoid as much as possible twisting of the microfibres and presence of split ends, and their ends were bonded by cyanoacrylate adhesive on aluminium circular tabs. The tests were carried out in displacement control using a cross-head speed equal to 2 mm/min.

2.4. Composite flexural testing

Flexural tests have been performed in accordance with ASTM D-790 standard on a 4302 testing machine by INSTRON (High Wycombe, Bucks., UK), using a 10 kN load cell, supporting the specimens in a three-point bending rig with 10 mm cylindrical supports and a 200 mm span. Loading was carried out in displacement control at a cross-head speed of 1 mm/min.

2.5. Falling weight impact characterization

Using the same bending rig, falling weight impact tests were carried out. A 12.7 mm impacting head was employed, with a total (cross-head + impactor) 2.5 kg mass. The impact energy was varied by changing the falling height of the mass in an IFW5 impact tower by Rosand (Zwick-Roell, Leominster, Herefordshire, UK). During impact testing, force, time and displacement data were acquired. Impact damage patterns have been characterised under an optical stereo- microscope by Carl Zeiss UK (Welwyn Gardens, Herts., UK) with magnification up to 60×. A scanning electron microscope (SEM) S-2500 by Hitachi Europe (Krefeld – Germany) was also used.

3. Results and discussion

An optimal fibre extraction results in a compromise between the need of obtaining 'clean' fibres, by a complete removal of wax, pectins, etc., and the requirement of not introducing further damage in the technical fibre, apart from the inherent weaker zones, due to the hierarchised structure of the fibre, often referred to as kink bands [11]. As a result, the analysis of the results would principally try to evaluate the level of improvement, both in quasi-static and dynamic properties of the composite laminates, which can be achieved by a longer but sounder extraction process of fibres, which obviously results in higher costs.

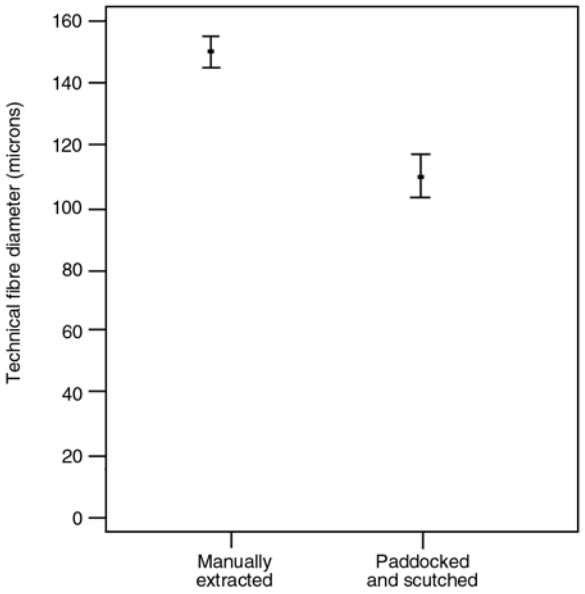

Figure 2. Diameter of technical phormium fibres with the different extraction methods

Measurement by optical microscopy of fibre diameters, as from the results in Figure 2, would indicate that the amount of non-structural matter which is additionally removed by paddocking and scutching would possibly exceed 20% of total weight. The consequent improvement therefore in tensile properties of the fibres with respect to the manually extracted fibres can be suggested to be at least on the same level. In contrast, the results found in practice suggest that, while thorough removal of non-structural results in a very large improvement of fibre tensile strength, which almost double its average value, albeit retaining a very large scattering, fibre stiffness is not substantially improved by paddocking and scutching (Table 2). It can be suggested that the significant variability in the properties of phormium fibres, even obtained from the same cultivar and from leaves selected by hand, as a result of the variable presence of defects and kink bands, as reported in [11], would lead to this increase in average fibre strength. This is to be verified, especially considering that scattering is large for both the extraction methods considered. The higher tensile modulus values would appear more consistent, though, and be due to the significantly higher content in structural matter in the technical fibres, which led to some stiffening effect during loading.

When inserting these fibres into the polymer resin, increasing the thickness of the samples would result in the possibility of improved 'locking-up' between unidirectional long fibres, when applying the pressure at mould closure. This is due to their tendency to microbuckling, as it happens when kink bands are present [12], as it is the case with plant fibres. Also, the manufacturing procedure not including thorough degassing adopted would mean that a higher thickness would possibly result also in the higher presence of microvoids: in addition, the control over fibre directionality would be even more difficult. All the above considerations act as limiting factors on the main concept of increasing laminate thickness in order to get sufficient impact resistance.

The results show that extraction scutching and paddocking markedly increases flexural strength and modulus, while it does not result in a significant improvement of flexural work of fracture, as measured from the area below the bending force vs. deflection curve (Table 3). In practice, it appears that the possibilities of the fibres in terms of deformation are exploited to the fullest when extracting them manually, whilst loading appears to be more effective after paddocking and scutching resulting in a much larger ultimate stress.

An explanation for this behaviour can come from the comparison of the modes of fracture under impact loading, shown in Figures 3 and 4. The former highlights that the not fully effective impregnation of manually extracted fibres results in a marked influence of internal defects, such as incorrect fibre orientation, whilst the latter depicts, through the complex pattern of flexural impact damage, the presence of hindrances that limit crack propagation, which may result in the higher stiffness of the laminate. Paddocking and scutching led also to fibres which were more easily impregnated by the polymer resin: an example of flexural frac-

Table 2. Tensile properties of phormium fibres extracted with the two procedures

Fibre tensile properties	Manually extracted	Paddocked and scutched
σ [MPa]	147 ± 30	282 ± 56
E [GPa]	11.5 ± 3.5	10.4 ± 2.8

Table 3. Flexural properties of phormium fibre composites

Fibre tensile properties	Manually extracted	Paddocked and scutched
σ [MPa]	43 ± 2.5	60.5 ± 4.0
E [GPa]	0.8 ± 0.25	4.4 ± 0.2
W_{flex} [kJ]	2.77 ± 0.6	2.67 ± 0.47

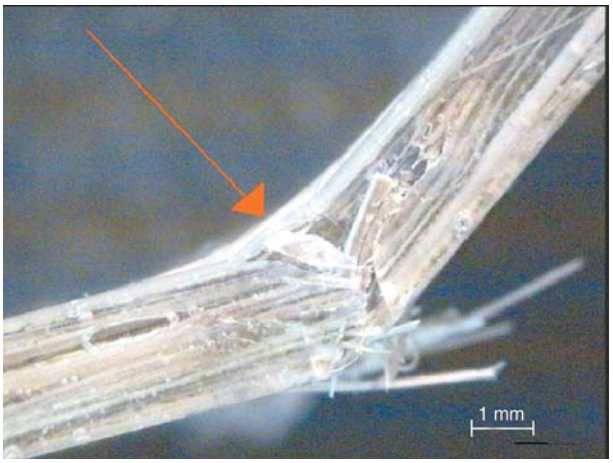

Figure 3. Mode of fracture under impact loading for phormium/epoxy laminates reinforced with manually extracted fibres (centre of the impacted region marked with the red arrow)

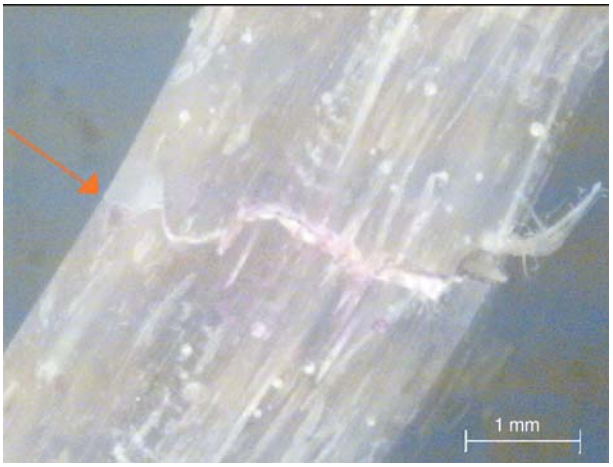

Figure 4. Mode of fracture under impact loading for phormium/epoxy laminates reinforced with paddocked and scutched fibres (centre of the impacted region marked with the red arrow)

ture surface, showing fibres effectively embedded in resin with little pull-out is presented in Figure 5. Both these evidences are confirmed by the study of impact hysteresis cycles, some typical examples of which are reported in Figures 6a and 6b for manually extracted and paddocked and scutched fibres respectively.

The detailed analysis of the data obtained from hysteresis impact cycles show that laminates obtained using paddocked and scutched fibres have globally superior impact properties with respect to the ones manufactured using manually extracted ones. The difference is particularly significant when dealing with linear stiffness, measured by the slope of the elastic part of the curve in N/mm, normalised against the thickness in mm. More moderate increments are also shown from normalised maximum load and deflection. The scattering measured on this value is mainly to be related with the non opti-

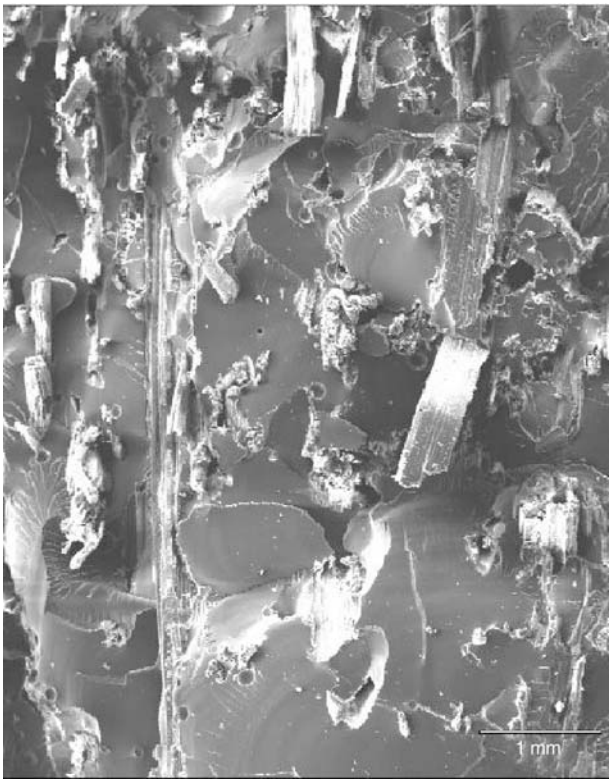

Figure 5. SEM micrograph of composites fracture surface (paddocked and scutched fibres)

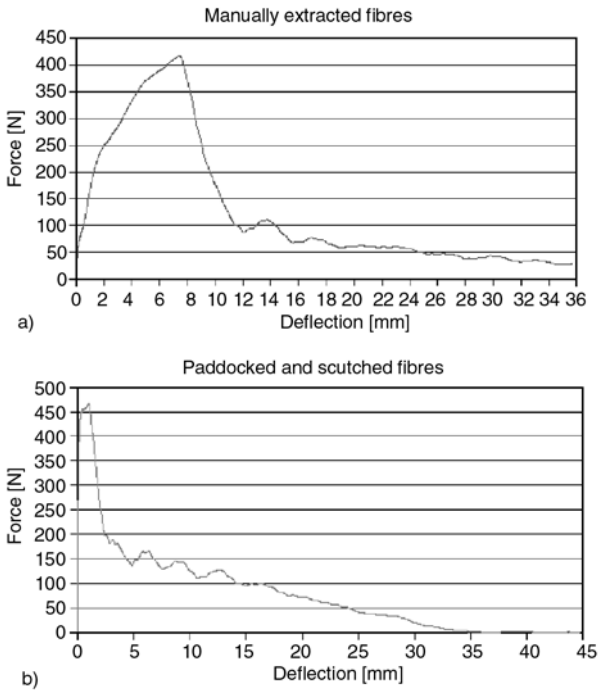

Figure 6. Typical impact hysteresis cycles for two phormium/epoxy laminates (7 mm) impacted at 3.75 Joules and with fibres extracted in different ways

Table 4. Values of variables from impact hysteresis cycles for different laminates (all thickness-sensitive values are normalised)

Properties	Manually extracted	Paddocked and scutched
Max. load/thickness [N/mm]	57.0 ± 7.3	102.4 ± 31.1
Max. deflection/thickness (pure number)	4.2 ± 1.9	6.9 ± 1.1
Normalised linear stiffness [N/(mm/mm)]	313.2 ± 93.5	2002.3 ± 553.0
Damping ratio	1.7 ± 0.9	4.6 ± 2.1
Penetration energy [kJ/m^2]	1.7 ± 0.5	3.1 ± 0.6

Table 5. Comparative values of normalised linear stiffness [N/(mm/mm] and penetration energy [kJ/m^2] for different plant fibre reinforced laminates

Laminate	Avg. normalised linear stiffness [N/(mm/mm)]	Avg. penetration energy [kJ/m^2]	Fibre volume [wt%]
Phormium/epoxy (manually extracted fibres)	313	1.7	16
Phormium/epoxy (paddocked and scutched fibres)	2002	3.1	16
Jute/polyester [16]	1462	27.0	50
Hemp/epoxy (unidirectional loose fibres) [14]	1023	70.0	50
Hemp/epoxy (cross-ply loose fibres) [14]	2279	72.0	53
Hemp/epoxy (non-woven mat fibres) [14]	1984	77.5	45
Flax/epoxy (0.2 mm. thread) [9]	1134	53.3	31
Flax/epoxy (0.9 mm. thread) [9]	1628	59.3	53
Flax/epoxy (2.3 mm. thread) [9]	1155	51.7	50

mal alignment of fibres and also to the limited total volume of reinforcement, which results in the presence of resin-rich areas (Table 4). In any case, the average value of normalised linear stiffness obtained when using paddocked and scutched fibres is comparable with values measured already on other laminates, although reinforced with a much larger volume of fibres, as reported in Table 5.

Damping ratio has been defined, along the lines of what done already in [13–15], as the ratio between the non-elastic energy (A2+A3) and the hysteresis energy before damping (or rebound) (A1+A2): an example of this measurement is reported for example in Figure 7 for paddocked and scutched fibres laminates. Paddocking and scutching phormium fibres results in the production of laminates which are able to dissipate much more energy (actually, more that twice as much) in the damping phase of the impact event. This very high value of damping ratio appears to be an interesting characteristic of phormium fibres, whenever their diameter is not very scattered, as a result of effective extraction, and in any case much higher than the values measured in [15] on jute, flax and abaca. It is noteworthy, however, that, whatever the fibre extraction method adopted, laminate penetration energy remains quite low, and by no means comparable with other plant fibre reinforced laminates, it is in this respect that the detrimental effect of the low fibre volume introduced is particularly evident (Table 5). It is suggested that phormium fibres may have some interest as reinforcement in impact-resistant composites only in much larger volumes and possibly different configurations, in laminates with thickness exceeding few mm (possibly above 10 mm or so) or in hybrids including also layers of fibreglass.

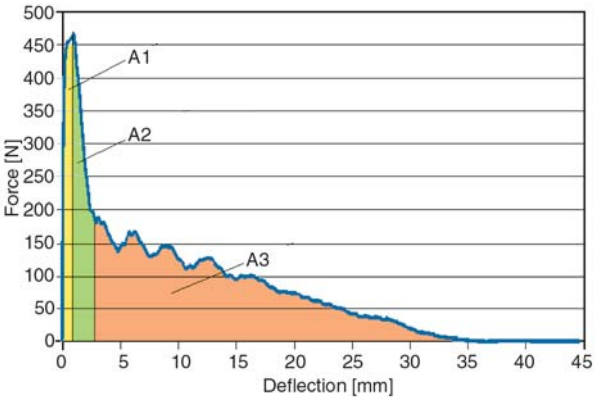

Figure 7. Example of measurement of damping ratio from impact hysteresis curves as (A2+A3)/(A1+A2)

In general, the results indicate the importance of the extraction method adopted on the falling weight impact properties of the phormium fibre laminate obtained, especially as regards its damping behaviour during the impact event. This is particularly important in phormium fibres, because of the possibility with effective extraction to reduce the inher-

ently large variability of cross-sectional shapes and dimensions of technical fibres. This is a feature which has been frequently observed in leaf-extracted plant fibres e.g., in henequen [17].

4. Conclusions

Extraction of phormium fibres by decortication (paddocking and scutching), rather than manual extraction from leaves, results in considerably improved flexural properties of the obtained composites. In addition, the amount of energy absorbed during the damping phase of the falling weight impact event is also much larger, suggesting to be result of the improved fibre-matrix interface.

The main limitation of these composites is in the low amount of fibres that can be introduced in the matrix, because of geometrical limitations, in that the scattering in diameters and shapes between the single fibres, albeit reduced by decortication, is still considerably high. This affects particularly impact penetration energies of the resulting laminates, and could possibly be solved by the use of phormium fibres disposed in non-woven mats or fabrics, which are currently under development.

References

[1] Saheb D. N., Jog J. P.: Natural fiber polymer composites: A review. Advances in Polymer Technology, **18**, 351–363 (1999).
DOI: 10.1002/(SICI)1098-2329(199924)18:4<351::AID-ADV6>3.0.CO;2-X

[2] Santulli C.: A biomimetic approach to the production of sustainable structural composites using plant fibres. in 'Biologically inspired textiles' (eds.: Ellison M. S., Abbott A. G.) Woodhead Publishing, Cambridge, 95–114 (2008).

[3] Mishra S., Mohanty A. K., Drzal L. T., Misra M., Hinrichsen G.: A review on pineapple leaf fibers, sisal fibers and their biocomposites. Macromolecular Materials and Engineering, **289**, 955–974 (2004).
DOI: 10.1002/mame.200400132

[4] Cruthers N. M., Carr D. J., Laing R. M., Niven B. E.: Structural differences among fibers from six cultivars of harakeke (*Phormium tenax*, New Zealand flax). Textile Research Journal, **76**, 601–606 (2006).
DOI: 10.1177/0040517506065603

[5] Le Guen M., Newman R.: Pulped *Phormium tenax* leaf fibres as reinforcement for epoxy composites. Composites Part A: Applied Science and Manufacturing, **38**, 2109–2115 (2007).
DOI: 10.1016/j.compositesa.2007.07.001

[6] Lewin M.: Handbook of fiber chemistry. Taylor and Francis, London (2006).

[7] Rodríguez E., Petrucci R., Puglia D., Kenny J. M., Vázquez A.: Characterization of composites based on natural and glass fibers obtained by vacuum infusion. Journal of Composite Materials, **39**, 265–282 (2005).
DOI: 10.1177/0021998305046450

[8] Santulli C., Janssen M., Jeronimidis G.: Partial replacement of E-glass fibres with flax fibres in composites and effect on falling weight impact performance. Journal of Materials Science, **40**, 3581–3585 (2005).
DOI: 10.1007/s10853-005-2882-y

[9] Santulli C.: Falling weight impact damage characterisation on flax/epoxy laminates. International Journal of Materials and Product Technology, **36**, 221–228 (2009).
DOI: 10.1504/IJMPT.2009.027833

[10] Santulli C., Caruso A. P.: A comparative study on falling weight impact properties of jute/epoxy and hemp/epoxy laminates. Malaysian Polymer Journal, **4**, 19–29 (2009).

[11] Newman R., Clauss E., Carpenter J., Thumm A.: Epoxy composites reinforced with deacetylated phormium tenax leaf fibres. Composites Part A: Applied Science and Manufacturing, **38**, 2164–2170 (2007).
DOI: 10.1016/j.compositesa.2007.06.007

[12] Sutcliffe M. P. F., Fleck N. A.: Microbuckle propagation in fibre composites. Acta Materialia, **45**, 921–932 (1997).
DOI: 10.1016/1359-6454(95)00410-6

[13] Karger-Kocsis J., Benevolenski O. I., Moskala E. J.: Towards understanding the stress oscillation phenomenon in polymers due to tensile impact loading. Journal of Materials Science, **36**, 3365–3371 (2001).
DOI: 10.1023/A:1017935323058

[14] Santulli C., Caruso A. P.: Effect of fibre architecture on the falling weight impact properties of hemp/epoxy composites. Journal of Biobased Materials and Bioproducts, (in press) (2009).

[15] Bledzki A. K., Mamun A. A., Faruk O.: Abaca fibre reinforced PP composites and comparison with jute and flax fibre PP composites. Express Polymer Letters, **1**, 755–762 (2007).
DOI: 10.3144/expresspolymlett.2007.104

[16] Santulli C.: Mechanical and impact properties of untreated jute fabric reinforced polyester laminates compared with different E-glass fibre reinforced laminates. Science and Engineering of Composite Materials, **9**, 177–188 (2000).

[17] Cazaurang-Martinez M. N., Herrera-Franco P. J., Gonzalez-Chi P. I., Aguilar-Vega M.: Physical and mechanical properties of henequen fibers. Journal of Applied Polymer Science, **43**, 749–756 (1991).
DOI: 10.1002/app.1991.070430412

eXPRESS Polymer Letters Vol.3, No.10 (2009) 657–664
Available online at www.expresspolymlett.com
DOI: 10.3144/expresspolymlett.2009.82

Thermomechanical properties of the silanized-kenaf/ polystyrene composites

*Y. Xu, S. Kawata, K. Hosoi, T. Kawai, S. Kuroda**

Department of Production Science and Technology, Graduate School of Engineering, Gunma University, 29-1 hon-cyo, Ota, Gunma 373-0057, Japan

Received 12 June 2009; accepted in revised form 11 August 2009

Abstract. In order to improve the poor interfacial adhesion of the kenaf fiber and polystyrene (PS) in their composite material, the surface of the kenaf fiber was modified using a synthesized polymeric coupling agent to promote adhesion with PS matrix. The dynamic thermo-mechanical properties of the composite composed of modified kenaf fiber and PS were also investigated. The polymeric coupling agent treatment of the kenaf fiber increased the fiber-matrix interaction through a condensation reaction between alkoxysilane and hydroxyl groups of kenaf cellulose. DMA (Dynamic Mechanical Thermal Analysis) results showed that the modified fiber composites have higher E' and lower tanδ than those with untreated fiber indicating that a greater interfacial interaction between the matrix resin and the fiber. It was also found that the storage modulus increases in proportion with the Si/C ratio on the fiber surface.

Keywords: *polymer composites, kenaf fiber, polymeric coupling agent, dynamic mechanical properties, interfacial interaction*

1. Introduction

Biodegradable or environmentally acceptable materials have attained increasing interest over the past decades due to environmental pressure derived from the consumption of the petroleum-based materials [1–3]. The use of natural fibers, derived from annually renewable resources, as reinforcing fibers in both thermoplastic and thermoset matrix composites provides positive environmental benefits with respect to ultimate disposability and raw material utilization. Other benefits are also seen as the natural fibers absorb nitrogen and phosphorus included in the soil [4–7].

Kenaf, *Hibiscus cannabinus, L. family Malvaceae*, is an herbaceous annual plant that can be grown under a wide range of weather condition, especially in Asia and Central America and finds application as a cordage and sack fiber. The excellent cellulose in the kenaf fiber (KF) source also made the kenaf as a source for a large range of paper products. Recently, researches have further increased the diversity of uses for kenaf by demonstrating its suitability in building materials, textiles, adsorbents, and fibers in new and recycled plastics [8].

KF shows low density, high impact resistance, and high modulus. In addition, KF is available in large amounts, easy to get, low cost, non-abrasive during processing, it exhibits high specific mechanical properties and biodegradability [9–13]. However the hydrophilicity of natural fibers results in high moisture absorption and weak adhesion to hydrophobic matrix resin. And there also have been other challenges presented by natural fibers such as large variability of mechanical properties, low ultimate strength, lower elongation, problems with nozzle flow in injection molding machines, bubbles

*Corresponding author, e-mail: skuroda@gunma-u.ac.jp

in the product, and poor resistance to weathering [14–18]. To increase the interaction between the fibers and the resin is the way to tackle with the low adhesion. Normally, there are two ways to treat KF to make it compatible with resin matrix: one is alkaline treatment, by using an alkaline solution, which can dissolve unwanted microscopic pits on the fibers resulting in better fiber matrix adhesion. The other way is using coupling agent. The coupling agent has two functions: to react with –OH groups of the cellulose and to react with the functional groups of the matrix with the goal of facilitating stress transfer between the fibers and the matrix. The commonly used coupling agent includes maleic andydride, silane coupling agent, etc [19–22]. The effect of the coupling agent was only concluded form the phenomenon of the improvement of the mechanical properties of the composite. Little research is available for the quantitative effect of the coupling agent on the mechanical properties [23–25]. Recently we have synthesized a novel coupling agent composed of methacryloxypropyltriethoxysilane by means of photo-graft polymerization. In this paper, the effect of the coupling agent is studied through quantitative analysis of the reactivity of KF with coupling agent.

2. Experiments

2.1. Material

Kenaf fiber (KF) used in this experiment was harvested in Henan Province, China. The fiber was cut into 2–5 mm length, and was washed by running water and then dried up in oven at 80°C until constant weight.

A commercial-grade polystyrene (PSJ433, MFI = 21.0 g/10 min at 230°C/2.16 kg, E' = 0.8 GPa, ρ = 1.0304 g/cm^3, ν = 0.33, PS Japan) was selected as polymer matrix.

The polymeric coupling agent (CA) was synthesized in our lab. Figure 1 shows the structure of CA used in this study.

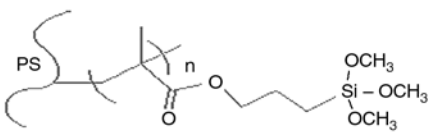

Figure 1. Structure of the coupling agent

2.2. Production of Coupling Agent (CA)

PS powder was supplied from Toyo Styrene Co, Ltd. The powder size is around 200 μm.

3-methacryloxypropyltriethoxysilane (MAPTMS) from Shin-Etsu Silicones was used as grafting monomer and used as received.

Xanthone was used as photo-initiator. Toluene and methanol were used as solvent.

Xanthone was dissolved in methanol/toluene mixture solvent to prepare initiator solution. The solvent and monomer were put into the reactor to form a solution, and then PS powder was put into the reactor. The reactor was bubbled with nitrogen for 1 h.

The reactors containing monomer, initiator, polymer matrix and solvent was then heated to 60°C, and irradiated with a 400 W high pressure Hg lamp (Riko, UVL-400H, Riko Kagaku, Japan) for 4 h.

After the photo-graft polymerization, the PS powder was washed with methanol in a Soxhlet extractor for 24 h and then dried at room temperature in a vacuum oven for 48 h.

The grafting of MAPTMS onto PS powder was confirmed by the FT-IR spectra recorded on JASCO FT/IR-8000 and the grafting yield (GY) was evaluated by Equation (1):

$$Grafting\ yield\ [\%] = \left(\frac{W_1 - W_0}{W_0}\right) 100 \qquad (1)$$

where, W_1 is the weight PS powder after grafting and W_0 is the weight of the original weight of PS powder.

2.3. Reaction of CA with KF in THF solvent

First, KF was washed in THF solvent at 70°C for 1 h to remove impurities. And then the CA was dissolved in THF at different concentration to react with KF at 70°C for 1 h. The modified KF was filtered and then dried in a vacuum oven until constant weight.

2.4. Preparation of composites using a kneader

PS/KF/CA composites were prepared using a kneader (Labo Plastomill 4C, Toyoseiki, Japan). The PS and the KF reacted with CA were weighted as 50 to 50. To prepare the composites, the mixing

Table 1 Composition of the samples

Sample code	PS [weight ratio]	KF [weight ratio]
PSJ433	100	0
C0	50	50 (THF-washed)
C1	50	50 (reacted with 5 wt% CA)
C2	50	50 (reacted with 10 wt% CA)
C3	50	50 (reacted with 15 wt% CA)

temperature was set at 195°C. PS was first added into the kneader at 22 rpm and after the PS was melted, the reacted KF was mixed with the molten PS for 10 min at 30 rpm. After blending, the compound was hot-pressed at 30 MPa for 5 min, and then moved to cooling press until the temperature of the compound was cooled down to room temperature under a pressure of 25 MPa. The composition of the samples prepared is listed in Table 1 with their code.

2.5. Recovery of KF from composites

The PS/KF/CA composites were dissolved in THF solvent for 5 h at room temperature, and then the solution was filtered to recover the kneaded KF fiber. The recovered KF was then washed with THF at least twice to clean the fiber surface, and dried in a vacuum oven until constant weight. The diameter, the length and the surface composition of the KF fiber before and after kneading were analyzed by digital microscope, scanning electron microscope (SEM) and energy dispersive X-ray spectrometer (SEM-EDX).

2.6. Measurements

The FTIR spectra of the coupling agent was recorded on Fourier-transform IR spectrophotometer (JASCO FT/IR – 8000). Samples were mixed with analytical grade KBr and compressed into disk and the spectra were recorded with a 2 cm^{-1} resolution and 32 scans.

The fiber diameter before and after kneading was detected by digital microscope VHX-600 (Keyence, Japan). A maximum of 200 magnifications were tested for each sample.

The density of the KF was detected by a density analytical balance AUW120D (Shimadzu corporation, Japan) with using 2-propanol for the liquid medium.

Samples were studied by dynamic mechanical analysis (DMA) using tensile mode with Rheolograph Solid S-1 (Toyoseiki, Japan). The measurements were carried out at temperature range from 30 to 150°C at a heating rate of 2°C/min. The test frequency was 10 Hz and the sample size was 20 mm × 5 mm × 1.5 mm. The storage modulus, loss modulus and tanδ of the samples were recorded during the running.

Scanning electron microscope and energy dispersive X-ray spectrometer (SEM-EDX) (S-3000N, Hitachi; EX-200K Horiba) was used to measure the element of the surface on the KF, the recovered KF and the KF reacted with CA in THF solvent. The measurements were carried out at 15 kV and the analysis depth is about 1 μm.

3. Results and discussion

3.1. Characterization of CA

Figure 2 is a typical FTIR spectrum of CA. The strong peak appeared at 1089, 1602 and 1729 cm^{-1} which correspond to the absorption of Si–O–C, benzene ring and carbonyl group, respectively. The grafting yield was calculated using Equation (1) and the estimated GY for the present CA was 5.8%, which was found to be consistent with the values estimated by Nuclear Magnetic Resonance (NMR) and FT-IR measurements as reported elsewhere [26].

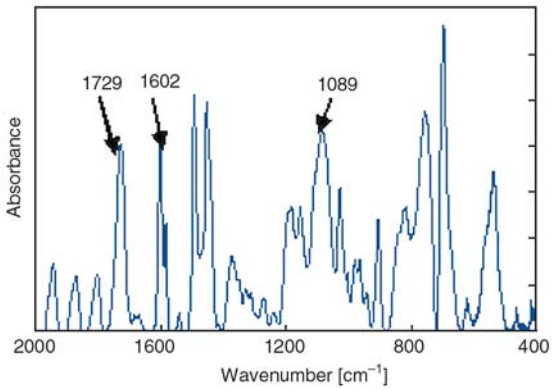

Figure 2. Typical FT-IR spectrum of the coupling agent

3.2. Surface elements analysis of the kenaf fiber

The surface of the KF was modified using the synthesized polymeric coupling agent in THF solution to promote the adhesion with the PS matrix. The

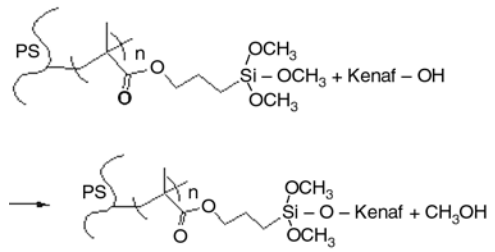

Figure 3. Possible reaction mechanism of the coupling agent with kenaf fiber

main component of KF is cellulose of which hydroxyl group is to be reacted with CA in the following mechanism shown in Figure 3.

The reaction of coupling agent with KF is the ester-exchange reaction between the alkoxysilane groups (Si–OR) and hydroxyl groups of KF, which results in the KF surface covered with the hydrophobic PS chain of the CA that can entangle with PS matrix to enhance the interfacial adhesion between KF and PS matrix.

The KF fibers before and after kneading were shown in Figure 4. The KF fiber diameter before kneading is around 50–120 μm. After kneading, the diameter of the KF fiber was kept around 50–100 μm. It shows that the diameter of the KF fiber did not change during kneading but the fiber length decreased down to c.a. 400–500 μm.

Si/C ratio of the KF recovered from the composites and the KF reacted with CA are shown in Figure 5. It can be seen along with the increasing of the CA weight fraction, the Si/C ratio of the reacted KF is increased obviously. After the CA weight fraction reached 10 wt%, the Si/C ratio achieves saturation and it is not increased any more.

The Si/C ratio of the recovered KF is lower than the modified KF fiber, which indicates that the silicon combined with KF has been removed during kneading. It should be noted that the recovered KF had reduced length of c.a. 400–500 μm while the diameter did not change indicating some breakage occurred during the process.

However, the KF reacted in 15% CA solution seems to form more chemical bonds with a CA molecular chain than that reacted in 10% solution even though the number of CA molecule attached to a KF are similar to each other so that the CA molecule remains on KF when the neighbor fiber surface is peeled.

CA has a PS main chain, which could entangle with a matrix PS molecular chain as well as set up van

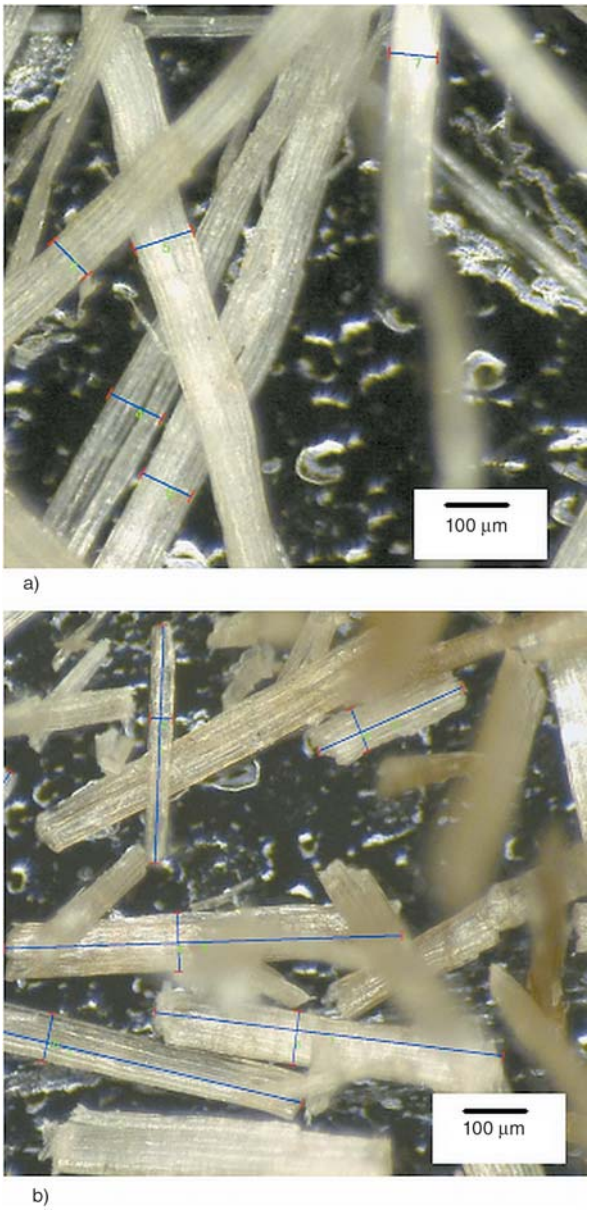

Figure 4. KF fiber diameter before kneading (a) and after kneading (b)

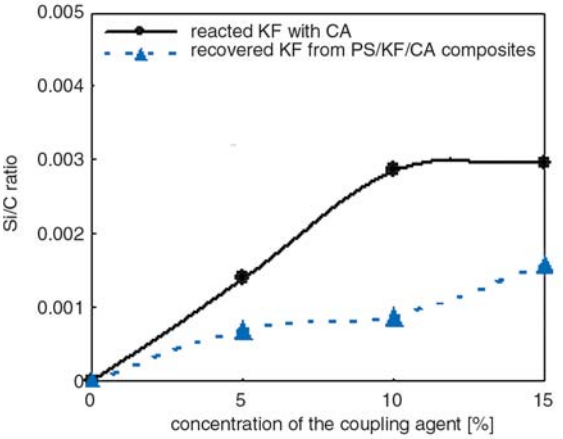

Figure 5. The Si/C ratio of the recovered KF from the composites and the reacted KF analyzed by SEM-EDX

der Waals interaction with the PS matrix due to their similar chemical structures. Although van der Waals interaction is not as strong as other primary bonds, it could still improve the adhesion properties between hydrophilic KF and the hydrophobic PS matrix.

3.3. Morphology of the KF

Scanning electron microscopy provides an excellent technique for examination of surface morphology of fibers and fracture surfaces of the fiber composites. Examinations were carried out on the unwashed fiber and THF washed fiber.

The SEM micrograph of the longitudinal surface of unwashed KF bundles in Figure 6a shows the presence of wax, oil and surface impurities. The existence of these materials will decrease the mechanical properties of the fiber composites. Figure 6b shows the surface of the KF bundles washed with THF. It seems that the impurity has been removed without roughing the surface of fiber bundles.

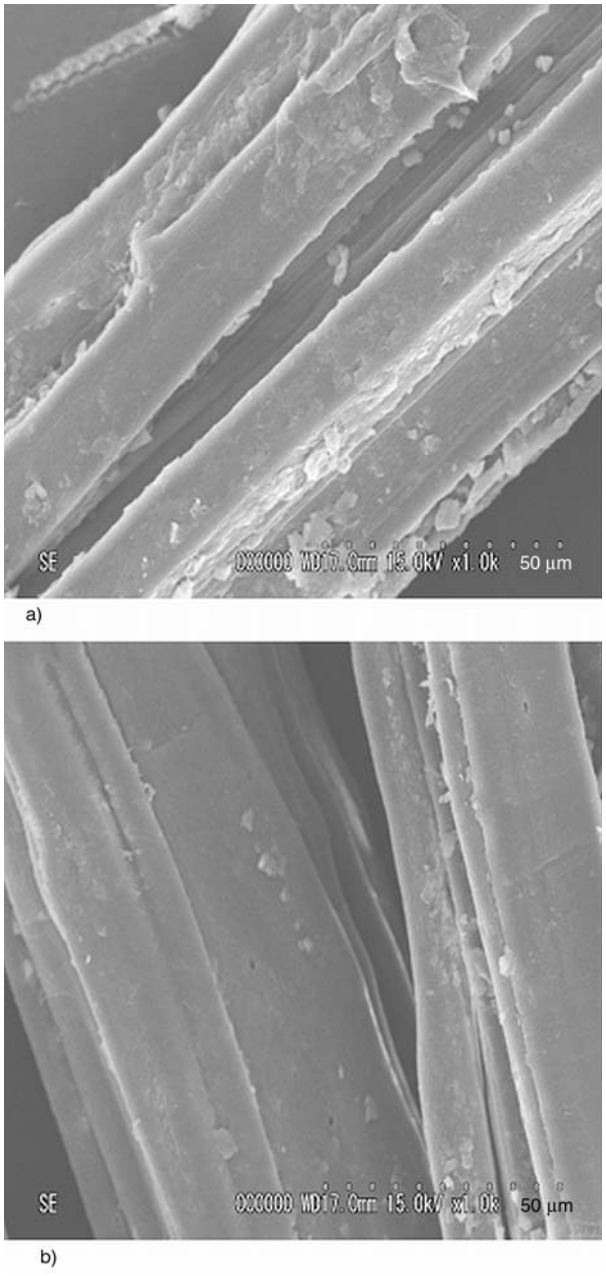

Figure 6. SEM micrographs of longitudinal views of (a) unwashed KF and (b) THF washed KF

3.4. Mechanical properties of composites

Dynamic mechanical thermal analysis was carried out on the different types of composites prepared. Storage modulus values of the PS, PS/KF/CA composites are compared in Figure 7.

The storage modulus is useful in assessing the molecular basis of the mechanical properties of a material because it is very sensitive to structural changes, such as fiber-matrix interfacial bonding. Figure 7 shows the storage modulus of neat PS, PS/KF/CA composites with 50 wt% fiber treated in different concentration of CA solution. The storage modulus improved significantly with the addition of KF to PS over the whole range of the testing temperatures as a result of the reinforcement imparted by the fiber. A much enhanced storage modulus of the composites are obtained for the PS/KF/CA composites compared with the un-treated C0 composite which suggests that the adhesion between PS and un-treated KF is very poor as observed in other Polyolefin/KF composites [27] and the surface modification of KF with CA

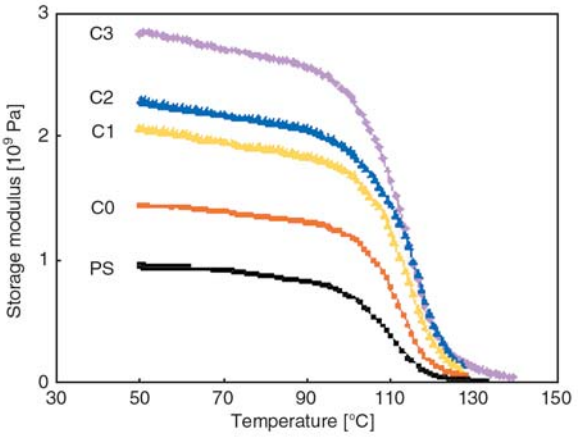

Figure 7. Variation of storage modulus of non-reacted and reacted KF/PS composites as a function of temperature

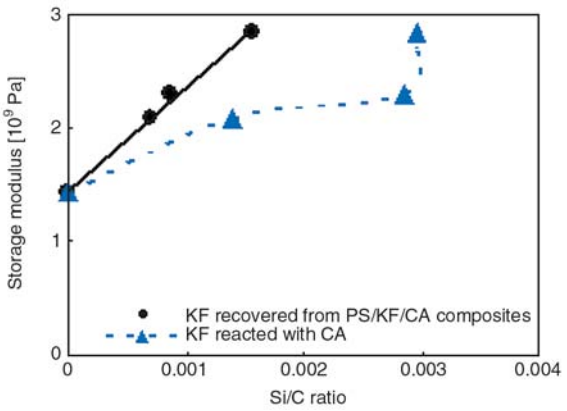

Figure 8. Variation of storage modulus of the PS/KF/CA composites at 50 °C as a function of Si/C ratio

improves the adhesion strength. With the increasing of the CA content on KF, the storage modulus becomes larger.

Figure 8 shows the variation of storage modulus of the PS/KF/CA composites at 50°C as a function of Si/C ratio observed on KF. The storage modulus of the composites increases with the Si/C ratio, which strongly proved that the modification of fiber with CA contributes to the improvement of interfacial adhesion of KF and PS matrix. It should be noted here that the storage modulus is in proportion to the Si/C of recovered KF but not with the reacted KF. As mentioned previously, a part of CA attached to KF by solution reaction is removed during molding. The observed Si/C ratio seems to represent the amount of CA found on KF accurately and to be in accordance with the interaction strength between KF and PS matrix. According to the modified Kerner equation for the composite with randomly dispersed fibrous filler [28] and using the measured values, the Young's modulus of the present composite (E) is estimated from Equation (2):

$$\frac{E}{E_{PS}} = \frac{1 + A \cdot B \cdot \phi_{KF}}{1 - B \cdot \psi \cdot \phi_{KF}} \tag{2}$$

where E is the estimated modulus of the composites, E_{PS} is the modulus of the PS, ϕ_{KF} is the volume fraction of KF. B and ψ are given Equations (3) and (4):

$$B = \frac{\frac{E_{KF}}{E_{PS}} - 1}{\frac{E_{KF}}{E_{PS}} + A} \tag{3}$$

$$\psi \approx 1 + \left(\frac{1 - \phi_m}{\phi_m^2} \right) \cdot \phi_{KF} \tag{4}$$

where E_{KF} is the modulus of the KF. ϕ_m is the maximum volume of the KF. With the random filling of the KF, the ϕ_m is 0.8.

With the random filling of the KF, A is determined by the ratio of KF length (L) and diameter (D). In the present study, the L/D is 4 leading to A is 2.08 [29].

Young's modulus of KF has been estimated as 38 GPa [30] and KF density was measured as 1.3824 g/cm^3, respectively.

The value observed for C3 sample in this present study, 2.86 GPa, is about 84% of the theoretically predicted value, c.a. 3.39 GPa, which indicates CA with graft yield of 5.8 % functioned successfully in the PS/KF composites.

The value of the tanδ, the ratio of viscous to elastic properties, of PS/KF/CA composites with 50 wt% fiber are shown in Figure 9 as a function of temperature. It is obvious that the composites are elastic material with tanδ close to zero at low temperature below 90°C. Beyond 90°C, they become viscous owing to their PS component but there is not a big difference in height of tanδ peak among the untreated-fiber composite C0 and reacted-fiber composites C1-C3 indicating the same order of damping capabilities. The slight reduction in tanδ for the reacted-fiber composites means that the mobility of PS molecules is restricted due to the stronger interfacial interaction between KF and PS than that for untreated-fiber composite. Furthermore, the decrease in mechanical loss factor is also denotes an improvement of fatigue property.

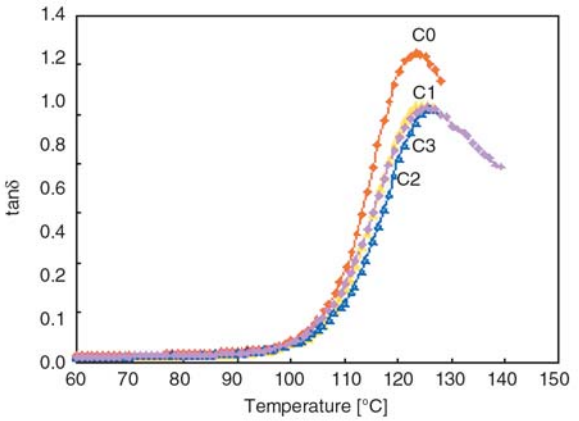

Figure 9. Variation of tanδ of untreated and reacted-fiber PS/KF/CA composites with fiber as a function of temperature

4. Conclusions

In this paper, the surface of the KF was modified using a synthesized polymeric coupling agent to promote adhesion with a PS matrix, and the dynamic mechanical thermal analysis of the modified KF on the PS composites was investigated. CA treatment of the KF increased the fiber-matrix interaction through an ester-exchange reaction between alkoxysilane and hydroxyl groups of kenaf cellulose. DMA showed that modified fiber composites have higher E' and lower tanδ indicating a greater interfacial bond strength and adhesion between the matrix resin and the fiber. After kneading, the KF kept the same diameter, but shortened the fiber length and decreased the Si/C ratio. The storage modulus increased steadily with the increase of the Si/C ratio on KF surface after kneading. A good consistency between the high Si concentrations on KF with the high mechanical properties of the composites was proved.

Acknowledgements

This study was supported by TOHO INDUSTRIAL CO.,LTD as a part of the project 'Development of Creative Technology Seeds – Contract Development' promoted by Japan Science and Technology Agency.

References

[1] Hong C. K., Hwang I., Kim N., Park D. H., Hwang C. B. S., Nah C.: Mechanical properties of silanized jute-polypropylene composites. Journal of Industrial and Engineering Chemistry, **14**, 71–76 (2008). DOI: 10.1016/j.jiec.2007.07.002

[2] O'Donnell A., Dweib M. A., Wool R. P.: Natural fiber composites with plant oil-based resin. Composites Science and Technology, **64**, 1135–1145 (2004). DOI: 10.1016/j.compscitech.2003.09.024

[3] Dweib M. A., Hu B., O'Donnell A., Shenton H. W., Wool R. P.: All nature composites sandwich beams for structural applications. Composite Structures, **63**, 147–157 (2004). DOI: 10.1016/S0263-8223(03)00143-0

[4] Munikenche Gowda T., Naidu A. C. B., Rajput Chhaya: Some mechanical properties of untreated jute fabric-reinforced polyester composites. Composites Part A: Applied Science and Manufacturing, **30**, 277–284 (1999). DOI: 10.1016/S1359-835X(98)00157-2

[5] Nishino T., Hirao K., Kotera M.: X-ray diffraction studies on stress transfer of kenaf reinforced poly (L-lactic acid) composites. Composites Part A: Applied Science and Manufacturing, **37**, 2269–2273 (2006). DOI: 10.1016/j.compositesa.2006.01.026

[6] Shibata S., Cao Y., Fukumoto I.: Lightweight laminate composites made from kenaf and polypropylene fibres. Polymer Testing, **25**, 142–148 (2006). DOI: 10.1016/j.polymertesting.2005.11.007

[7] Amaducci S., Amaducci M. T., Benati R., Venturi G.: Crop yield and quality parameters of four annual fiber crops in north of Italy. Industrial Crops and Products, **11**, 179–186 (2000). DOI: 10.1016/S0926-6690(99)00063-1

[8] Nishino T., Hirao K., Kotera M., Nakamae K., Inagaki H.: Kenaf reinforced biodegradable composite. Composites Science and Technology, **63**, 1281–1286 (2003). DOI: 10.1016/S0266-3538(03)00099-X

[9] Ray D., Sarkar B., Das S., Rana A.: Dynamic mechanical and thermal analysis of vinylester-resin-matrix composites reinforced with untreated and alkali-treated jute fibres. Composites Science and Technology, **62**, 911–917 (2002). DOI: 10.1016/S0266-3538(02)00005-2

[10] Sydenstricker T. H. D., Sandro M., Sandro C. A.: Pull-out and other evaluations in sisal-reinforced polyester biocomposites. Polymer Testing, **22**, 375–380 (2003). DOI: 10.1016/S0142-9418(02)00116-2

[11] Eichhorn S. J., Baillie C. A., Zafeiropoulos N., Mwaikambo L. Y., Ansell M. P., Dufresne A., Entwistle K. M., Herrera-Franco P. J., Escamilla G. C., Groom L., Hughes M., Hill C., Rials T. G., Wild P. M.: Review current international research into cellulosic fibres and composites. Journal of Materials Science, **36**, 2107–2131 (2001). DOI: 10.1023/A:1017512029696

[12] Sgriccia N., Hawley M. C.: Thermal, morphological, and electrical characterization of microwave processed natural fiber composites. Composites Science and Technology, **67**, 1986–1991 (2007). DOI: 10.1016/j.compscitech.2006.07.031

[13] Wambua P., Ivens J., Verpoest I.: Natural fibres: Can they replace glass in fibre reinforced plastics? Composites Science and Technology, **63**, 1259–1264 (2003). DOI: 10.1016/S0266-3538(03)00096-4

[14] Toiz G., Denes F., Young R.: Lignin-polypropylene composites. Part 1: Composites from unmodified lignin and polypropylene. Polymer Composites, **23**, 806–813 (2002). DOI: 10.1002/pc.10478

[15] Fung K. L., Xing X. S., Li R. K. Y., Tjong S. C., Mai Y-W.: An investigation on the processing of sisal fibre reinforced polypropylene composites. Composites Science and Technology, **63**, 1255–1258 (2003). DOI: 10.1016/S0266-3538(03)00095-2

[16] Rezaur Rahman Md., Monimul Huque Md., Nazrul Islam Md., Mahbub Hasan: Mechanical properties of polypropylene composites reinforced with chemically treated abaca. Composites Part A: Applied Science and Manufacturing, **40**, 511–517 (2009)
DOI: 10.1016/j.compositesa.2009.01.013

[17] Riccieri J., Vazguez A., de Carvalho L. H.: Interfacial properties and initial step of the water sorption in unidirectional unsaturated polyester/vegetable fibre composites. Polymer Composites, **20**, 29–37 (1999).
DOI: 10.1002/pc.10332

[18] Gauthier R., Joly C., Coupas A., Gaultier H., Escoubes M.: Interfaces in polyolefin/cellulosic fibre composites: Chemical coupling, morphology, correlation with adhesion and aging in moisture. Polymer Composites, **19**, 287–300 (1998).
DOI: 10.1002/pc.10102

[19] Gassan J., Bledzki A. K.: Effect of cyclic moisture absorption desorption on the mechanical properties of silanized jute-epoxy composites. Polymer Composites, **20**, 604–611 (1999).
DOI: 10.1002/pc.10383

[20] Dash B. N., Rana A. K., Mishra H. K., Nayak S. K., Mishra S. C., Tripathy S. S.: Novel, low-cost jute-polyester composites. Part 1: Processing, mechanical properties, and SEM analysis. Polymer Composites, **20**, 62–71 (1999).
DOI: 10.1002/pc.10335

[21] Feng D., Caulfield D. F., Sanadi A. R.: Effect of compatibilizer on the structure-property relationships of kenaf-fiber/polypropylene composites. Polymer Composites, **22**, 506–517 (2001).
DOI: 10.1002/pc.10555

[22] Keener T. J., Stuart R. K., Brown T. K.: Maleated coupling agents for natural fibre composites. Composites Part A: Applied Science and Manufacturing, **35**, 357–367 (2004).
DOI: 10.1016/j.compositesa.2003.09.014

[23] Aziz S. H., Ansell P. M., Clarke S. J., Panteny S. R.: Modified polyester resins for natural fibre composites. Composites Science and Technology, **65**, 525–535 (2005).
DOI: 10.1016/j.compscitech.2004.08.005

[24] Shibata S., Cao Y., Fukumoto I.: Press forming of short natural fiber-reinforced biodegradable resin: Effects of fiber volume and length on flexural properties. Polymer Testing, **24**, 1005–1011 (2005).
DOI: 10.1016/j.polymertesting.2005.07.012

[25] Arbelaiz A., Fernández B., Ramos J. A., Retegi A., Llano-Ponte R., Mondragon I.: Mechanical properties of short flax fibre bundle/polypropylene composites: Influence of matrix/fibre modification, fibre content, water uptake and recycling. Composites Science and Technology, **65**, 1582–1592 (2005).
DOI: 10.1016/j.compscitech.2005.01.008

[26] Xu Y., Kawata S., Hosoi K., Kawai T., Kubota H., Kuroda S.: Preparation of polymeric coupling agent by means of photo-graft polymerization onto PS microspheres. Journal of Applied Polymer Science, in press (2009).

[27] Sanadi A. R., Caulfield D. F., Jacobson R. E., Rowell R. M.: Renewable agricultural fibers as reinforcing fillers in plastics: Mechanical properties of kenaf fiber-polypropylene composites. Industrial and Engineering Chemistry Research, **34**, 1889–1896 (1995).
DOI: 10.1021/ie00044a041

[28] Lewis T. B., Nielsen L. E.: Dynamic mechanical properties of particulate-filled composites. Journal of Applied Polymer Science, **14**, 1449–1471 (1970).
DOI: 10.1002/app.1970.070140604

[29] Nielsen L. E.: Mechanical properties of polymers and composites. Marcel Dekker, New York (1976).

[30] Ochi S.: Mechanical properties of kenaf fibers and kenaf/PLA composites. Mechanics of Materials, **40**, 446–452 (2008).
DOI: 10.1016/j.mechmat.2007.10.006

eXPRESS Polymer Letters Vol.3, No.10 (2009) 665–675
Available online at www.expresspolymlett.com
DOI: 10.3144/expresspolymlett.2009.83

Molecular dynamics simulation on glass transition temperature of isomeric polyimide

*M. Li, X. Y. Liu, J. Q. Qin, Y. Gu**

State Key Laboratory of Polymer Material and Engineering, College of Polymer Science and Engineering, Sichuan University, Chengdu 610065, China

Received 5 June 2009; accepted in revised form 12 August 2009

Abstract. It is an abnormal phenomenon that glass transition temperature (T_g) of isomeric polyimide (PI) is higher than its corresponding symmetrical PI. To illustrate this phenomenon at the molecular scale, we applied molecular dynamics method to predict the T_g of PI, which were prepared based on 4,4'-oxydianiline (ODA) and 3,3',4,4'-biphenyltetracarboxylic dianhydride (3,3',4,4'-BPDA), and its isomeric system (2,2',3,3'-BPDA-ODA). Simulation result is consistent with experimental value. Non-bond energy plays an important role in glass transition process, for it has an abrupt change near T_g. The higher free volume fraction of isomeric PI can provide the polymer with more space to obtain segmental motion. However, from the torsion angle distribution calculations, it is shown that the torsion angle of its biphenyl group is constrained. Furthermore, from mean square displacement and vector autocorrelation functions calculations, this group is observed to rotate against other groups in the glassy state, and increases the chain rigidity to a great extent. So the isomeric PI needs much more relaxation time for the segment motion. Therefore, the higher T_g of isomeric PI is mainly attributed to the chain rigidity for the time scale, not the free volume for the space scale.

Keywords: *modeling and simulation, isomeric polyimide, molecular dynamics simulation, glass transition temperature*

1. Introduction

Glass transition temperature (T_g) is a key index to evaluate the thermal properties of heat-resistant polymers, such as polyimide (PI), polysulfone, polyether ether ketone. As for polyimide, isomeric PI, which incorporate geometrically asymmetrical unit in dianhydride or diamine structures, can improve the processability and solubility; at the same time, its thermal properties do not show obvious decrease for there is no composition change compared with corresponding symmetrical PI. Unexpectedly, the T_g of isomeric PI is relatively higher than that of symmetrical PI [1]. This interesting phenomenon is not observed with other polymers, such as polyamide [2] and poly(arylene ether ketone) [3, 4]. Several researchers have tried to explain this phenomenon: Tong *et al*. [5] reported that the T_g of symmetrical PI, which was polymerized from 3,3',4,4'-biphenyltetracarboxylic dianhydride (3,3',4,4'-BPDA) and 4,4'-oxydianiline (ODA), was 52 K lower than that of its isomeric system (2,2',3,3'-BPDA-ODA). Furthermore, they analyzed the relative energies of torsion angle for PI monomer, and suggested that the steric hindrance of the adjacent anhydride groups of 2,2',3,3'-BPDA inhibit the segmental motion, and increase the T_g, relative to that of the 3,3',4,4'-BPDA. Kochi *et al*. [6] reported similar results on these two systems, and analyzed the temperature of β relaxation using the dynamic mechanical analysis (DMA) method. Hasegawa *et al*. [7] studied on the isomeric phenomena of PIs, which were prepared

*Corresponding author, e-mail: guyi@scu.edu.cn

based on BPDA and 1,4-phenylene diamine (PDA). Semiempirical method was used to study the conformation of a single PI chain in gas state. They inferred that the higher T_g for the isomeric polyimide is attributed to the asymmetric structure requiring a larger sweep volume for the crank shaft motion and accordingly more energy (higher temperature) to obtain this motion. The above studies facilitate us with the insight into the nature of the higher T_g of isomeric PI, however, there has been no systematic study investigating the effect of isomerism on T_g of polyimides. It is acknowledged that the T_g of polymeric materials is mainly determined by the segment motion of a polymer chain. If this motion can be observed, the polymer chain should have sufficient space (more free volume) and can complete this motion in a short time period (less relaxation time, it mainly depends on rigidity of a polymer chain). Nevertheless, these two factors can not be well discussed in the gas state [5, 7], so it is necessary to find an appropriate method to investigate them in the bulk state.

Yet, molecular dynamics (MD) simulation method provides a proper means to study bulk polymer at molecular scale. Some researchers have applied it to study the glass transition temperature of polymers, such as polyethylene [8], polypropylene [9], polystyrene [9], poly(oxymethylene) [8], polysiloxane [10], polylactic acid [11], epoxy resin [12]. The results indicate a good agreement with experimental value. In the filed of polyimides, Liang *et al.* [13] successfully predict the glass transition temperature of PI with different chromophores using MD method, and they deduced that T_g of PIs are correlated to the height of energy barrier of bridging bonds between aromatic rings. Recently, Yani and Lamm [14] studied on the glass transition temperature of PI/polyhedral oligomeric silsesquioxane (POSS) blends, showing that the simulation results are comparable to experimental observation and incorporation of the appropriate content POSS can improve glass transition temperature. Thus, MD method is an effective method to predict the glass transition temperature of polymers at the molecular scale.

In this study, we firstly applied MD simulation method to study the effect of isomerism on the glass transition temperature of bulk polyimides, using 3,3',4,4'-BPDA-ODA and 2,2',3,3'-BPDA-ODA systems (Figure 1) as model molecules. The

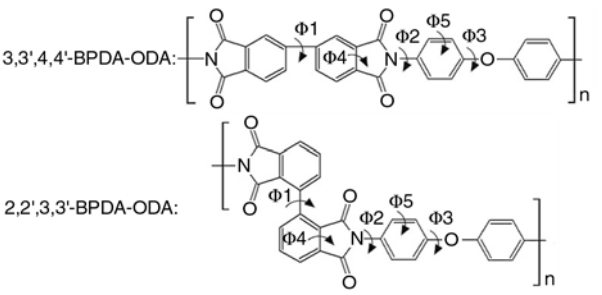

Figure 1. Structures of two polyimides: 3,3',4,4'-BPDA-ODA and 2,2',3,3'-BPDA-ODA

rest of the paper is organized as follows: In section 2, simulation details of MD method are described. Section 3 is result and discussion. We obtained comparative value of T_g in PIs, and analyze the role of energy component in glass transition process. Furthermore, the reason for higher T_g of 2,2',3,3'-BPDA-ODA systems is given by the analysis at time scale (chain rigidity) and space scale (free volume). Finally, we summarize our major results and conclusions in section 4.

2. Simulation details

Simulations were performed using the Materials Studio 4.0 software purchased from Accelrys Inc [15]. The Dreiding force field was used in molecular mechanics (MM) and molecular dynamics simulations [16]. The total potential energy (E_{total}) can be expressed as:

$$E_{total} = E_{bond} + E_{non-bond} = E_b + E_\theta + E_\varphi + E_{inv} + E_{vdW} + E_{elec} \quad (1)$$

Equation (1) is divided into two parts: valence terms (E_{bond}) and non-bond interaction terms ($E_{non-bond}$). The valence terms include E_b, E_θ, E_φ, E_{inv} for bond stretching, angle bending, dihedral torsion and inversion (out-of-plane) terms. The non-bond interaction terms include E_{vdW} and E_{elec} for calculating van der Waals force and electrostatic interactions respectively. The non-bond interactions were calculated in this study with cut-off being set to 0.95 nm, which is less than half of the cell length (during the glass transition process, cell length was kept around 2.2–2.5 nm). The amorphous polymer models were built with the Theodorou and Suter's method [17, 18] using periodic boundary conditions. Each cell consisted of a parent PI chain with 20 repeat units. Though the system size of 20 repeat units is not enough to rep-

resent the conformation of a real polymer chain, previous researchers have reported reasonable result when they used 10–15 repeat units [13, 19]. In addition, previous studies demonstrate that simulated T_g values are comparable with experimental one by simulating a single polymer chain [8–10, 13]. So we can save a lot of computational resource in this way. The cell was first optimized in a low initial density of 0.5 g/cm^3 by smart minimization, which incorporated steepest decent with conjugate gradient methods. Then, relaxation of the cell was performed by MD simulation at 1000 K for 2 ns using an integration step of 1 fs under constant-pressure constant-temperature (NPT) ensemble. The conformation of low potential energy structure was selected and minimized again. In this procedure, density of each PI system was above 0.8 g/cm^3. To make sure a system reached equilibrium, a number of thermodynamic quantities were checked. As a result, they remained stable during the last 500 ps, and it was concluded that the system was equilibrated.

The glass transition temperature of polymeric materials can be determined by plotting specific volume versus temperature with constant-NPT MD simulation and noting where the slope changes [14]. The system was cooled from 750 K stepwise to 400 K by decrements of 50 K. At each temperature, constant-NPT MD simulation was conducted for 1 ns. In the last 100 ps, the cell density was sampled at every picosecond, and the average value was taken as the result.

In addition to the glass transition temperatures, we have also calculated torsion angle distribution, mean square displacement and vector autocorrelation functions of polyimides. The equilibrated configuration in the constant-NPT MD simulation was used as the initial structure, and then was calculated by constant-volume constant-temperature (NVT) MD simulation for 2 ns. Data samples were collected at every picoseconds.

In this study, the pressure of system was set to $1.0 \cdot 10^5$ Pa. Nose thermostat [20, 21] and Berendsen barostat [22] were applied to control temperature and pressure in constant-NPT MD simulation.

3. Results and discussion

3.1. Glass transition temperature

The temperature dependence of the specific volume of two PI systems is shown in Figure 2. With increasing temperature, the increment of specific volume is less pronounced below T_g yielding a kink in the curve to determine T_g. Detailed method has been well described in ref. [11]. According to this method, simulated glass transition temperatures of these two PIs were obtained. The T_g of isomeric PI (2,2',3,3'-BPDA-ODA) is 593 K which is much higher than symmetrical PI's (3,3',4,4'-BPDA-ODA, 548 K). Simulation result is consistent with experimental values shown in Table 1. For comparison, we also applied group contribution method to predict T_g of PIs [13]. This method is based on the contribution of each functional group to thermodynamic properties of polymeric materials, and it has been widely used in alkyl polymers [23, 24]. However, in this study, the T_g values of two PIs are the same using this method for it can not resolve the position effect of the imide group. Therefore, MD simulation is a relatively effective method to predict T_g of isomeric polyimides.

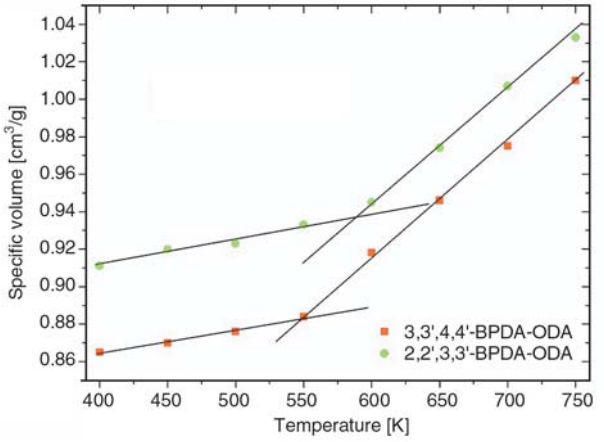

Figure 2. Plots of specific volume of MD simulation versus temperature for two polyimides: 3,3',4,4'-BPDA-ODA (■); 2,2',3,3'-BPDA-ODA (●)

Table 1. Glass transition temperatures of PIs with MD simulation, correlation prediction, and experiment methods

PI systems	Glass transition temperature [K]		
	MD simulation	Correlation prediction[a]	Experiment[b]
3,3',4,4'-BPDA-ODA	548	576	539
2,2',3,3'-BPDA-ODA	593	576	591

[a]Predicted by Synthia module in Materials Studio software package
[b]Experimental value in ref. [5]

Also, we checked the density of PIs at 298 K. The density for 3,3',4,4'-BPDA-ODA system is 1.20 g/cm^3 while the density of 2,2',3,3'-BPDA-ODA system is 1.13 g/cm^3. And the density of 3,3',4,4'-BPDA-ODA system is about 17% smaller than experiment value [25] (density of 2,2',3,3'-BPDA-ODA system has not been reported in existing reference). However, when we want to get the comparable T_g from the MD simulation, the dynamic change of density (or specific volume) near T_g should be emphasized, not the density itself.

3.2. Free volume

According to the Fox and Flory's theory of glass transition, the free volume of the polymer experiences an abrupt change during the cooling down at a point called the glass-transition temperature. In this study, we applied a probe sphere, whose radius is 0.1 nm (distance between neighboring atoms) or 0.3 nm (distance between neighboring molecules), to probe the equilibrated polymer cells to calculate the free volume [8]. Furthermore, the free volume fraction (FVF) can be obtained by Equation (2):

$$FVF = \frac{V_f}{V_f + V_0} \tag{2}$$

where V_f is free volume, and V_0 is occupied volume of the polymer chains.

The plot of FVF of two PIs with a probe sphere of 0.1 nm radius versus temperature is shown in Figure 3, indicating similar T_g with the plot of specific volume versus temperature. However, increasing the radius to 0.3 nm, we can not get the clear T_g by the same method, for it is difficult to determine van der Waals surface with the probe sphere of big radius in this measurement. During the glass transition process, free volume determines how much space can be provided for the segment motion of a polymer chain. For polymers with similar compositions, the lower FVF can bring with higher T_g of that polymeric materials, for it can not provide sufficient space for segment motion at the same temperature. It is clear that free volume fraction of 2,2',3,3'-BPDA-ODA system is higher than 3,3',4,4'-BPDA-ODA system at the same temperature, as the same result for specific volume showing in Figure 2. In 2,2',3,3'-BPDA-ODA system, incorporation of asymmetry group decreases the regularity of polymer chain, inhibits the close packing of inter polymer chain, and increases free volume at molecular scale, namely facilitates the segment motion to some extent. This result may go against the result of higher T_g of isomeric PIs. However, free volume is not the single variable to evaluate the T_g of PIs, other factors that may affect the T_g will be discussed in the following sections.

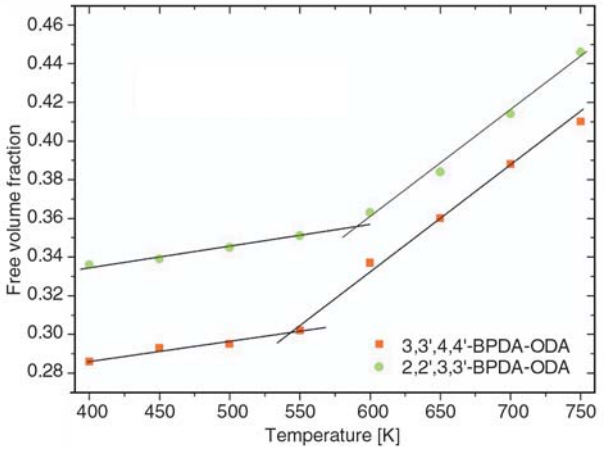

Figure 3. Plots of free volume fraction versus temperature for two polyimides: 3,3',4,4'-BPDA-ODA (■); 2,2',3,3'-BPDA-ODA (●)

3.3. Role of the energy components in glass transition process

To understand the role of each energy component playing in glass transition process, we examined the plot of the energy component versus temperature for two PI systems, and the result shows that the PIs show the same trend in the plot. Take isomeric 2,2',3,3'-BPDA-ODA system for example, the simulated results of bond energy, angle energy, torsion energy, inversion energy and non-bond energy versus the temperature were plotted in Figure 4. There is a kink only in the plot of non-bond energy versus temperature, indicating the occurrence of glass transition. At both below and above T_g, non-bond energy increases almost linearly with increasing temperature with a break at T_g. But for the other energy components, they consistently increase linearly with increasing temperature in the whole temperature range. These results show that the non-bond energy plays an important role in the glass transition process of the polymer system. The above results are consistent with the same analysis on epoxy resin by Wu and Xu [12]. However, Li

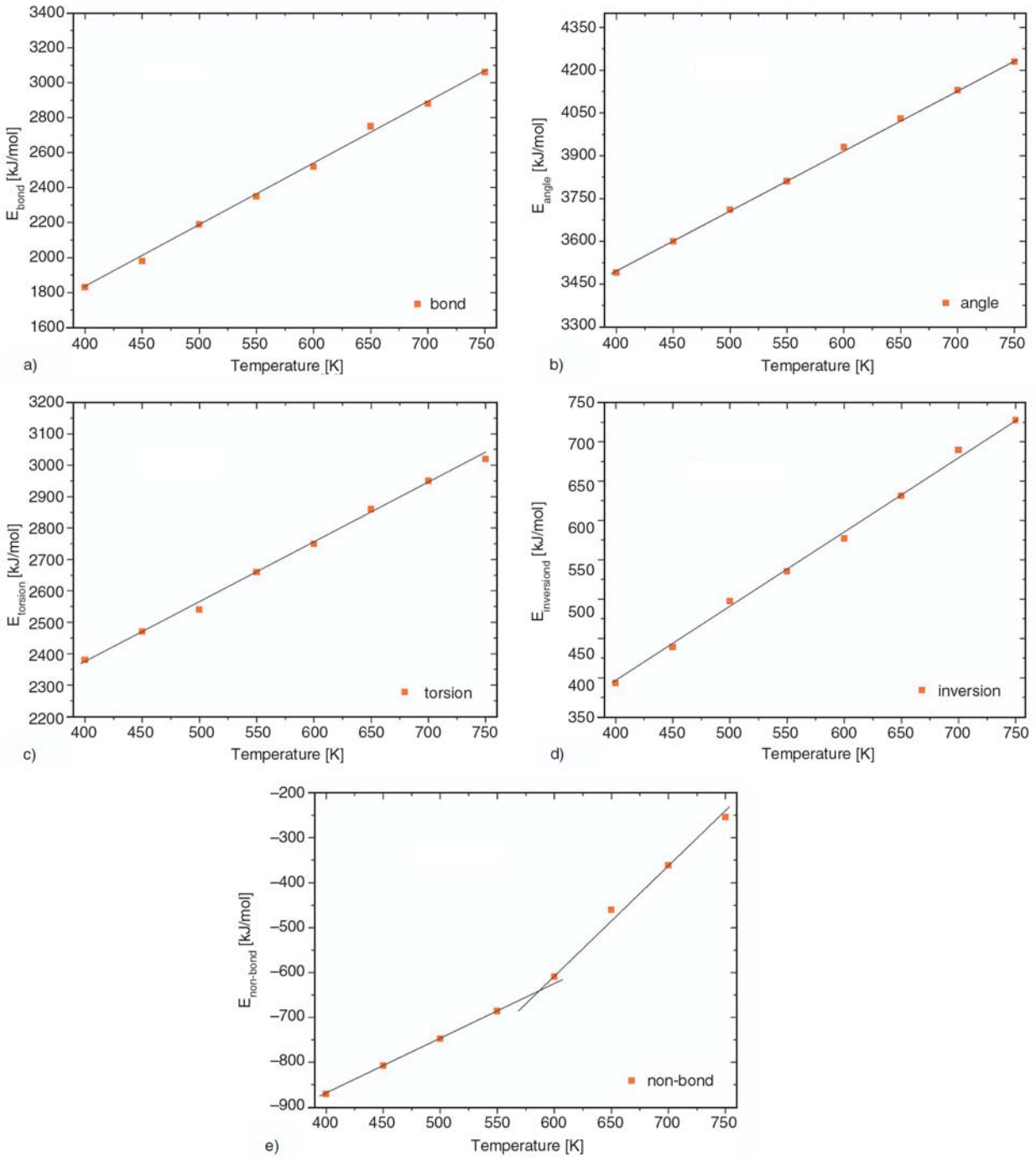

Figure 4. Plots of some energy components versus temperature of 2,2',3,3'-BPDA-ODA: (a) bond energy; (b) angle energy; (c) torsion energy; (d) inversion energy; (e) non-bond energy

and coworkers [8, 26] also performed the same analysis on polyoxymethylene (POM) system [8] and poly(3-hydroxybutyrate) (PHB)/poly(ethylene oxide) (PEO) blend system [26] and drew a different conclusion from ours: both torsion and non-bond energy played important roles in glass transition. In fact, the freedom of bond stretching and angle bending could be equilibrated fast in the simulation, therefore the linear increasing trend are shown. Unlike the common alkyl polymers, aromatic PI has much higher T_g for it has plenty of phenyl and imide rings, so the dihedral torsion and out-of-plane motion of aromatic PIs are constrained, and no kink has been observed in this study. However, the segment motion ability of aromatic PIs are mainly attributed to the limited torsion of linking of phenyl and imide rings [13]. Influenced by the thermal fluctuation, limited link-

ing groups show distinct mobility, yielding the conformation transition, and furthermore, resulting in the sudden change of non-bond energy near T_g.

3.4. Torsion angle distribution

As discussed in section 3.3, mobility of linking groups exerts an important influence during the glass transition process. In order to elucidate the reason for the higher T_g of isomeric PI, torsion angle distributions of linking in two PIs were plotted (Figure 5 and Figure 6). Torsion angles Φ1, Φ2 and Φ3 were defined in Figure 1. For facilitating the discussion, we defined C_p for carbon atom in phenyl ring and C_i for carbon atoms in imide ring linking the ether group. Therefore, we can define C_p–C_p–C_p–C_i (Φ4) as the torsion angle of C_p–C_p between phenyl and imide rings, and H–C_p–C_p–C_p (Φ5) as torsion angle of C_p–C_p in the phenyl ring which is between imide ring and ether group. Furthermore, the Φ4 and Φ5 can be used for study of the co-plane properties of these aromatic rings. As

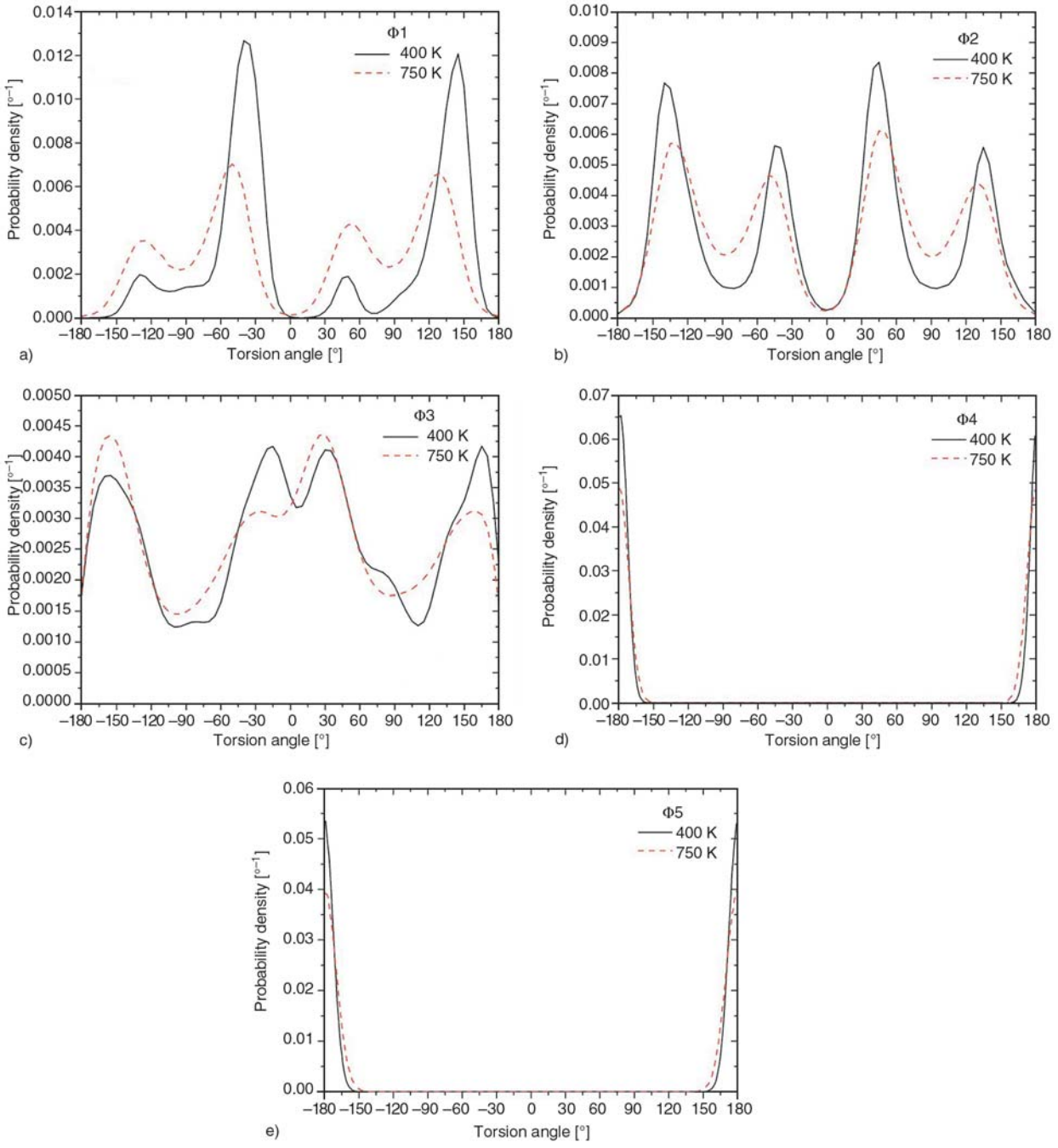

Figure 5. Torsion angle distributions of 3,3',4,4'-BPDA-ODA: (a) Φ1, (b) Φ2, (c) Φ3, (d) Φ4 and (e) Φ5. The results have been obtained with constant-NVT MD simulation at T = 400 K (——) and 750 K (– –).

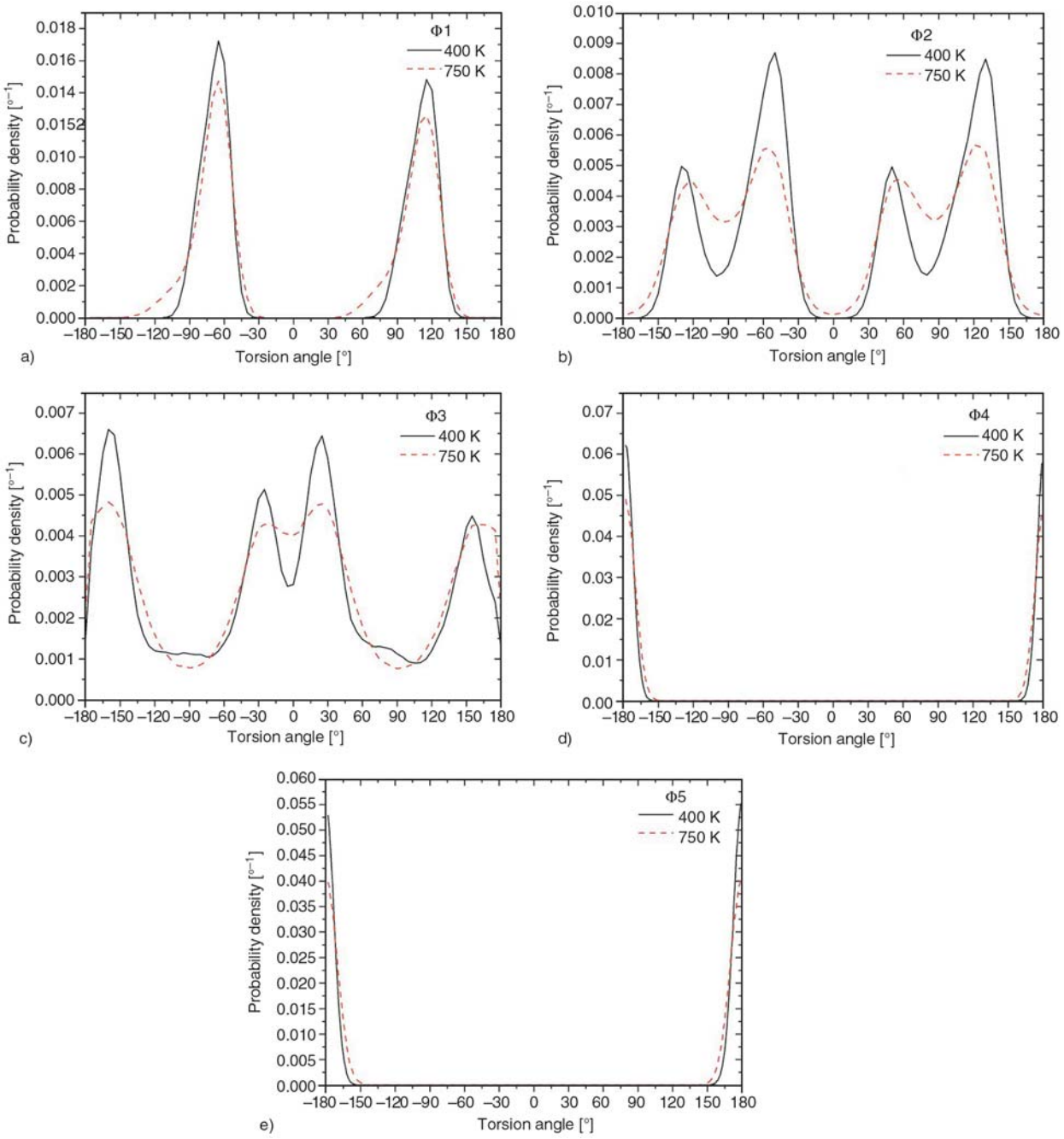

Figure 6. Torsion angle distributions of 2,2',3,3'-BPDA-ODA: (a) Φ1, (b) Φ2, (c) Φ3, (d) Φ4 and (e) Φ5. The results have been obtained with constant-NVT MD simulation at T = 400 K (——) and 750 K (– –).

for Φ1 (torsion angle of C_p–C_p between phenyl ring), 3,3',4,4'-BPDA-ODA system has peaks in ±35° and ±135°, but in isomeric 2,2',3,3'-BPDA-ODA system, there are only two peaks located in the ±60°. This result is similar to the plot of relative energy of torsion angles for PI monomers in the same systems obtained by molecular mechanics in the previous study [5]. Higher rotational barrier corresponding to Φ1 in 2,2',3,3'-BPDA-ODA system is responsible for the two symmetrical two peaks in the torsion angle distribution, and eventually results in its higher T_g. Two PIs have the same peak position but different relative proportion for Φ2 (torsion angle of N–C_p between imide and phenyl rings) and Φ3 (torsion angle of C_p–O in diamine structure). As for Φ4 and Φ5, two PIs have only two half peaks in ±180°, illustrating that phenyl and imide ring can keep in a plane well under the premise of phenyl ring's keeping in a plane. To explore the effect of temperature on torsion angle distribution, two PIs' torsion angle distributions in 400 and 750 K were given. These

distribution functions exhibit peak at the same position at two different temperatures, only a wide distribution at the higher temperature, especially Φ2 and Φ3. No matter at glassy or rubbery state, the torsion angles of Φ4 and Φ5 are kept around ±180°. It proves that atoms in phenyl and imide ring of PIs can be kept in a plane respectively during the glass transition process. Furthermore, it also confirms that the torsion energy does not have sudden change in the glass transition process due to confined torsion, which has been discussed in section 3.3.

3.5. Mean square displacement

The value of T_g is correlated well with the polymer rigidity, namely the segmental mobility in polymer chain. To observe the mobility of PI chains during glass transition process, the mean square displacements (MSD) were calculated [14]. With the increasing temperature, the slope of MSD of both two PI systems becomes steeper. Take 2,2',3,3'-BPDA-ODA system as an example (Figure 7), the slope of MSD above T_g (700 and 750 K) are much higher than that below T_g (400 and 500 K), indicating higher mobility of PI chains above T_g. Furthermore, we have also compared the mobility of 3,3',4,4'-BPDA-ODA and 2,2',3,3'-BPDA-ODA systems. Figure 8 shows the mean square displacement plot for the two PI systems at 400 and 750 K. It is shown that the MSD for 2,2',3,3'-BPDA-ODA system is lower than that for 3,3',4,4'-BPDA-ODA system at all times. This means 2,2',3,3'-BPDA-ODA system has lower mobility than 3,3',4,4'-BPDA-ODA system, and hence it needs more time

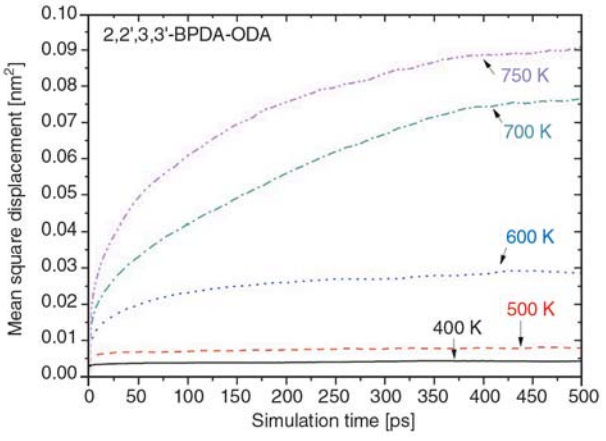

Figure 7. Mean square displacements of 2,2',3,3'-BPDA-ODA system as a function of temperature

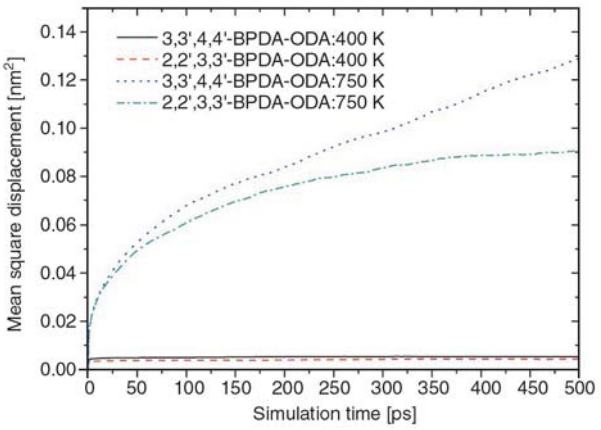

Figure 8. Mean square displacements of 3,3',4,4'-BPDA-ODA and 2,2',3,3'-BPDA-ODA systems at T = 400 K and 750 K

(or higher temperature) to obtain segment motion. The above observations support the result of higher T_g of 2,2',3,3'-BPDA-ODA systems.

3.6. Vector autocorrelation function

To further characterize the mobility of PI chains, the mobility of linking groups were examined. It can be quantified by vector autocorrelation functions (VACFs) of these groups along the polymer chain (Equation (3)):

$$M_2(t) = \frac{3 < (u(t) \bullet u(0))^2 > -1}{2} \tag{3}$$

where $u(t)$ and $u(0)$ represent unit vectors of the segment at time t and time 0, respectively. The < > indicates an ensemble average over such vectors [12]. At the same simulation time, the higher value of $M_2(t)$ indicates the higher rigidity of the segment.

The segmental vectors corresponding to the torsion angle Φ1, Φ2, Φ3, Φ4 and Φ5 are shown in Table 2. They are defined as the vectors from the first atom to the fourth atom of the torsion angles. The plots of VACFs of these segments in two PIs are given at two temperatures: 400 K (Figure 9) and 750 K (Figure 10) [12]. At 400 K, the value

Table 2. Definition of segmental vectors corresponding to torsion angle Φ1, Φ2, Φ3, Φ4 and Φ5

Torsion angle	Atoms	Segmental vector
Φ1	C_{p1}–C_{p2}–C_{p3}–C_{p4}	$C_{p1} \rightarrow C_{p4}$
Φ2	C_i–N–C_{p1}–C_{p2}	$C_i \rightarrow C_{p2}$
Φ3	C_{p1}–C_{p2}–O–C_{p3}	$C_{p1} \rightarrow C_{p3}$
Φ4	C_{p1}–C_{p2}–C_{p3}–C_i	$C_{p1} \rightarrow C_i$
Φ5	H–C_{p1}–C_{p2}–C_{p3}	H $\rightarrow C_{p3}$

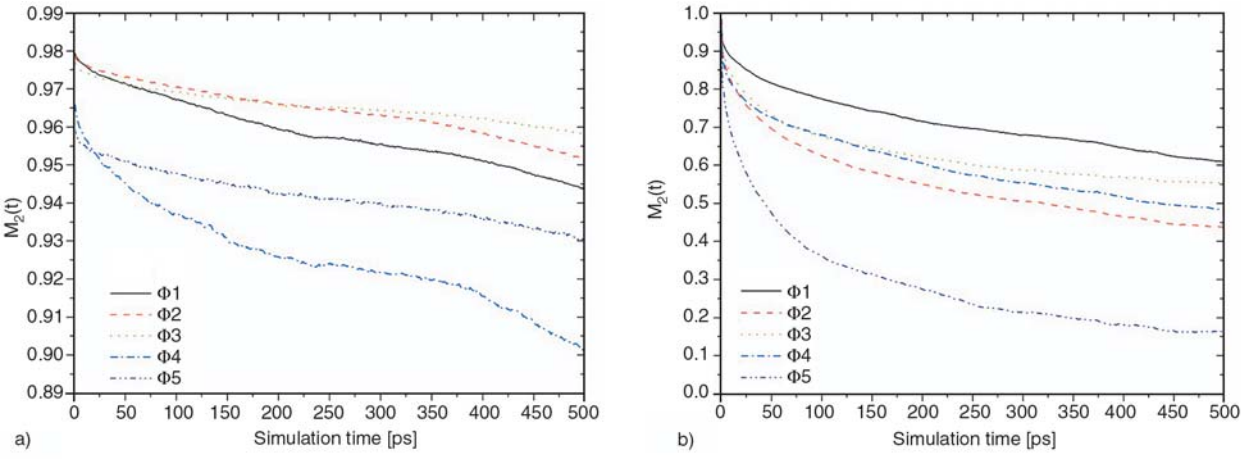

Figure 9. Vector autocorrelation functions of vector bonds corresponding to Φ1, Φ2, Φ3, Φ4 and Φ5 in 3,3',4,4'-BPDA-ODA with constant-NVT MD simulation at (a) T = 400 K and (b) 750 K

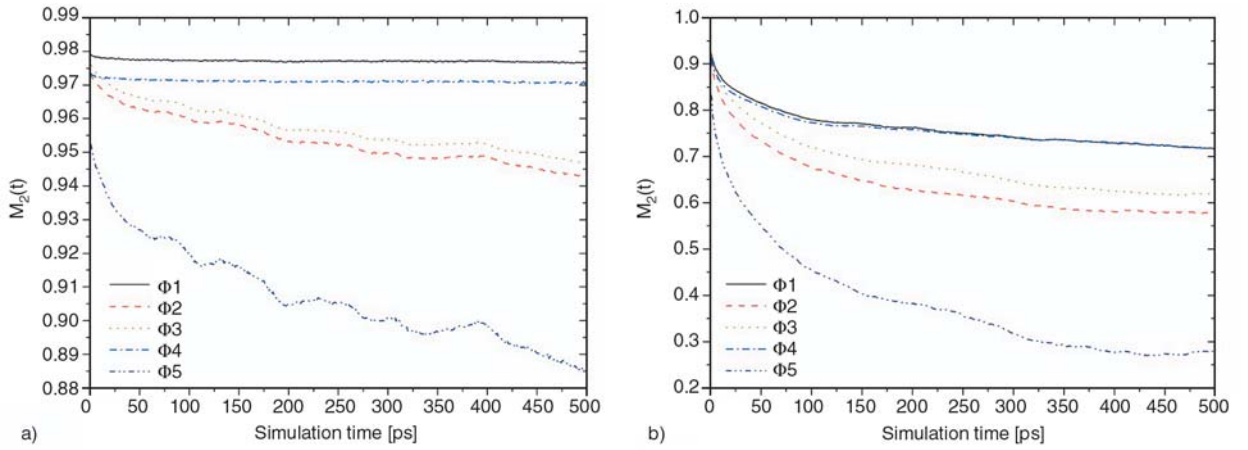

Figure 10. Vector autocorrelation functions of vector bonds corresponding to Φ1, Φ2, Φ3, Φ4 and Φ5 in 2,2',3,3'-BPDA-ODA with constant-NVT MD simulation at (a) T = 400 K and (b) 750 K

$M_2(t)$ in two PIs are above 0.9 during the simulation time, indicating high chain rigidity of PIs. In 3,3',4,4'-BPDA-ODA system, the mobility of Φ1 is higher than Φ2 and Φ3, but the opposite result is obtained in 2,2',3,3'-BPDA-ODA system. The reason is that higher steric hindrance between biphenyl group can lead to lower torsion mobility of 2,2',3,3'-BPDA-ODA system. Because the aromatic rings can keep in a plane respectively during the simulation, we can define $C_{p1} \rightarrow C_i$ (Φ4) to characterize the torsion mobility of phenyl and neighboring imide rings. Also, we can define $H \rightarrow C_{p3}$ (Φ5) to characterize that of phenyl ring in diamine structure. In this way, the cooperative motion among Φ1, Φ2 and Φ3 can be characterized through Φ4 and Φ5. In 3,3',4,4'-BPDA-ODA system, the mobility of Φ4 is much higher than Φ1 and Φ2, for it exists a positive cooperative motion between Φ1 and Φ2. Yet, in 2,2',3,3'-BPDA-ODA system, mobility of Φ4 lies between Φ1 and Φ2, which indicates that Φ1 has reverse torsion motion with Φ2, thereby it weaken the mobility of Φ4. As for Φ5, its mobility is much higher than Φ2 and Φ3 in two PI systems, showing the positive cooperative motion between Φ2 and Φ3. Possible torsion model is shown in Figure 1, and the result confirms the inference of torsion analysis via DMA method in the previous study [6]. In two PI systems, the mobility of five torsion angles shows an obvious increment at 750 K, and the same arrangement order in mobility, that is Φ5>Φ2>Φ3≈Φ4>Φ1. This result indicates that the Φ2 and Φ3 are easier than Φ1 to be influenced by thermal fluctuation. The mobility of Φ2 and Φ3 increase more quickly at higher temperature, and then the conformation transitions are easier to take place. So the corresponding torsion angles are distributed wider (see Figure 5 and Figure 6). The mobility of Φ1 is the lowest among the five torsion angles, and hence it can be used to compare the mobility of the polymer

chains in two PI systems. At 750 K, the value of $M_2(t)$ in 2,2',3,3'-BPDA-ODA system is higher than that of 3,3',4,4'-BPDA-ODA system. This result indicates that 2,2',3,3'-BPDA-ODA system has lower mobility than 3,3',4,4'-BPDA-ODA system. And it also confirms the claim that the higher T_g in isomeric 2,2',3,3'-BPDA-ODA system is mainly attributed to the limited torsion motion between biphenyl groups. Yet, in two PI systems, the mobility of Φ4 lays between Φ1 and Φ2, while that of Φ5 is much higher than Φ2 and Φ3. In other words, the positive comparative motion of Φ1 and Φ2 in 3,3',4,4'-BPDA-ODA system disappears in the rubbery state. It may be resulted from partial reverse motion of diamine structure above glass transition temperature.

4. Conclusions

MD simulation was performed to study the glass transition temperature of isomeric PIs. Simulated T_g is consistent with experimental value: T_g of isomeric 2,2',3,3'-BPDA-ODA system is higher than 3,3',4,4'-BPDA-ODA system.

The glass transition temperature of polymeric materials is mainly determined by the segment motion of a polymer chain. It mainly involves the factors at space scale (free volume) and time scale (chain rigidity). Higher rigidity and less free volume lead to the higher T_g of polymers, however, these two factors are in opposition in isomeric PI (2,2',3,3'-BPDA-ODA). The higher free volume fraction of isomeric PI can provide the polymer with more space to obtain the segment motion. However, from the torsion angle distribution calculations, it is shown that the torsion angle of its biphenyl group is constrained. Furthermore, from mean square displacement and vector autocorrelation functions calculations, this group is observed to rotate against other groups in the glassy state, and increases the chain rigidity to a great extent. So the isomeric PI needs much more relaxation time for the segment motion. Therefore, the higher T_g of isomeric PI is mainly attributed to the chain rigidity for the time scale, not the free volume for the space scale.

Acknowledgements

We are grateful for the financial support from the National Natural Science Foundation of China (No.50433010).

References

[1] Ding M.: Isomeric polyimides. Progress in Polymer Science, **32**, 623–668 (2007).
DOI: 10.1016/j.progpolymsci.2007.01.007

[2] Hsiao S-H., Liou G-H.: Preparation and characterization of aromatic polyamides from 4,4'-(2,6-naphthylenedioxy)dibenzoic acid and aromatic diamines. Macromolecular Chemistry and Physics, **199**, 2321–2328 (1999).
DOI: 10.1002/(SICI)1521-3935(19981001)199:10<2321::AID-MACP2321>3.0.CO;2-R

[3] Parthiban A., Le Guen A., Yansheng Y., Hoffmann U., Klapper M., Müllen K.: Amino-functionalized poly(arylene ether ketone)s. Macromolecules, **30**, 2238–2243 (1997).
DOI: 10.1021/ma961310y

[4] Goodwin A. A., Campbell J. A., Wang Z. Y.: Poly(aryl ether ketone)s containing dibenzoylbiphenyl groups: Dynamic mechanical and physical ageing behaviour. Polymer International, **48**, 353–359 (1999).
DOI: 10.1002/(SICI)1097-0126(199905)48:5<353::AID-PI138>3.0.CO;2-J

[5] Tong Y., Huang W., Luo J., Ding M.: Synthesis and properties of aromatic polyimides derived from 2,2',3,3'-biphenyltetracarboxylic dianhydride. Journal of Polymer Science Part A: Polymer Chemistry, **37**, 1425–1433 (1999).
DOI: 10.1002/(SICI)1099-0518(19990515)37:10<1425::AID-POLA4>3.0.CO;2-G

[6] Kochi M., Chen C., Yokota R., Hasegawa M., Hergenrother P.: Isomeric biphenyl polyimides. (II) Glass transitions and secondary relaxation processes. High Performance Polymers, **17**, 335–347 (2005).
DOI: 10.1177/0954008305055557

[7] Hasegawa M., Sensui N., Shindo Y., Yokota R.: Structure and properties of novel asymmetric biphenyl type polyimides. Homo- and copolymers and blends. Macromolecules, **32**, 387–396 (1999).
DOI: 10.1021/ma9808629

[8] Yu K., Li Z., Sun J.: Polymer structures and glass transition: A molecular dynamics simulation study. Macromolecular Theory and Simulations, **10**, 624–633 (2001).
DOI: 10.1002/1521-3919(20010701)10:6<624::AID-MATS624>3.0.CO;2-K

[9] Han J., Gee R. H., Boyd R. H.: Glass transition temperatures of polymers from molecular dynamics simulations. Macromolecules, **27**, 7781–7784 (1994).
DOI: 10.1021/ma00104a036

[10] Pozuelo J., Baselga J.: Glass transition temperature of low molecular weight poly(3-aminopropyl methyl siloxane). A molecular dynamics study. Polymer, **43**, 6049–6055 (2002).
DOI: 10.1016/S0032-3861(02)00442-1

[11] Zhang J., Liang Y., Yan J., Lou J.: Study of the molecular weight dependence of glass transition temperature for amorphous poly(L-lactide) by molecular dynamics simulation. Polymer, **48**, 4900–4905 (2007).
DOI: 10.1016/j.polymer.2007.06.030

[12] Wu C., Xu W.: Atomistic molecular simulations of structure and dynamics of crosslinked epoxy resin. Polymer, **48**, 5802–5812 (2007).
DOI: 10.1016/j.polymer.2007.07.019

[13] Liang T., Yang X., Zhang X.: Prediction of polyimide materials with high glass-transition temperatures. Journal of Polymer Science Part B: Polymer Physics, **39**, 2243–2251 (2001).
DOI: 10.1002/polb.1198

[14] Yani Y., Lamm M. H.: Molecular dynamics simulation of mixed matrix nanocomposites containing polyimide and polyhedral oligomeric silsesquioxane (POSS). Polymer, **50**, 1324–1332 (2009).
DOI: 10.1016/j.polymer.2008.12.045

[15] Materials Studio 4.0 software:
http://www.accelrys.com

[16] Mayo S. L., Olafson B. D., Goddard W. A.: DREIDING: A generic force field for molecular simulations. The Journal of Physical Chemistry, **94**, 8897–8909 (1990).
DOI: 10.1021/j100389a010

[17] Theodorou D. N., Suter U. W.: Detailed molecular structure of a vinyl polymer glass. Macromolecules, **18**, 1467–1478 (1985).
DOI: 10.1021/ma00149a018

[18] Theodorou D. N., Suter U. W.: Atomistic modeling of mechanical properties of polymeric glasses. Macromolecules, **19**, 139–154 (1986).
DOI: 10.1021/ma00155a022

[19] Pan R., Liu X., Zhang A., Gu Y.: Molecular simulation on structure-property relationship of polyimides with methylene spacing groups in biphenyl side chain. Computational Materials Science, **39**, 887–895 (2007).
DOI: 10.1016/j.commatsci.2006.10.019

[20] Nosé S.: A molecular dynamics method for simulations in the canonical ensemble. Molecular Physics, **52**, 255–268 (1984).
DOI: 10.1080/00268978400101201

[21] Nosé S.: A unified formulation of the constant temperature molecular dynamics methods. The Journal of Chemical Physics, **81**, 511–519 (1984).
DOI: 10.1063/1.447334

[22] Berendsen H. J. C., Postma J. P. M., van Gunsteren W. F., DiNola A., Haak J. R.: Molecular dynamics with coupling to an external bath. The Journal of Chemical Physics, **81**, 3684–3690 (1984).
DOI: 10.1063/1.448118

[23] Cypcar C. C., Camelio P., Lazzeri V., Mathias J. L., Waegell B.: Prediction of the glass transition temperature of multicyclic and bulky substituted acrylate and methacrylate polymers using the energy, volume, mass (EVM) QSPR model. Macromolecules, **29**, 8954–8959 (1996).
DOI: 10.1021/ma961170s

[24] Camelio P., Lazzeri V., Waegell B., Cypcar C., Mathias J. L.: Glass transition temperature calculations for styrene derivatives using the energy, volume, and mass model. Macromolecules, **31**, 2305–2311 (1998).
DOI: 10.1021/ma970983t

[25] Zhang J., Lu J., Liu W., Xue Q.: Separation of CO_2 and CH_4 through two types of polyimide membrane. Thin Solid Films, **340**, 106–109 (1999).
DOI: 10.1016/S0040-6090(98)01350-9

[26] Yang H., Li Z-S., Qian H., Yang Y., Zhang X., Sun C.: Molecular dynamics simulation studies of binary blend miscibility of poly(3-hydroxybutyrate) and poly(ethylene oxide). Polymer, **45**, 453–457 (2004).
DOI: 10.1016/j.polymer.2003.11.021